

Diss. ETH No. 15824

Energy release in solar flares

A dissertation submitted to the
SWISS FEDERAL INSTITUTE OF TECHNOLOGY
ZÜRICH

for the degree of
Doctor of Sciences

presented by

PASCAL SAINT-HILAIRE

Dipl. Phys.

born March 9, 1972
citizen of Sigriswil (BE)

accepted on the recommendation of
Prof. Dr. Arnold O. Benz, examiner
PD Dr. Manuel Güdel and Prof. Dr. Jan O. Stenflo,
co-examiner

2005

Contents

Abstract	v
Resumé	vii
1 Introduction	1
1.1 The changing Sun, from radio to gamma-rays	1
1.1.1 Radio: 20MHz($\lambda=15$ m)–300GHz ($\lambda=1$ mm)	3
1.1.2 Infrared 1mm–0.75 μ m	6
1.1.3 Visible or optical 750–380 nm	6
1.1.4 Ultraviolet 380–10 nm	7
1.1.5 Soft X-rays 10–0.1 nm (\sim 0.1–10 keV)	7
1.1.6 Hard X-rays 10–300keV	8
1.1.7 Gamma-rays >300 keV	9
1.2 Emission mechanisms	9
1.2.1 Bremsstrahlung	9
1.2.2 Gyro-emission	11
1.2.3 Electron-Cyclotron Maser	12
1.2.4 Plasma emission	12
1.3 The standard solar flare scenario	13
2 Hard X-ray, ejecta, and their associated decimetric radio emission in solar flares	21
2.1 Introduction	22
2.2 Instruments and data selection	24
2.2.1 The YOHKOH Hard X-ray Telescope (HXT)	24

2.2.2	The Phoenix-2 spectrometer	25
2.2.3	The Nançay Radioheliograph (NRH)	25
2.2.4	The Yohkoh Soft X-ray Telescope (SXT)	26
2.2.5	The Transitional and Coronal Explorer (TRACE)	26
2.2.6	Other data	26
2.2.7	Selection of Events	26
2.3	Observations and results	28
2.3.1	HXR/SXR/EUV observations	35
2.3.2	Radio observations	37
2.3.3	LASCO observations:	38
2.4	Discussion	38
2.5	Conclusions	41
3	The RHESSI Experimental Data Center	43
3.1	Introduction	43
3.2	Description of HEDC	45
3.2.1	Architecture	47
3.2.2	On-line RHESSI data repository	48
3.2.3	HEDC Extended Catalog generation	48
3.2.4	The data management (dm) component	49
3.2.5	The processing logic (pl) component	51
3.2.6	Other services	52
3.3	Using HEDC	55
3.3.1	Browsing with the Web interface	55
3.3.2	Processing with the Web interface	56
3.3.3	Synoptic engine	57
3.3.4	The StreamCorder	57
3.4	First experiences and conclusions	58
3.5	ADDENDUM: Status as of October 2004	58
3.6	ADDENDUM: HEDC Extended Catalog contents	59
3.6.1	Detection of events	60
3.6.2	Determination of event attributes	60

3.6.3	Data Products automatically generated with each event	60
3.6.4	Others	65
3.7	ADDENDUM: Attributes used for browsing queries	65
4	Energy budget and imaging spectroscopy of a compact flare	69
4.1	Introduction	70
4.2	Lightcurves and other generalities	72
4.3	Source size	73
4.4	RHESSI imaging spectroscopy	80
4.5	Spectral features	82
4.6	TRACE images with RHESSI overlays	84
4.7	Energy budget	85
4.8	Conclusions	89
5	Thermal and non-thermal energies of solar flares	91
5.1	Introduction	92
5.2	Basic theory	94
5.2.1	Thick-target bremsstrahlung emission	94
5.3	Known and unknown errors in computing non-thermal energies	102
5.3.1	Errors due to approximations of bremsstrahlung cross-section, collisional energy loss cross-sections, and other factors	102
5.3.2	Some numerical examples	105
5.3.3	Finding the low-energy cutoff or turnover	109
5.4	RHESSI flare observations, data analysis	109
5.4.1	Flare selection criteria	109
5.4.2	Extracting the thermal and non-thermal flare energies	110
5.5	Results and discussion	115
5.6	Conclusions	119
5.7	ADDENDUM: Collisional evolution of an injected electron spectrum	120

5.8	ADDENDUM: Surface brightness of two volumes with the same plasma contents	121
6	Summary and Outlook	123
6.1	Summary	123
6.2	Outlook	125
A	Useful cross-sections	129
A.1	Bremsstrahlung cross-sections	129
A.2	Energy-loss cross-sections	130
A.2.1	Coulomb energy-loss cross-section	130
A.2.2	Magnetobremsstrahlung (gyro- and synchrotron) energy losses	131
B	Energy deposition in the upper chromosphere and transition region	135
C	The Ramaty High-Energy Solar Spectroscopic Imager	141
	Curriculum Vitae	145
	List of Publications	147
	Acknowledgments	149
	Bibliography	151

Abstract

Solar flares have been happening for a long time, and, when the Sun was young, were probably much stronger than today's. But only in the last few decades have they been observed in the whole electromagnetic spectrum. Current solar observatories, both space-born and ground-based, provide a (sometime overwhelming) wealth of data at high spectral, temporal, and spatial resolutions. The aim of this thesis is a better interpretation and understanding of solar flares, mainly by studying their signatures in parts of the electromagnetic spectrum where they are the most spectacular: X-ray, ultraviolet, and radio. Of course, only a portion of the overall problem has been tackled. The emphasis is mostly on X-ray observations, as they seem to provide the most direct and quantitatively usable particle acceleration signatures.

The introductory section of this thesis starts with a cursory glance at the electromagnetic spectra of the quiet, active and flaring Sun. Then, relevant emission mechanisms are briefly discussed, in particular bremsstrahlung. The introduction is concluded with a description of the current standard solar flare model.

The other chapters of this work are derived from submitted or published articles in refereed journals.

In Chapter 2¹, temporal and spatial correlations in solar flares of hard X-rays, radio decimetric continuum emission, ejecta and CMEs were examined. The focus was on three well-observed, medium-sized flares. The main findings were that (1) major hard X-ray flares are often associated with ejecta seen in soft X-rays and extreme ultraviolet. (2) These ejecta seem to start before any hard X-ray or decimetric radio emission, suggesting a driven reconnection model. (3) Particularly at high frequencies, decimetric radio continuum occurring nearly simultaneously with the first

¹Based on Saint-Hilaire & Benz (2003)

hard X-ray peak are located close to the hard X-ray source, and may be a good indicator of the main acceleration region.

With the launch of the RHESSI X-ray satellite (see e.g. Appendix C), a data center was set up to deal with the large amount and the complexity of the incoming data: This is discussed in Chapter 3². This data center automatically generates a catalogue of images, lightcurves and other data products for each flare observed by RHESSI. This catalogue is browsable on-line, thereby greatly increasing the speed at which scientists find data sets of interest. Although this other feature has not been as extensively used, scientists also have the possibility to create simple data products and add them to the database.

In Chapter 4³, a first attempt to combine RHESSI and data from other observatories is made to obtain the energy partition of a solar flare. The kinetic energy in non-thermal electrons, the thermal energy in the heated plasma, and the kinetic energy in bulk motion all seem to lie within the same order of magnitude. Rough imaging spectroscopy has also been done: The thermal source was initially found to be spatially stable, then to slowly drift outwards.

In Chapter 5⁴, flare X-ray emission have been theoretically examined in great details, in order to provide the best possible estimates of flare particle energies, as well as to compare them with energies derived from secondary thermal emission. The electromagnetic signature of accelerated particles is about 10^5 times less powerful than that of the thermal emission, but is a direct signature of the accelerated electrons. While possible sources of errors are potentially still large, the study of several medium-sized, well-observed RHESSI flares shows that both the kinetic energy in accelerated electrons and the energy in the hot plasma are similar, and that caution should be used when measuring this last quantity.

This thesis concludes with a summary and an outlook on future work.

²Based on Saint-Hilaire & al. (2002)

³Based on Saint-Hilaire & Benz (2002)

⁴Based on Saint-Hilaire & Benz (2005)

Resumé

Les éruptions solaires ont toujours été présentes, et étaient probablement bien plus fortes au début de la vie de notre Soleil. Cependant, leur observation dans tout le spectre électromagnétique n'existent que depuis quelques décennies. Les observatoires solaires, spatiaux ou terrestres, fournissent des données à haute résolution spectrale, temporelle, et spatiale (parfois en quantité phénoménale). Le but de cette thèse est une meilleure compréhension et interprétation des éruptions solaires, en se basant principalement sur leurs signatures dans le spectre électromagnétique où ils sont le plus spectaculaires: les rayons X, les ultraviolets, et les ondes radio. Bien sûr, seulement une partie du problème n'a pu être examinée: l'emphase a été placée sur les observations dans les rayons X, puisqu'ils semblent être la signature la plus directe (et la plus utilisable quantitativement) d'accélération de particules.

Le chapitre introductoire de cette thèse commence par un bref aperçu des spectres électromagnétiques produit par le Soleil, durant ses extrema d'activités et durant ses éruptions. Puis, les principaux mécanismes d'émissions électromagnétiques sont brièvement discutés, en particulier le rayonnement de freinage ('bremsstrahlung'). L'introduction est conclue par une description de l'actuel modèle standard d'éruption.

Les autres chapitres de cette dissertation sont dérivés d'articles soumis ou déjà publiés dans des journaux scientifiques arbitrés.

Dans le chapitre 2, les corrélations temporelles et spatiales entre rayons X durs, continus d'émission radio decimétrique, éjection coronale de masse et autres éjections lors d'éruptions solaires ont été examinées. L'emphase a été placée sur trois éruptions bien observées de moyenne intensités. Les conclusions principales sont que (1) les éruptions avec émission intense de rayons X durs sont généralement associées avec des éjections observées dans les rayons X mous et l'ultraviolet. (2) Ces éjections semblent commencer avant toute émission de rayons X durs ou

radio décimétrique, ce qui suggère un modèle de reconnexion magnétique forcé (“driven magnetic reconnection”). (3) Particulièrement à hautes fréquences, les continuums radio décimétriques simultanés au premier pic de rayons X durs sont localisés très proches de la source de rayons X durs, et pourraient bien indiquer l’emplacement de la région d’accélération.

Avec le lancement du satellite RHESSI (voir appendice C), un centre de données a été mis en place pour faire face à la grande quantité et la complexité des données: ceci est discuté au chapitre 3. Ce centre de données génère automatiquement un catalogue d’images, courbes de lumières et autres données pour chaque éruption solaire observée par RHESSI. Ce catalogue peut être examiné en ligne, permettant aux scientifiques de trouver beaucoup plus rapidement d’intérêt particulier. Bien que cette capacité n’ait pas été exploitée intensivement, les scientifiques ont également la possibilité de créer des données secondaires simples, et de les incorporer à la base de données.

Au chapitre 4, un premier essai de combinaison de données entre RHESSI et d’autres observatoires a été effectué, afin de déterminer le budget énergétique d’une éruption solaire. L’énergie cinétique des électrons accélérés (non-thermiques), l’énergie thermique du plasma surchauffé, et l’énergie cinétique des mouvements de masses semblent tous être du même ordre de grandeur. L’imagerie spectroscopique indique que la source thermique est initialement spatialement stable, puis dérive lentement vers l’extérieur.

Au chapitre 5, l’émission de rayons X par éruptions solaires a été étudiée en détails, afin de pouvoir dériver avec la plus grande exactitude l’énergie des particules, et de les comparer à l’énergie thermique irradiée. La signature électromagnétique directe de ces particules est environ 10^5 fois plus faible que l’émission thermique secondaire. Bien que les sources d’erreurs sont potentiellement toujours importantes, l’étude de plusieurs éruptions de taille moyenne observées par RHESSI montrent que l’énergie cinétique des électrons non-thermiques est similaire à l’énergie thermique irradiée par le plasma surchauffé, quoique cette dernière quantité doit être mesurée avec soin.

Cette thèse se conclut par un aperçu des possibles extensions de ce travail.

Chapter 1

Introduction

Omnia mutantur

1.1 The changing Sun, from radio to gamma-rays

The solar spectrum, from radio to gamma-rays, is displayed in Fig. 1.1. From the near ultraviolet to millimeter wavelengths, it has mostly the shape of a $T \approx 5770\text{K}$ black body. To the naked eye, it hardly ever changes, apart from sunspots. Sunspots might have been first observed by Chinese astronomers around 28 BC or even before. Johann Fabricius of Holland, Galileo Galilei of Italy, Christopher Schiener of Germany, and Thomas Herriot of England all claim to have observed sunspots with telescopes (invented only in 1608 by Dutch craftsmen), somewhen in 1611. After observing sunspots disappearing over the solar limb, Galileo made the breakthrough discovery that they were something on the surface of the Sun (clouds ?), and not objects passing in front of it: The Heavens weren't perfect! We have known for over 150 years that these sunspots appear in cycles. This 9–14 (average ~ 10.8) year cycle was first noted by Heinrich Schwabe, an amateur astronomer, in 1843. Periods of low sunspot number were dubbed “solar minimum”, while periods of high sunspot number, “solar maximum”. Only much later was it discovered that this sunspot cycle was tied to the 22-year magnetic cycle of the Sun.

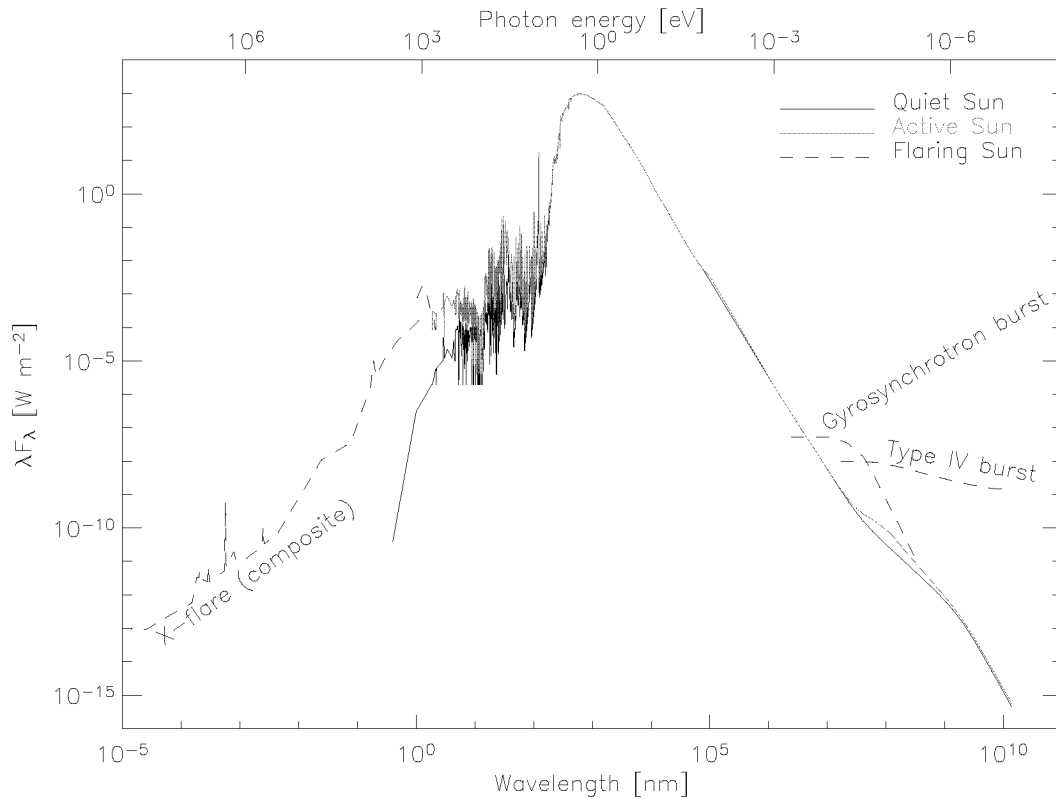


Figure 1.1: The solar spectrum, from gamma-rays to radio. Details and further explanations are found in Figs. 1.2, 1.3, and 1.4. The *dashed lines* (flaring Sun) are upper envelopes.

Radio, ultraviolet and soft X-ray emission change during this 11-year long cycle, and are strongest at “solar maximum”. The total solar irradiance varies by about 0.1% during this cycle.

The most dramatic changes occur during solar flares: Strong radio bursts longer than the millimeter range can be orders of magnitude higher than the quiet solar emission. Ultraviolet and X-ray emission are enhanced. Even gamma-rays are sometimes present in the strongest flares. In the powerful X17 flare of 28 October 2003, Woods et al. (2004) have observed a 270ppm increase in the total solar irradiance (TSI). It is the first time that the TSI has been unambiguously changed by a solar flare event, 23% of it being in the 27–200nm wavelength range.

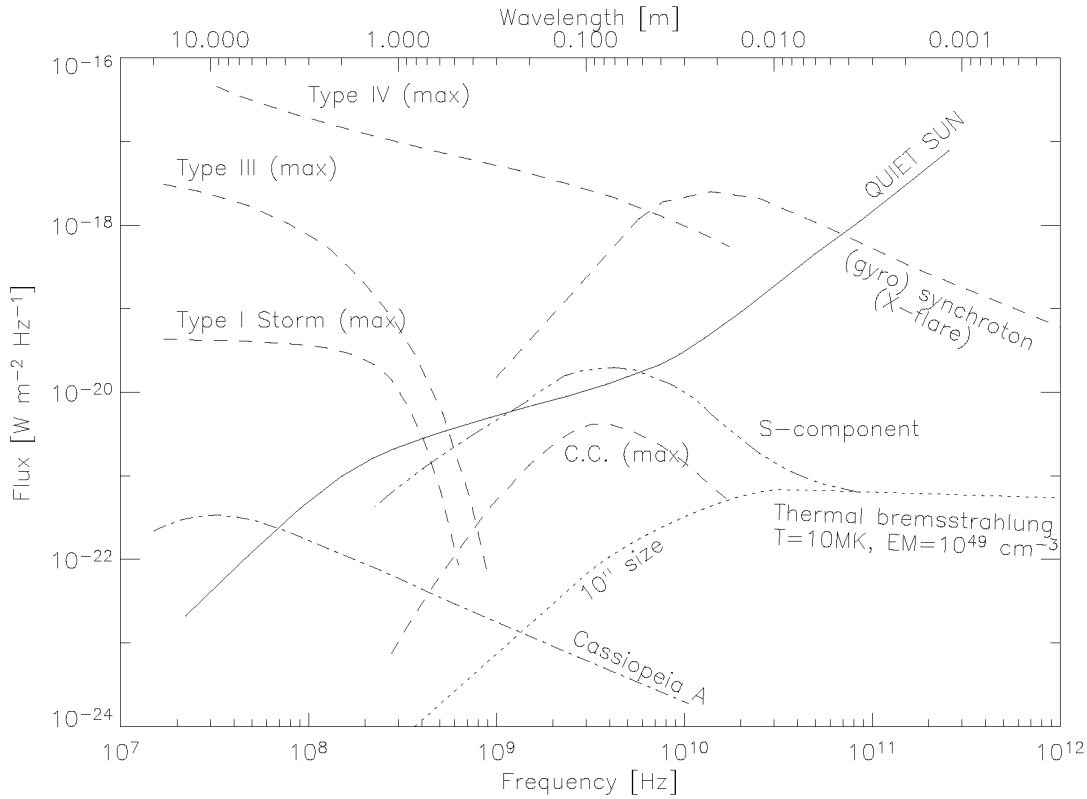


Figure 1.2: Radio spectra observed on Earth: The quiet Sun, its slow component, some solar bursts, and the Cassiopeia A supernova remnant (which loses about 0.7% of its flux every year, Martirosyan et al., 2002). C.C. stands for Coronal Condensation (an area where the corona is hotter and denser than its surrounding, usually above active regions). This radio spectrum is mostly a composite from Styx (2002); www resource (1).

1.1.1 Radio: 20MHz($\lambda=15$ m)–300GHz ($\lambda=1$ mm)

Radio frequencies (RF), from below Extremely Low Frequencies (ELF, 3–30 Hz) to Extremely High Frequencies (EHF, 30–300 GHz) refer to the portion of the electromagnetic (EM) spectrum in which EM waves can be generated by an alternating current fed to an antenna. Extraterrestrial emission below ~ 20 MHz is not observable by ground-based telescopes, as it is blocked by the Earth’s ionosphere. 20 MHz corresponds to the ionosphere’s plasma frequency, which can be perturbed by solar and geomagnetic activity.

The quiet Sun spectrum (Fig. 1.2) above ~ 10 GHz is a power-law with spectral index 2, corresponding to a black-body spectrum with a

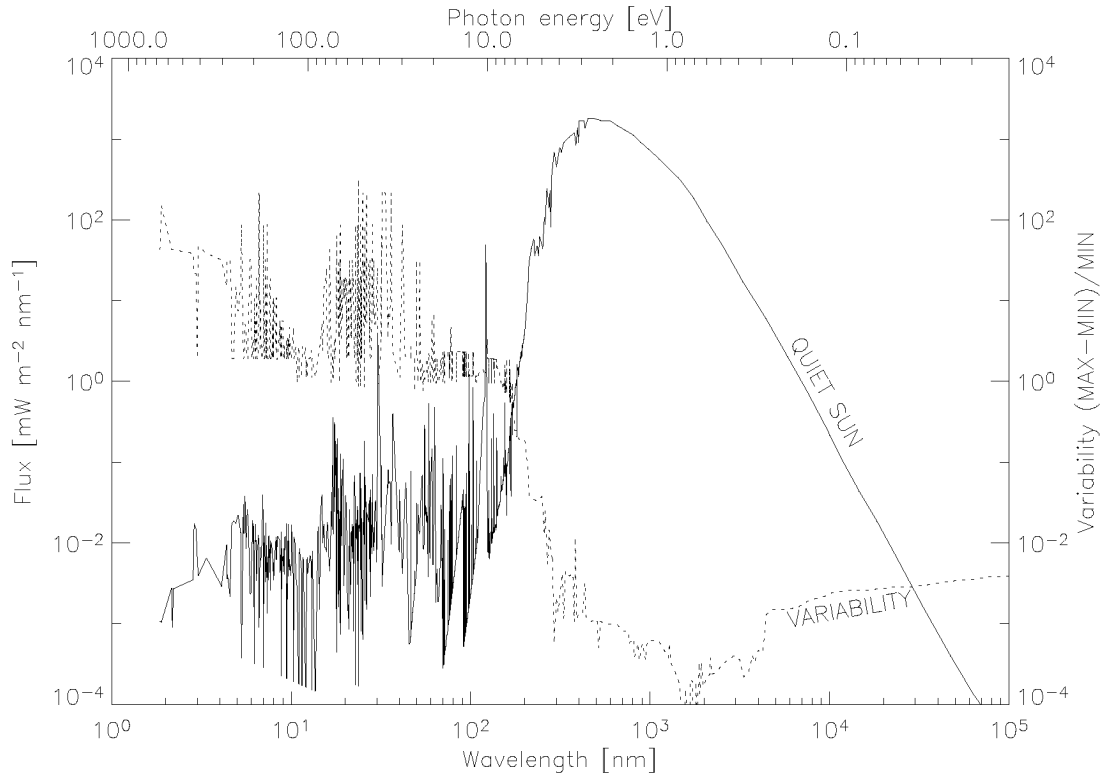


Figure 1.3: The quiet and active Sun, from the far infrared to the extreme ultraviolet. This spectrum is a composite from Hinteregger et al. (1981) and [www resource \(2\)](#).

$T \approx 10^4\text{K}$ temperature. At wavelengths longer than the meter, it has a $T \approx 10^6\text{K}$ black-body spectrum. At 17GHz, the solar limb is 20–25 arc seconds ($\sim 2\%$ of a solar radius) above the photospheric limb, while it is $\sim 50\%$ or more larger at meter and longer wavelengths.

Superimposed on the quiet solar radio emission is the slowly varying *s-component*. It is correlated to the 11-year solar cycle. In fact, the 2.8 GHz (10.7 cm) emission is usually a good indicator of solar activity, and has been used to determine UV irradiance variations (Hinteregger et al., 1981; Bailey et al., 2000).

These radio emissions are mostly from *bremsstrahlung* (free-free) emission, although some of the slowly varying component or coronal condensation above sunspots is thermal gyro-resonance emission.

During flares, powerful radio bursts occur (see e.g. review or catalogues by Dulk, 1985; Güdel & Benz, 1988; Isliker & Benz, 1994). A

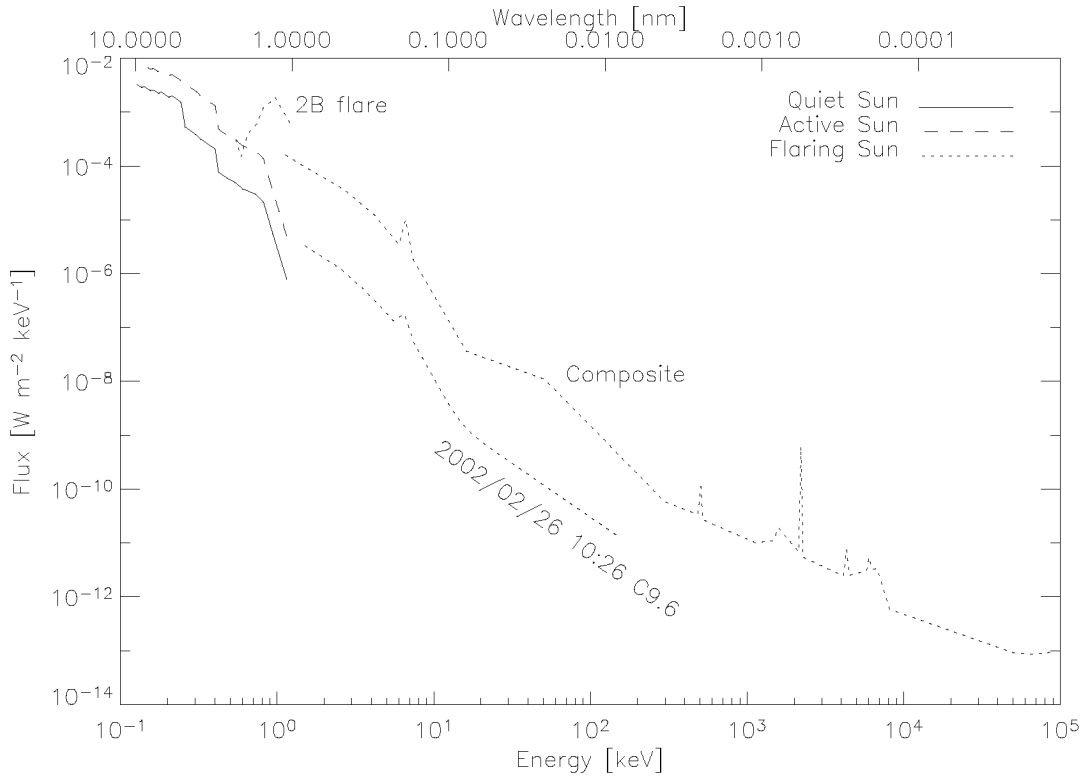


Figure 1.4: The solar X-ray spectrum. The *composite* is from [www resource \(3\)](#), the quiet/active components from [Livingston & al. \(1991\)](#), the 2B flare from [Styx \(2002\)](#), and the 2002/02/26 flare directly from RHESSI data.

first class of bursts, occurring usually in the microwave (1-30 GHz), mm and sub-mm regions, are believed to be caused by gyrosynchrotron or synchrotron radiation. Such bursts rarely last longer than a few minutes.

Plasma emission occurs more often at dm and meter-wavelengths (type IIIs have been observed by spacecraft at much longer wavelengths, in the solar wind). Some radio bursts are short-lived (individual Type III bursts, believed to be caused by electron beams, last typically one second). Type II shock waves may last several minutes. Type IV pulsations may last up to several hours, and Type I noise storms may last a whole day.

The *dashed lines* in Fig. 1.2 are envelopes of the very strongest bursts observed.

1.1.2 Infrared 1mm–0.75 μ m

44% of solar energy is from $>800\text{nm}$ light, but a good portion of the infrared part of the solar spectrum does not reach Earth ground level, because of large absorption features from mostly H_2O and CO_2 (see e.g. [www resource](#), 2). In the far infrared (FIR, 30–1000 μm), the solar cycle variability is less than 0.5%. In the mid infrared (MIR 5–30 μm) (or intermediate infrared, IIR) and the near infrared (NIR, 0.7–5 μm), the variability is even less: $<0.1\%$.

1.1.3 Visible or optical 750–380 nm

Almost all of the energy coming from the Sun and reaching the ground is in the visible part of the spectrum. The shape is not a perfect black-body spectrum, though, as several strong absorption lines are present, like the 6563Å $H\alpha$ line. With a sufficiently narrow-width filter, this line can be seen to emit from chromospheric regions, and is often used to detect and classify optical flares. Other so-called “forbidden” lines from the solar corona are also observed. They are dubbed “forbidden” because their transition would be impossible at Earth-like densities, were collisional de-excitations would dominate. Some of those lines are 100 times more intense than their neighboring continuum (e.g. FeXIV at 530.29nm, CaXV at 569.45nm, or FeX at 637.45nm).

The solar corona produces only about 10^{-6} times the optical luminosity of the Sun. The “K” (Kontinuum) corona is heavily polarized by Thomson scattering, whereas the “F” (Fraunhofer) corona, which dominates outward of 2–3 solar radii scatters mostly off dust particles.

The optical output of the Sun is hardly altered by a flare event: Only the most powerful flares show features in “white light”, as first noticed by Carrington in 1859. In dim M-stars, it has been observed to vary a lot more: Karpen et al. (1977) report a luminosity increase of up to an order of magnitude in the U band, a factor 4 in the B band, and a factor ~ 1.7 in the V band. Kahler et al. (1982) also reported substantial increases in the Balmer lines (see also Güdel, 2002).

1.1.4 Ultraviolet 380–10 nm

The ultraviolet band is divided into near ultraviolet (NUV, 380–200 nm), far ultraviolet (200–120nm), extreme ultraviolet (EUV, 120–10 nm), and sometimes XUV (<30 nm). There are further three “biological bands”: UV–A (380–315 nm, composing 99% of the ultraviolet light reaching the ground), UV–B (315–280nm), and the germicidal UV–C (280–10 nm). No radiation shorter than 280nm reaches the ground (O_2 and O_3 absorption). Shorter wavelength radiation is hence sometimes dubbed “vacuum ultraviolet” or VUV. Below 150nm, emission lines dominate the spectrum, of which the Lyman- α (1215.67Å, width $\sim 1\text{\AA}$) line is the most prominent: 6 mW/m², or about as much as the whole spectrum below 150nm besides Ly- α !

Figure 1.3 shows that the ultraviolet flux reaching the ground (i.e. longer than 280nm) varies by less than 0.1% during a solar cycle, or about the same as the total solar irradiance. Hence, sun bathers do not feel the difference between solar minimum and solar maximum. Shorter wavelengths vary by a factor ~ 2 between solar minimum and solar maximum, although some individual lines vary by up to a factor 100 (OVIII, FeXVI)!

In the powerful X17 Flare on 28 October 2003, Woods et al. (2004) have observed increases of factors 2–3 in EUV (~ 27 –115 nm) spectral irradiance, with individual lines varying by 10% (MgII 280nm) or 20% (Ly- α core), up to factor 17 (SiIII 120.6nm). Above ~ 120 nm, the ratio decreases progressively to a factor ~ 1 around 170nm and longer wavelengths.

Most of the UV continuum ($\gtrsim 310$ nm) comes from the photosphere, whereas most UV lines come from higher up: chromosphere, transition region, or the corona. Emission below ~ 30 nm comes mostly from the corona, while emission between ~ 30 and 140nm comes mostly from chromospheric regions. The EUV limb is 5–10 arc seconds above the photospheric limb.

1.1.5 Soft X-rays 10–0.1 nm (~ 0.1 –10 keV)

Very few soft X-rays (SXR) are witnessed during solar minimum. As can be seen in Fig. 1.5, a lot more (about a factor 10 in *Yohkoh* SXT’s 0.25–4 keV band) are present during solar maximum. They are emitted in the

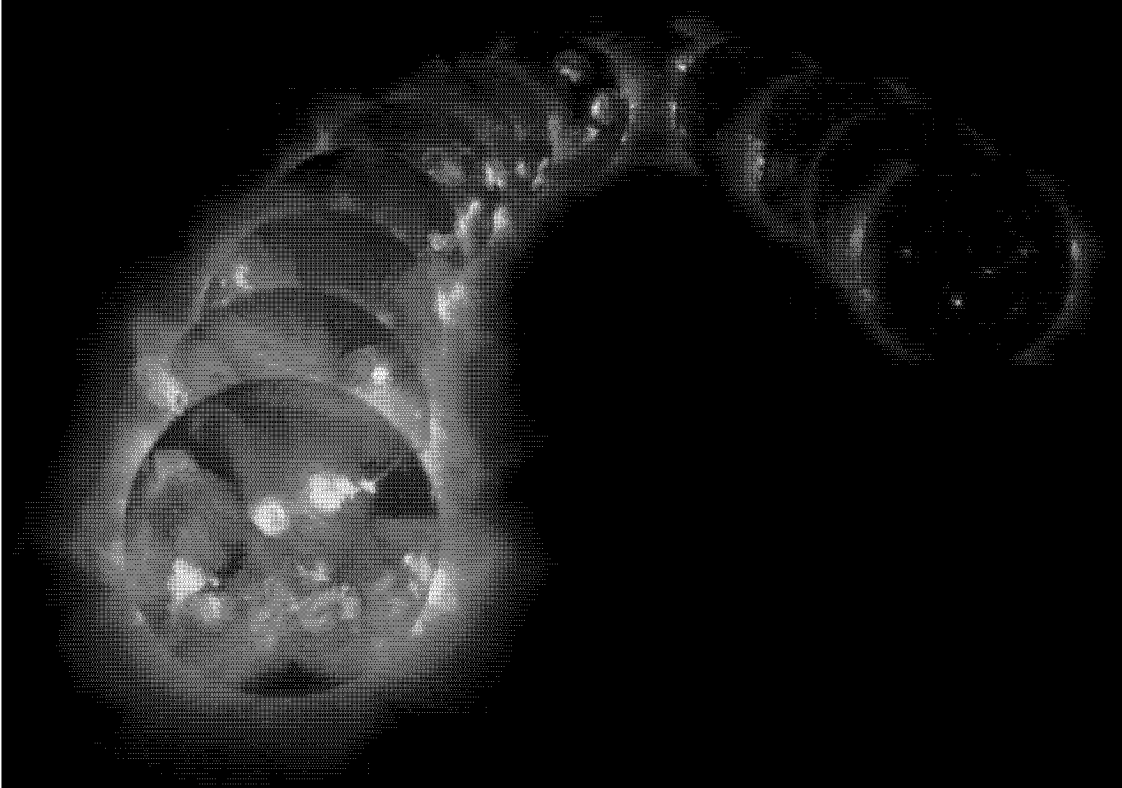


Figure 1.5: The changing Sun, in soft X-rays, as seen from the Soft X-ray Telescope (SXT, 0.25–4 keV, Tsuneta et al., 1991), on board the Japanese *Yohkoh* satellite. *Left:* Solar maximum. *Right:* Solar minimum.

solar corona, at altitudes of a few thousand kilometers.

The FeXXVI 6.7 keV line is one of the highest-energy important spectral lines of hot plasmas. Beyond ~ 8 keV, only free-free bremsstrahlung emission occurs.

In the powerful X17 Flare on 28 October 2003, Woods et al. (2004) have observed increases of factor ~ 50 in irradiance from wavelengths between 0.1 to 7nm, and a factor 570 increase in 0.1-0.8nm. In solar physics, SXR often refers to the thermal part of the photon bremsstrahlung spectrum, which can go up to ~ 20 keV in powerful flares.

1.1.6 Hard X-rays 10–300keV

Hard X-rays are usually present only during flare events.

In solar physics, HXR often refer to the non-thermal, power-law like

part of the photon spectrum. I.e. rather than being associated to a specific energy band, they are associated with the physical process of bremsstrahlung of fast ($\gtrsim 0.2\text{--}0.3 c$) electrons.

1.1.7 Gamma-rays >300 keV

Gamma rays are only present in the most powerful of solar flares.

In solar physics, they are usually associated with emission from nuclear processes, such as the nuclear lines from excited nuclei, as well as the delayed neutron capture line (2.223 MeV), and the electron-positron annihilation line and continuum (Share & Murphy, 2004). So far, they have been witnessed in less than ~ 100 solar flares, and *never* from other flaring stars (Share & Murphy, 2004).

1.2 Emission mechanisms

This section briefly explains and characterizes emission mechanisms that are the cause of most of the X-ray and radio emission of the Sun. They can be divided in two broad classes: *coherent* and *incoherent* emissions. *Coherent* emission mechanisms include *plasma emission* and the *electron-cyclotron maser* mechanisms. *Incoherent* emission mechanisms include *bremsstrahlung* and *gyro-emission*.

In the solar case, X-rays are believed to be emitted only by bremsstrahlung, whether thermal or non-thermal.

1.2.1 Bremsstrahlung

When a fast *charged* particle encounters an atom, molecule, or ion, it is decelerated and emits radiation called bremsstrahlung (free-free radiation). For radio waves, distant encounters of electrons with ions (causing small-angle deflections) are much more important than the relatively rare close encounters and large deflections. For a detailed discussion on bremsstrahlung emission, the interested reader is referred to e.g. Longair (1992); Lang (1999); Dulk (1985). The total energy spectrum radiated

during one (even relativistic) collision is given by:

$$W(\nu) \approx \begin{cases} \frac{8}{3\pi} \frac{Z_i^2 e^6}{m_e^2 c^3 b^2 v^2} & \text{for } \nu > \nu_c \\ 0 & \text{for } \nu < \nu_c \end{cases} \quad (1.1)$$

where Z_i is the ion's atomic number, e the elementary charge, c the speed of light, v the velocity of the particle, b the impact parameter, and $W(\nu)$ is in ergs Hz^{-1} , $\nu_c \approx \frac{\gamma v}{b}$, with γ the Lorentz factor of the incoming particle. CGS units have been used throughout. The collision time is $\tau \approx \frac{2b}{\gamma v}$. The spectral energy radiated is flat up to the critical frequency ν_c , then falls off exponentially.

The radiated spectrum of a distribution of particles is a summation of Eq. (1.1) over all possible impact parameters, which is not trivial. The interested reader is referred to the above publications for more on this.

The spectral flux at Earth of a maxwellian flare plasma ($T > 3.6 \times 10^5$ K) from radio to X-rays is (from Lang, 1999; Dulk, 1985):

$$F_\nu = 1.33 \times 10^{-46} n_\nu Z^2 \ln \left(4.7 \times 10^{10} \frac{T}{\nu} \right) \frac{EM}{\sqrt{T}} e^{-\frac{h\nu}{kT}} \text{ [SFU]} \quad (1.2)$$

in a notation appropriate for the radio part of the spectrum. For the X-ray region, a more appropriate notation might be:

$$F_\epsilon = 5.9 \times 10^{-43} n_\epsilon Z^2 \ln \left(2 \frac{kT}{\epsilon} \right) \frac{EM}{\sqrt{T}} e^{-\frac{\epsilon}{kT}} \text{ [ph s}^{-1} \text{ cm}^{-2} \text{ keV}^{-1}] \quad (1.3)$$

where $n_{\nu,\epsilon}$ is the refractive index of the medium, Z the average atomic number (usually 1.2 in the solar corona), EM the emission measure in cm^{-3} , T the plasma temperature in K, ν the frequency in Hz (or ϵ the photon energy in keV), and 1 Solar Flux Unit (SFU) = $10^{-22} \text{ W m}^{-2} \text{ Hz}^{-1}$. If $\nu \lesssim \nu_p$ (the plasma frequency), then ν_p should be used instead of ν in the logarithm term.

Bound-bound line emission must be added to the free-free continuum. Line emission is also proportional to EM , and is very temperature-dependant.

Because of self-absorption, the spectrum has in fact a black-body shape at low frequencies (see Fig. 1.6).

For non-thermal bremsstrahlung, the reader is referred to Chapter 5 or Appendix A.

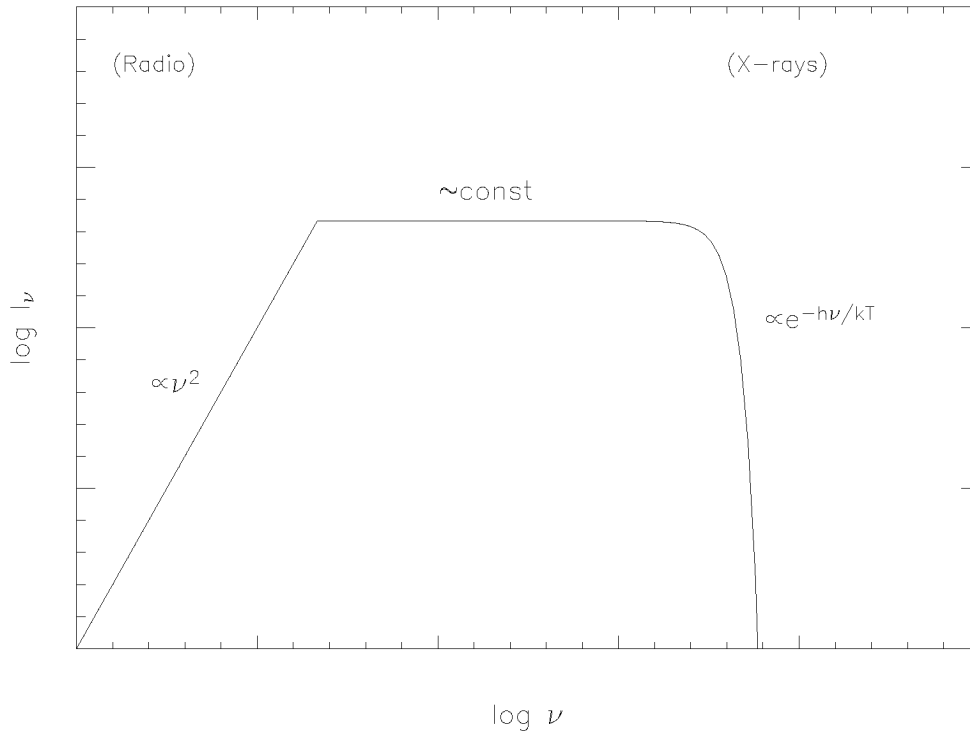


Figure 1.6: Thermal bremsstrahlung intensity. At low frequencies, self-absorption causes the intensity to behave as a black-body: $I_\nu = B_\nu = 2k_B T \frac{\nu^2}{c^2}$ (in the Rayleigh-Jeans limit). In the optically thin region, $I_\nu = \frac{F_\nu}{\pi \left(\frac{\phi_A}{2}\right)^2}$. ϕ_A is the source's angular diameter, and F_ν is given by either Eqs. (1.2) or (1.3).

1.2.2 Gyro-emission

When a plasma contains a magnetic field, accelerations due to particle collisions may be negligible in comparisons with those due to gyration around the field lines. Gyro-emission from non-relativistic particles is called gyro-resonance emission. It is called gyrosynchrotron in the case of mildly relativistic particles ($\gamma = 1.2-3$), and synchrotron in the case of relativistic particles ($\gamma \gg 1$). Because free-free spectral emissivity goes as $n^2 T^{-1/2}$ and thermal gyrosynchrotron goes as $n T^\alpha B^\beta$ (with $\alpha, \beta > 1$), it can follow that the former mechanism dominates at the lower frequencies, and the latter at higher frequencies.

Gyromagnetic radiation from mildly-relativistic to relativistic electrons with a power-law distribution in energy $f(E) \propto E^{-\delta}$, yields a

power-law photon energy spectrum $F_\nu \propto (h\nu)^\alpha$ with spectral index $\alpha = 1.22 - 0.9\delta$ for the gyrosynchrotron case and $\alpha = 0.5 - 0.5\delta$ for synchrotron emission (Dulk & Marsh, 1982; Dulk, 1985). Towards lower frequencies, self-absorption occurs as the medium becomes optically thick, and the spectrum drops at lower frequencies, with $\alpha = -2.9$ (for gyrosynchrotron) or $\alpha = -2.5$ (for synchrotron) spectral index (Dulk & Marsh, 1982). The Razin-Tsytoich suppression (due to the increase of the refractive index in the neighborhood of the local plasma frequency) might cause the spectrum to fall even more steeply. Gyrosynchrotron emission from a thermal distribution of electrons has $\alpha = 2$ below the critical frequency, and -8 above. See e.g. Dulk (1985) for a more complete discussion, including polarization and peak emission frequency considerations.

1.2.3 Electron-Cyclotron Maser

The basic requirements for a microwave amplification by stimulated emission of radiation to operate are (a) a population inversion in the electron distribution, and (b) a relatively strong field or low-density plasma such that $\nu_B \gtrsim \nu_p$, where the electron gyrofrequency ν_B is:

$$\nu_B = \frac{1}{2\pi} \frac{eB}{m_e c} = 2.8B \text{ [MHz]}, \quad (1.4)$$

where B is in Gauss.

If the latter condition is not met, the free energy is likely to go into various plasma waves rather than directly into EM radiation. The most common form of population inversion is the loss-cone distribution. A loss-cone may be produced by an electron distribution being mirrored at the foot points of magnetic loops: The electrons with the highest velocities along the magnetic field are not mirrored and are lost. Radiation is believed to be mostly at the fundamental or harmonic of ν_B .

1.2.4 Plasma emission

Plasma emission is an indirect emission process, where the exciting agent (e.g. a propagating beam of electrons) generates plasma waves which cannot escape directly from the plasma (e.g. Langmuir waves). This turbulence leads to escaping EM radiation through some secondary process,

e.g. scattering off ions or other waves. Emission typically occurs at the fundamental or second harmonic of the local plasma frequency:

$$\nu_p = \frac{1}{2\pi} \sqrt{\frac{4\pi e^2 n_e}{m_e}} = 8977 \sqrt{n_e} \text{ [Hz]} \quad (1.5)$$

For plasma emission to occur, a positive slope in electron velocity space is needed (the “bump-in-tail” instability is the arch-typical example): Particles close to resonance tend to be dragged into resonance, like a surfer catching a wave. If the particles are slightly slower than the wave, they tend to speed up, gaining energy from the wave. If they are slightly faster, they tend to slow down, giving energy to the wave. A particle distribution with a negative slope (such as a maxwellian distribution) will damp waves (Landau damping), as there are always more particles slightly slower (taking energy from the wave) than particles slightly faster (giving energy to the wave). Wave growth/damping time is of the order of the plasma period, hence very fast.

Solar radio bursts are believed to be mostly caused by plasma emission, and can reach brightness temperatures beyond 10^{10}K !

1.3 The standard solar flare scenario

Magnetic fields are believed to be the cause of flares. They are generated in the convective region, just below the photosphere, by the solar dynamo, and can have photospheric strengths of up to 3000 Gauss (0.3 T), but only ~ 100 G in the corona. In the corona, when magnetic field lines of opposite polarity get close to one another, the magnetic field gradient may become very strong. Magnetic field lines diffuse towards the region of low magnetic field amplitude, and reconnect (Sweet, 1958; Parker, 1957; Petschek, 1964; Priest & Forbes, 1986; Priest & Lee, 1990). This process diminishes the energy stored in the magnetic field: It is transformed into ohmic heating of the plasma and/or particle acceleration, as well as bulk motion.

Several acceleration mechanisms have been proposed, and are discussed in e.g. Miller et al. (1996, 1997); Kirk, Melrose & Priest (1994); Benz (2002a): Shock-drift acceleration (or fast-Fermi process), diffusive shock acceleration, DC electric fields, and stochastic acceleration pro-

cesses, including Transit-Time Damping. Particles are probably accelerated using combinations of the above processes. Discrimination is particularly difficult, as the mechanisms have apparently no direct signature, except, perhaps, metric narrow band radio spikes (Paesold et al., 2001) or type III radio bursts.

More generally, the phenomenon of particle acceleration may be viewed as follow: Reconnection generates a lot of plasma waves or turbulences, which act as randomly moving magnetic mirrors. These mirrors stochastically accelerate particles, as head-on encounters (where a particle gains energy) are more frequent than rear-on encounters (where a particle loses energy).

Both stochastic acceleration theories (Fermi, 1949; Benz, 1977) and simulations (Miller, 1998b, 2000) predict near power-law shapes of the electron distribution spectrum above the thermal distribution. Simulations also show a break in the power-law. Solar flares often possess breaks in their photon spectra.

Once accelerated, particles (electrons up to 100's of MeV, ions up to 10's of GeV) spiral along magnetic field lines. Particles connected to open field lines are lost in interplanetary space, while others precipitate down in the lower corona or upper chromosphere. HXR emission near the reconnection point is sometimes observed (Masuda, 1994), and is believed to be created by bremsstrahlung of the accelerated electrons (bremsstrahlung by ions is negligible in comparison) through the upper corona. As the medium has a small density, negligible energy losses are thought to occur ("thin-target model"). Radio type III burst may be emitted by the bump-on-tail plasma instability, where Langmuir waves are generated and may be converted into observable transverse electromagnetic waves (see e.g. Benz, 2002a). Gyro-emission (magneto-bremsstrahlung) is also often observed. As the particles precipitate towards the denser lower corona or upper chromosphere ($\sim 10^{13} \text{ cm}^{-3}$), they lose their energy very rapidly by coulomb collisions, simultaneously emitting bremsstrahlung radiation (thick-target model, Brown, 1971). There, they heat the ambient plasma to tens of MKs' (Neupert, 1968; Dennis & Zarro, 1993). This hot chromospheric material evaporates and fills magnetic loops, emitting thermal bremsstrahlung radiation in SXR that can last an hour or more for a large event. As this plasma cools down to lower temperatures, EUV lines are activated, and radiative cooling becomes much more effective. Some of the plasma can be ejected as a plasmoid (Khan et al., 2002), and emit

Quantity	Typical value
Length scale	10^9 cm
Volume	10^{27} cm ³
Coronal density	10^{10} cm ⁻³
Energy	10^{32-33} ergs
Accelerated electrons	10^{38}
Duration	10^{2-3} s
Plasma temperature	$4-5 \times 10^7$ K
Electron and ion energies	equipartition
³ He/ ⁴ He	~ 1 ($\times 2000$ enhancement)
Fe/O	~ 1 ($\times 8$ enhancement)
H/He	~ 10 ($\times 0.1$ enhancement)

Table 1.1: *Some characteristics of a large solar flare.* While most accelerated electrons are observed to be in the 10–20 keV range, electrons above 10’s of MeV are also observed (Miller et al., 1997). Ions, when observed (via their gamma-ray line signatures), have energies above 1 MeV/nucleon, and can reach ~ 100 MeV/nucleon (Miller et al., 1997). Large X-class flares may occur at a rate of ~ 1 per week during solar maximum. At the other end of the scale, *nanoflares* ($\sim 10^{24}$ ergs) are thought to occur continuously.

decimetric radio emission from its trapped electrons.

The ejected plasma can also form a Coronal Mass Ejection (CME), which magnetic fields can wreak havoc on Earth or artificial satellites. Such CMEs are visible in optical light by Thomson scattering of photospheric light off the denser material.

Figures 1.7, 1.8, 1.9, and 1.10 offer a visual snapshot of a flare. Table 1.3 gives some typical flare characteristics.

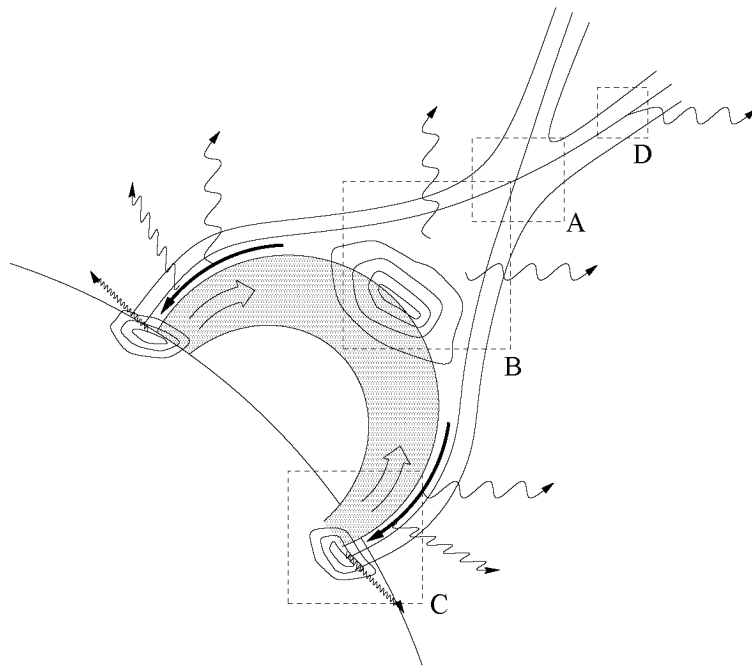


Figure 1.7: Canonical flare scenario (from Paesold, 2002). *A*: Site of initial energy release, by magnetic reconnection *B*: Site of particle acceleration. HXR loop top sources and radio spikes are sometimes present. *C*: Particles follow field lines, emitting gyromagnetic emission (gyrosynchrotron, synchrotron) as they spiral down into the chromosphere. They may also cause beam instabilities, and dm type III radio bursts. As they reach the denser lower corona or upper chromosphere, they will emit HXR by bremsstrahlung, and rapidly lose their energy by Coulomb collisions, thereby heating the ambient medium, and causing “chromospheric evaporation”, i.e. very hot plasma rises and fills the magnetic loop, and emits SXR by thermal bremsstrahlung. *D*: Other accelerated particles may escape along open field lines into interplanetary space, causing metric type III bursts. Some might even be trapped in plasmoids and CMEs, generating type IV radio bursts.

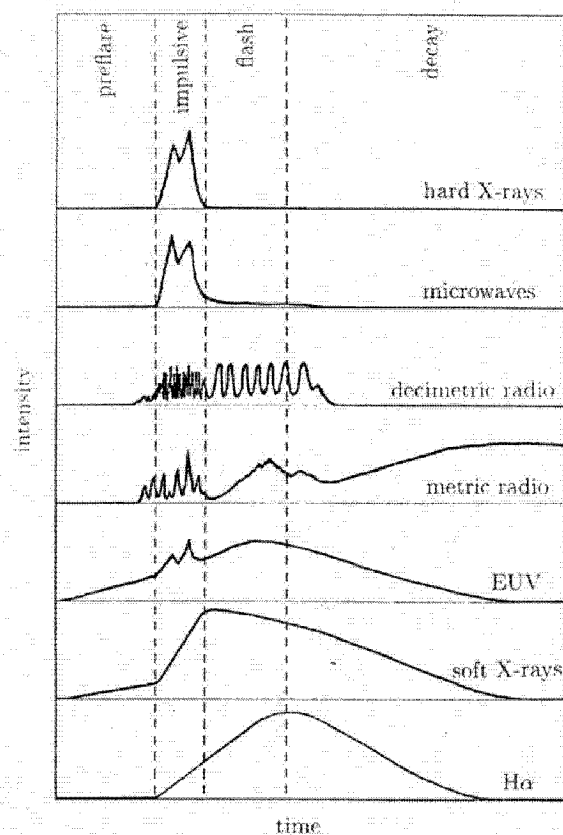


Figure 1.8: Schematic time profiles of flares in different wavebands (from Benz, 2002a). In large events, HXR and microwave typically last one minute (impulsive phase), whereas the decay phase may last one hour or more.

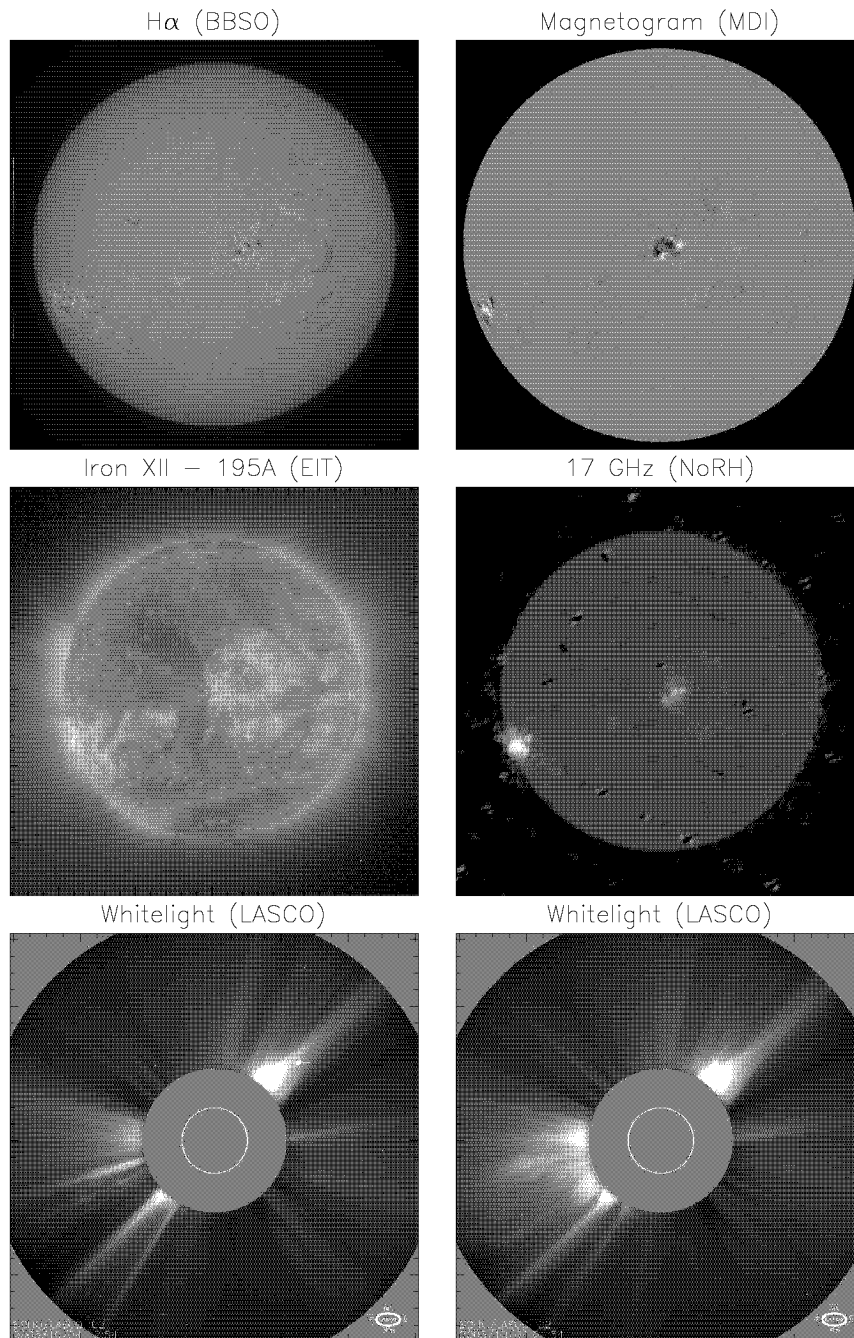


Figure 1.9: Full Sun images. The pictures were taken at times close to the 2003/10/24 02:45 M7.9 flare, which occurred on the southeastern part of the solar limb. See Fig. 1.10 for more details. The first four pictures show the active/flaring regions on the Sun. The *bottom* two pictures show the optical corona before and after the flare: A CME can clearly be seen in the process of being ejected.

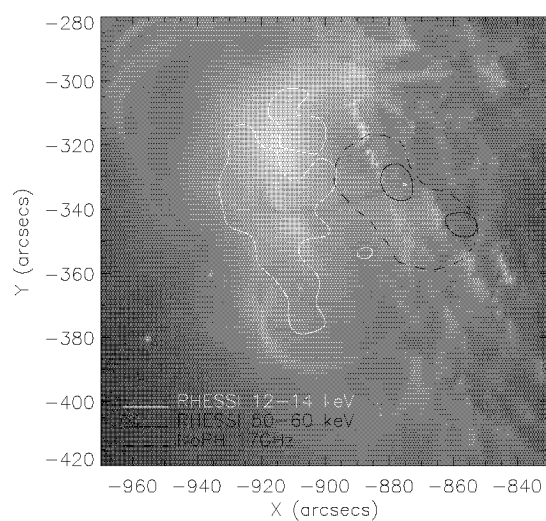


Figure 1.10: TRACE 195Å image with RHESSI and Nobeyama 17GHz contours, on 2004/10/24, around 02:45. The 50–60 keV and the 17GHz contours show the foot point sources. The 12-14 keV contour show the thermal plasma, possibly loop-top sources as well.

Chapter 2

Hard X-ray, ejecta, and their associated decimetric radio emission in solar flares

The only true wisdom is in knowing you know nothing.

Socrates (469–399 BC)

No man should escape our universities without knowing how little he knows.

J. Robert Oppenheimer (1904–1967)

ABSTRACT: We investigate temporal and spatial correlations in solar flares of hard X-rays (HXR) and decimetric continuum emissions, ejecta, and CMEs. The focus is on three M class flares, supported by observations from other flares. The main conclusions of our observations are that (1) major hard X-ray flares are often associated with ejecta seen in soft X-rays or EUV. (2) Those ejecta seem to start before HXR or related decimetric radio continua (DCIM emission). (3) DCIM occurring nearly simultaneously with the first HXR peak are located very close to the HXR source. Later in the flare, DCIM generally becomes stronger, drifts to lower frequency and occurs far from the HXR source. Thus the positions

at high frequency are generally closer to the HXR source. DCIM emission consists of pulses that drift in frequency. The very high and sometimes positive drift rate suggests spatially extended sources or type III like beams in an inhomogeneous source. Movies of selected flares used in this study can be found online¹.

2.1 Introduction

The release of non-potential magnetic energy in the corona accelerates charged particles to supra-thermal energies. Accelerated particles emit a variety of temporary radiations generally termed *flares*. Depending on wavelength and type of emission, they yield information on the propagation, thermalization and further development of the flare energy. Most prominent are hard X-rays (HXR, $\gtrsim 10$ keV) emitted as bremsstrahlung of energetic electrons losing energy by collisional interactions. They yield estimates of flare energies with a range beyond 10^{32} erg, of the number of accelerated electrons up to 10^{38} , and of electron energies up to 100 MeV. Other emissions include gyrosynchrotron radiation from decimeter to millimeter waves, produced by relativistic electrons in kilogauss magnetic fields, and gamma-ray lines due to impinging energetic ions.

The common feature of all the above emissions is that they are produced by energetic particles, the product of acceleration. The region of hard X-ray and gamma-ray emission is usually not the acceleration site, but some target plasma often at higher density and lower altitude. Thus the emissions give only indirect information on the acceleration process that has remained enigmatic for this reason since many decades. The theoretical work has recently concentrated on stochastic acceleration by Transit-Time Damping, but field aligned electric fields and shock waves may also play a role (cf. review by Miller et al., 1997).

It is surprising that the very process of acceleration of such overwhelming dimensions in our astronomical neighborhood should be hidden to direct observation. It is not even clear where acceleration occurs. The large number of electrons and the huge amount of energy involved point to a low altitude for the energy release site. On the other hand, time-of-flight measurements of electrons at different energies using HXR peaks rather suggest a high injection site (Aschwanden et al. 1998).

¹http://www.astro.phys.ethz.ch/papers/shilaire/HXRDCIM_CDROM_material/

Coherent radio emissions, characterized by relatively small bandwidths and high polarization, have been observed during flares from meter wavelengths up to 8 GHz (Bruggmann et al. 1990). Such emissions are sensitive signatures of deviations from thermal electron distributions driving plasma instabilities. In particular, beams of electrons, trapped electrons, unstable currents and shocks are known or suspected sources of coherent radio emission. They are radiated at the local plasma frequency, upper hybrid frequency, electron gyrofrequency, or their low order harmonics. Therefore, the observed range of coherent bursts includes source densities up to $4 \times 10^{11} \text{ cm}^{-3}$ (second harmonic) and magnetic field strengths up to about 1000 G (third harmonic). These limits include the plasma parameters generally expected in the flare acceleration site (e.g. Miller et al., 1998). Thus, the decimeter wavelengths are the range to search for coherent emissions from the accelerator.

Extremely narrowband and short spikes at decimeter waves (reported in the range 200 MHz to 8 GHz) have been suspected to be more directly related to the acceleration site than any other emission. The hypothesis includes two parts: spatial coincidence of the radio source and the acceleration site as well as a similarly high degree of fragmentation (Benz, 1986). Evidence comes mainly from the excellent correlation of spikes at meter waves and type III radio bursts, which sometimes seem to emanate from a group of metric spikes in the spectrum (Benz et al., 1996) and in space (Paesold et al., 2001). However, these metric spikes and type III bursts are often not associated with reported HXR emission and tend to have no counterparts in $\text{H}\alpha$. Furthermore, their location is high in the corona, and the energies involved are small (less than 10^{27} erg, Krucker et al., 1995). On the other hand, spikes in the *decimeter range* are well associated with HXR emission. However, the converse is not true: HXR bursts are associated with decimetric spikes only to $\geq 2\%$ (Güdel et al., 1991). Decimetric spikes are thus at most a sporadic signature of acceleration. This is also the conclusion of a recent investigation of the temporal and spatial association of decimetric spikes with HXR and thermal flare emissions (Benz et al., 2002).

Various forms of "pulsations" or broadband fluctuations have been known to occur in the decimeter range before, during, and after flares (cf. catalogues by Güdel and Benz, 1990; Isliker and Benz, 1994). A very regular subtype of them has been interpreted as MHD oscillation of a magnetic flux tube containing trapped electrons and modulating their

emission due to a loss-cone velocity distribution (Roberts and Mangeney, 1982) or as a limit cycle (Lotka-Volterra type) oscillation between precipitation and loss-cone instability (Aschwanden and Benz, 1988). Only 20% of those regular pulsations are associated with HXR emission, in which case the correlation is generally weak (Aschwanden et al., 1990). More recently, Kliem et al. (2000) have studied an event of irregular pulsations associated with HXR emission. The radio burst consists of irregular pulses with a bandwidth of 500 MHz at a center frequency of initially 1.5 GHz, drifting to lower frequency in the course of the event. The authors interpret the radio emission as a direct signature of reconnection. Similar events have been studied by Hori (1999), Khan et al. (2002), Karlicky et al. (2002), and others.

The previous studies have selected a certain type of radio burst and searched for associated HXR. Here we present a study applying the opposite approach: major HXR events have been selected and their radio emission in decimeter waves are studied in the spectrum and location relative to the HXR source. The HXR source is taken as indication for the site of prime flare energy deposition. A first step is to find direct radio signatures of the acceleration process, as close in time and space as possible. If such an emission exists, the radio spectrum can be used to investigate the nature of the emission and possibly reveal properties of the acceleration process.

2.2 Instruments and data selection

Our investigation combines temporal and spatial data on HXR emission with spectral and spatial information on associated radio emission at decimeter wavelengths. In addition, SXT and EUV images of the thermal coronal plasma background were used to put the non-thermal sources into the general context of the associated active region.

2.2.1 The YOHKOH Hard X-ray Telescope (HXT)

HXT (Kosugi et al., 1991) imagery has a spatial resolution of 5 ". It sees mostly the HXR produced by the bremsstrahlung of non-thermal electrons hitting the chromosphere or lower corona. Those high energy electrons are presumably accelerated by the flare process occurring in the

corona, and are hurled along magnetic field lines into the denser chromosphere. The HXT has four energy channels. In this investigation, only the lowest channel (14-23 keV) was used for imaging, as it usually has the most counts.

2.2.2 The Phoenix-2 spectrometer

The Phoenix-2 (Messmer et al., 1999) radio spectrometer was programmed to observe the low decimeter range simultaneously with the Nançay Radioheliograph several months per year. The resulting spectrograms have a time resolution of 0.1 seconds, a frequency resolution of 1 MHz, and span the 220-553 MHz range. The Sun is surveyed continually (from sunrise to sunset). Stokes I and V data are usually available, except for part of 1999, where only one (linear) polarization was measured. The spectrograms have been background-subtracted, and some channels with interferences were removed.

2.2.3 The Nançay Radioheliograph (NRH)

The NRH (Kerdran & Delouis, 1996) surveys and images the Sun continually at the following frequencies: 164, 236.6, 327, 410.5 and 432 MHz. Used NRH data were of two types:

- 120 ms time resolution, with 30" pixel resolution
- 10 seconds integrated data, with 15" pixel resolution

The second set² was used most often, as it has higher pixel resolution, takes less space on the hard disk, and the low time resolution is good enough for our needs.

The instrument has a nominal half-beamwidth of 1.96 arcmin at 164 MHz. It gets proportionally better at the higher frequencies. The relative accuracy (in arcseconds) of the position of a source centroid is hence given by the formula $\frac{118''}{\sigma} \frac{164}{\nu}$, where σ is the signal-to-noise ratio, and ν the frequency in MHz. The absolute accuracy of NRH maps is of the order of 50".

²<http://mesola.obspm.fr/>

2.2.4 The Yohkoh Soft X-ray Telescope (SXT)

The SXT (Tsuneta et al., 1991) provides full and partial disk images in the 0.25-4 keV range (i.e. sensitive to plasmas ≥ 2 MK), with pixel sizes down to 2.45". It monitors mostly the bremsstrahlung emission of the thermal plasma present in the corona. Five different filters can be positioned in front of the detector array to estimate isothermal temperatures and emission measures.

2.2.5 The Transitional and Coronal Explorer (TRACE)

TRACE (Handy et al., 1999) observations were carried out mostly with filters having the following wavelength bands:

- 1600Å : (bandwidth of 275Å, temperature range: 4.0-10.0 kK) sees chromospheric material in quiescence: the UV continuum, the CI and FeII lines, as well as the 200 kK CIV line in flares.
- 171Å: (bandwidth of 6.4Å, temperature range: 0.16-2.0 MK) sees coronal material: the FeIX and FeX lines.

As TRACE images tend to have an offset (of up to about 10 ") in their pointing, they have been shifted in order to fit more properly the Sun's limb (or EUV limb, for the EUV images), as best as was visually possible.

2.2.6 Other data

We have supplemented the set of data if necessary by observations from the Ondrejov spectrograph (0.8 to 4.5 GHz) (Jiricka et al., 1993) and the CGRO-BATSE (Fishman et al., 1989) instrument, which can detect photons in the 25 to 1000 keV range.

2.2.7 Selection of Events

The events have been selected according to the following criteria:

- Intensive HXR emission: as a proxy for HXR, we used the NOAA (National Oceanographic and Atmospheric Administration) Solar Event Report ³, looking for gyrosynchrotron radio emission above 10 GHz.
- Yohkoh HXT imagery had to be available, in order to determine the HXR sources' positions.
- Simultaneous Phoenix-2 spectrograms were required, showing decimetric radio continua (DCIM). The frequency range for those spectrograms must be 220-550 MHz in order to include the frequencies observed by the NRH.
- For position information of the bursts seen by Phoenix-2, radio imaging data from the NRH were mandatory.
- The events had to be as close to the limb as possible, where spatial information usually becomes more straightforward to use, and projection effects are less severe. This condition practically translated into taking events with locations beyond 45 degrees of solar longitude (east or west), as given by the NOAA Solar Event Report.
- To observe the spatial structure and temporal evolution of coronal loops, either Yohkoh SXT or TRACE images during each event were also required.

Very few events between 1999 and mid-2001 fulfilled all these stringent criteria, and had data deemed good enough for our study. A total of nine events were investigated. Three events (Table 2.1) had data that could be considered as 'nearly ideal' in all respects: all instruments in sunlight, looking at the same region of the Sun, and getting useful data. They will be the ones used in this study, although several other events, with poorer and/or partial data, were also examined closely to support the observations and conclusions made from the three best events.

At the web link provided at the beginning of this chapter, movies (in mpeg or javascript format) can be found of the three main events, and also of numerous other events. All movies show TRACE or SXT images, with overlaid contours from the NRH and HXT. See the *index.html* page

³[gopher://sec.noaa.gov/11/indices](http://sec.noaa.gov/11/indices)

Event	1999/09/08	2000/08/25	2001/06/15
Class	M1.4	M1.4	M6.3
AR	8690	9143	9502
Ejecta start time	12:08 to 12:12	?	10:02 to 10:05
HXR peak time(s)	12:14:00,12:14:40, 12:14:30	14:27:35, 14:31:00, 14:32:20	~10:07:20, 10:27:00, 10:30:30, 10:49:00
radio peak flux time 1.4 GHz	12:15	14:28:02, 14:31:47	~10:10, 10:27, 10:48:50
peak flux time 327 MHz	12:20:37	≈14:24 <small>(small)</small> , 14:31:39	10:07:22(typeII),≈10:14, 10:34:29,10:49:00,11:02:23
Brightness Temperature of brightest NRH pixel at peak flux (327 MHz)	150 MK	> 6000 MK	100 MK
pulse duration	0.5 secs	0.4 secs	≈ 0.4 secs
pulsation period	4-30 secs	≈8 secs	2.4 secs
Overall Drift rate (MHz/s)	-1.56 at 328 MHz (950 km/s)	-2.8 at 420 MHz (1200 km/s)	-4.3 MHz/s at 412 MHz
Drift rate of pulses (MHz/s)	> 1000 MHz/s at 430MHz	> 1300 MHz/s at 477MHz	-1190 MHz/s at 535 MHz
proj. radio source motion DCIM, 327 MHz	150 km/s	>300km/s	450 km/s
projected ejecta speed (km/s)	100 - 400 km/s	≈300 km/s	480 km/s
associated metric type III ?	starting right at 1st HXR peak	starting ~2 min. after first HXR peak	starting ~50s after HXR peak Type II starting ~30s after HXR peak
associated decimetric type III ?	none observed	(faint) starting to occur ~4 min. before HXR peak	(faint) starting to occur ~50s before HXR peak
HXR footpoint separation (Mm)	15"	17"	(35"), (HXR spikes all over), (35", same FPs as before)
distance nearest radio source to HXR (peak HXR flux)	10" (432MHz)	80"	20" other peaks: 90",90"
distance nearest radio source to HXR (peak radio flux)	90" (327 to 432 MHz)	100"	85" (SW) (100" (S) at 10:49)

Table 2.1: Observations summary for three prime events

at the above web site for further details. Most of the images shown in this chapter are actually snapshots from these movies, to illustrate the points that we want to emphasize. No doubt that the movies themselves provide an almost endless amount of additional details, but they are beyond the scope of this chapter. Here, we concentrate on a few major results.

2.3 Observations and results

Table 2.1 summarizes some characteristics pertaining to each of our three main events. Although they were not selected for these properties, all three had an ejecta observable in EUV or SXR, and meter wave type III bursts. Table 2.2, shows that most selected flares seem to have some kind of an ejecta, while metric type III bursts are not always witnessed.

Day	Time (UT)	Presence of meter type IIIs ?	EUV/SXT ejecta ?	Presence of CME ?
1999/09/08	12:15	yes	yes	no (?)
2000/08/25	14:28	yes	yes	yes
2001/06/15	10:07	yes	yes	yes
1999/06/11	11:16	no	?	yes
1999/06/12	13:31	no	?	no
2000/07/07		no	?	yes
2000/07/12	10:31	yes	?	yes
2000/08/12	09:50	yes	yes	yes
2000/09/14	14:40	yes	yes	no

Table 2.2: Some additional characteristics pertaining to the examined flares. A ‘?’ symbol means the data was not good enough for a clear-cut determination.

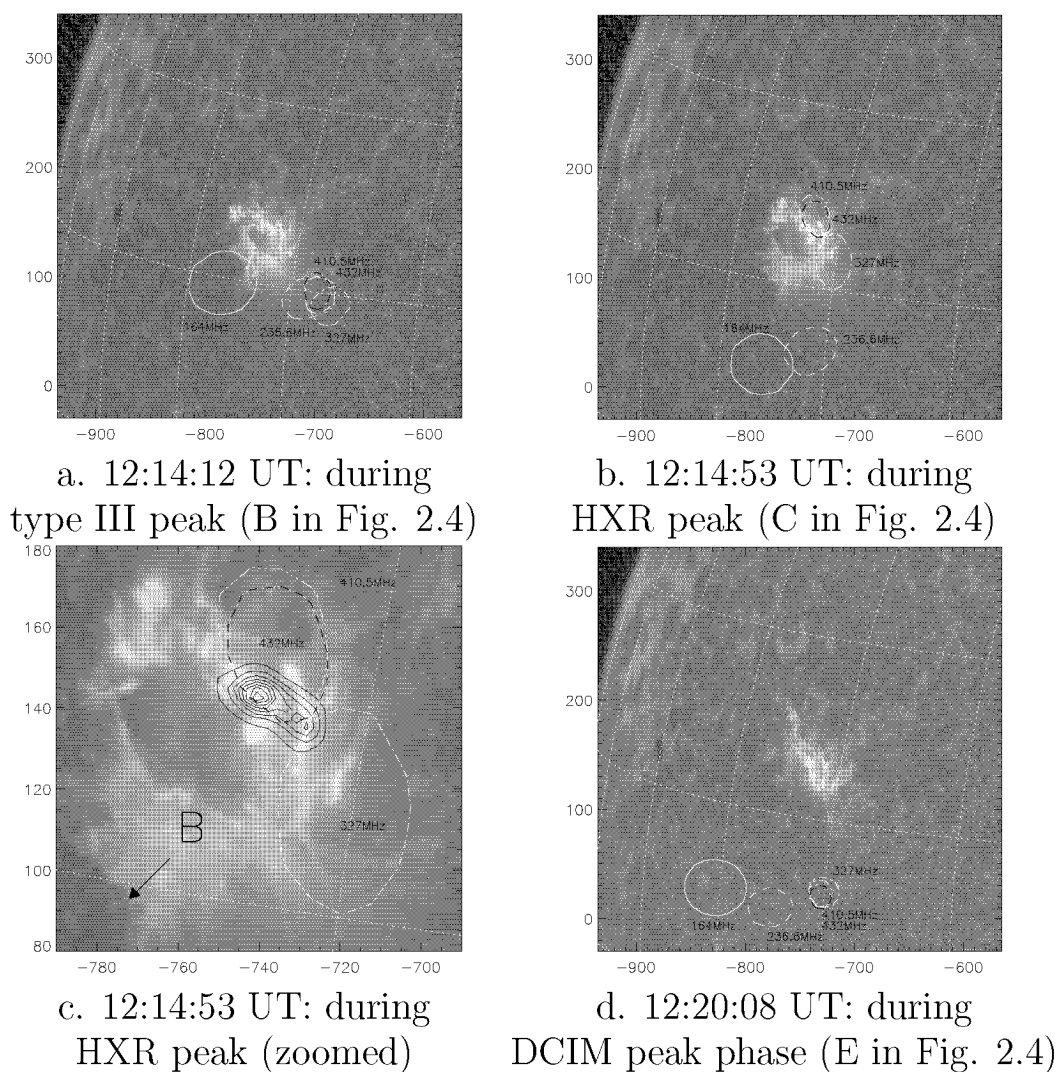


Figure 2.1: 1999/09/08 double-ribbon flare: TRACE 1600\AA images with NRH contours (98% level) at various frequencies, and HXT (23-33 keV band) overlay (solid isophotes in c). The units of the axes are arcseconds from Sun center. The ejecta (‘B’) and its motion (arrow) are marked in c.

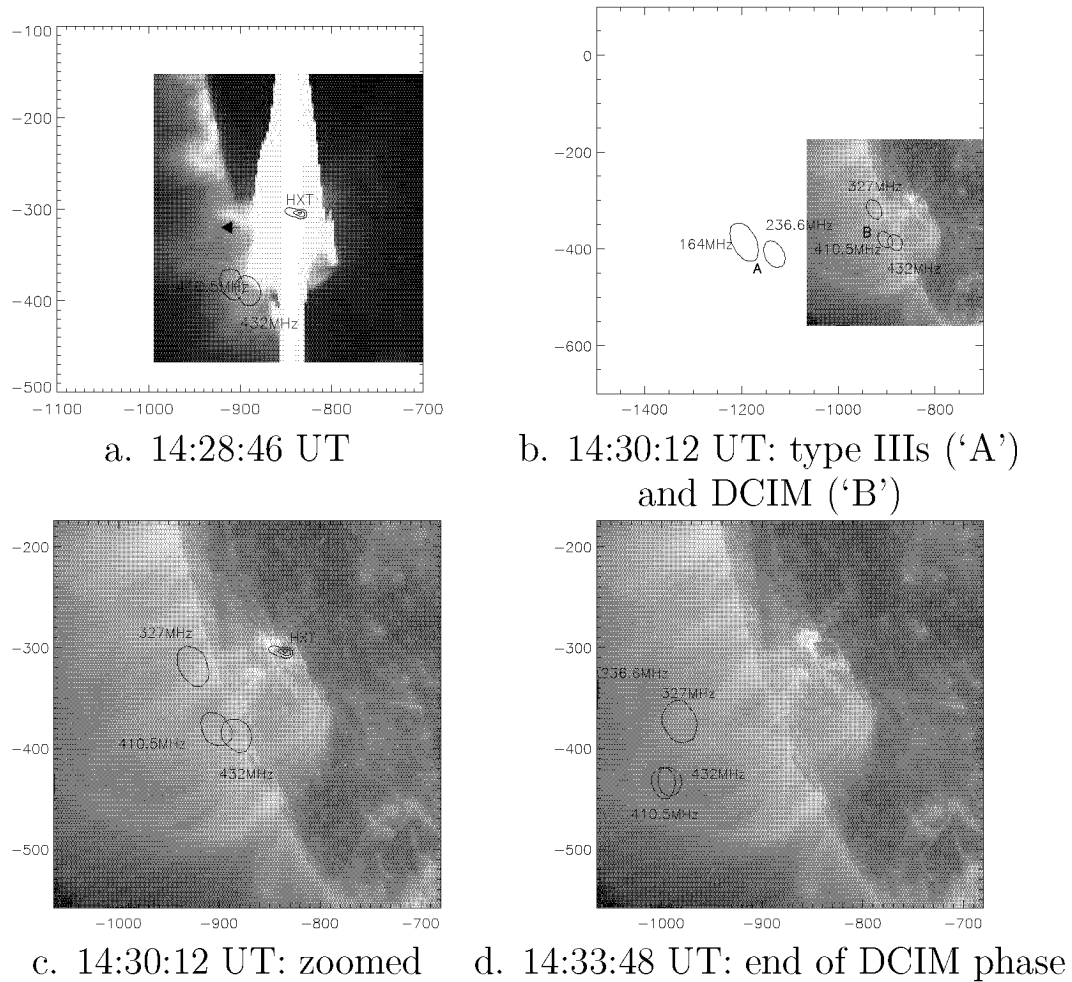
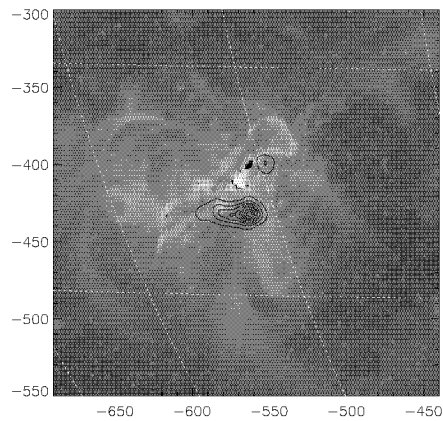
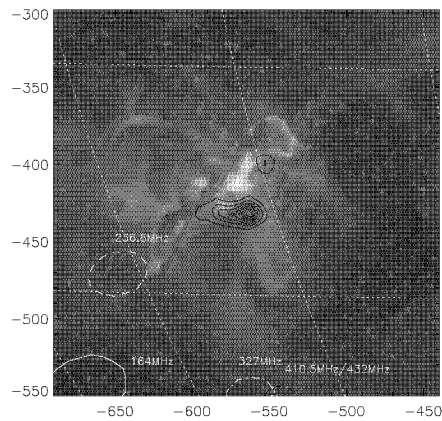


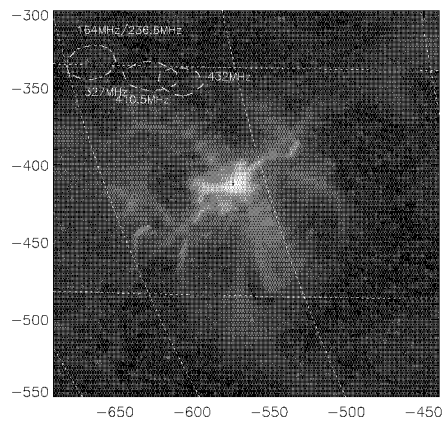
Figure 2.2: 2000/08/25 Event. SXT AlMg and TRACE images with NRH and HXT (from 14:27:30) overlays. The SXT AlMg image (with some saturated pixels) shows an ejected plasmoid (arrow).



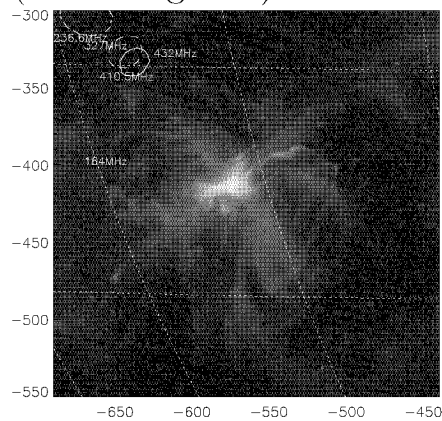
a. 10:06:54 UT: first HXR phase



b. 10:07:21 UT: type II phase ('A' in Fig. 2.6)



c. 10:09:23 UT: DCIM phase (start) ('C' in Fig. 2.6) and type IIIs ('B' in Fig. 2.6)



d. 10:12:24 UT: DCIM phase (peak time) ('C' in Fig. 2.6)

Figure 2.3: 2001/06/15 event: TRACE images with NRH (98% level) contours at various frequencies, and HXT (10:21 UT) overlay.

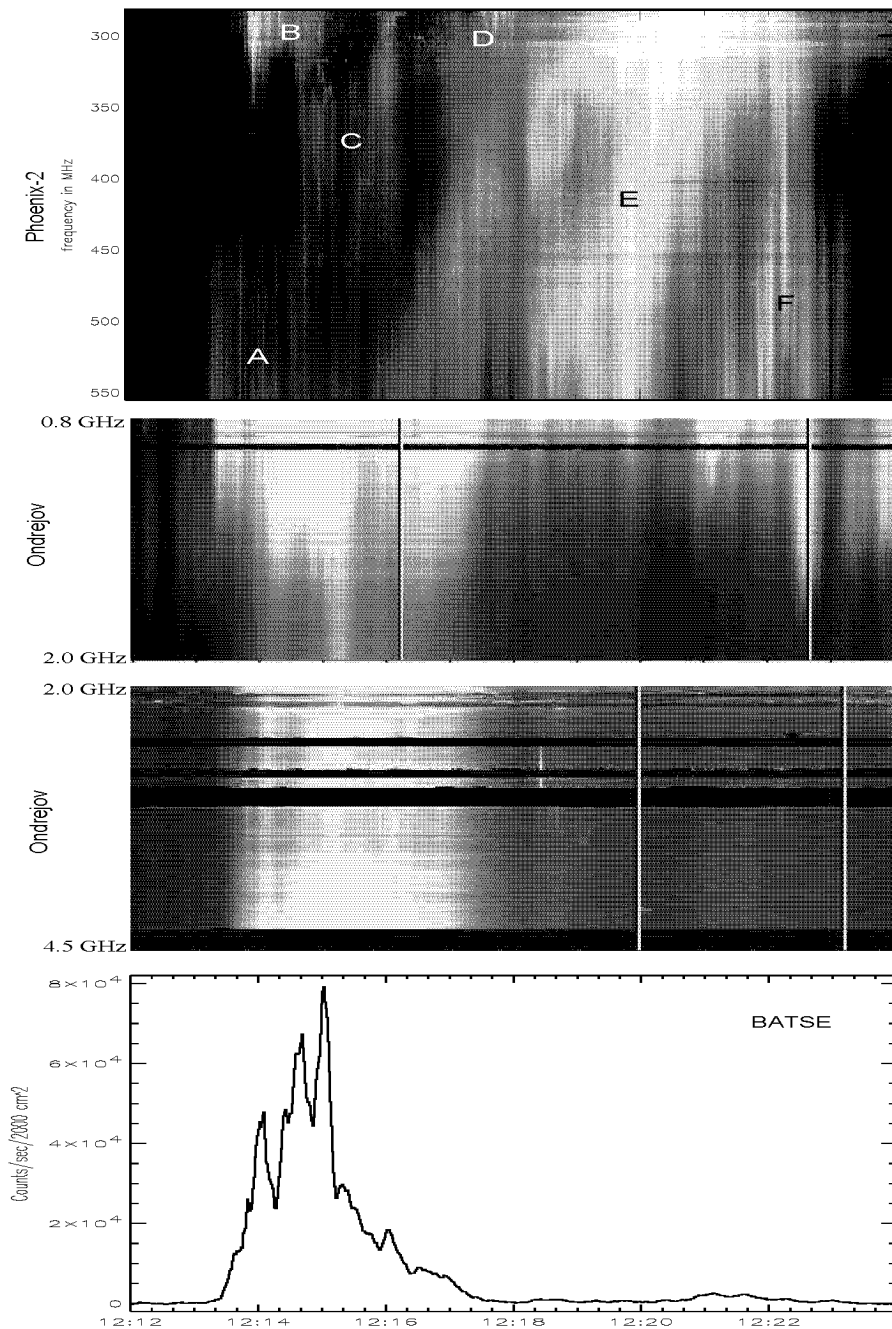


Figure 2.4: Time profiles for the 1999/09/08 event. The position of the emissions marked with letters is shown in Fig. 1 a-d. ‘B’ and ‘D’ are type III burts, whereas the others are DPS.

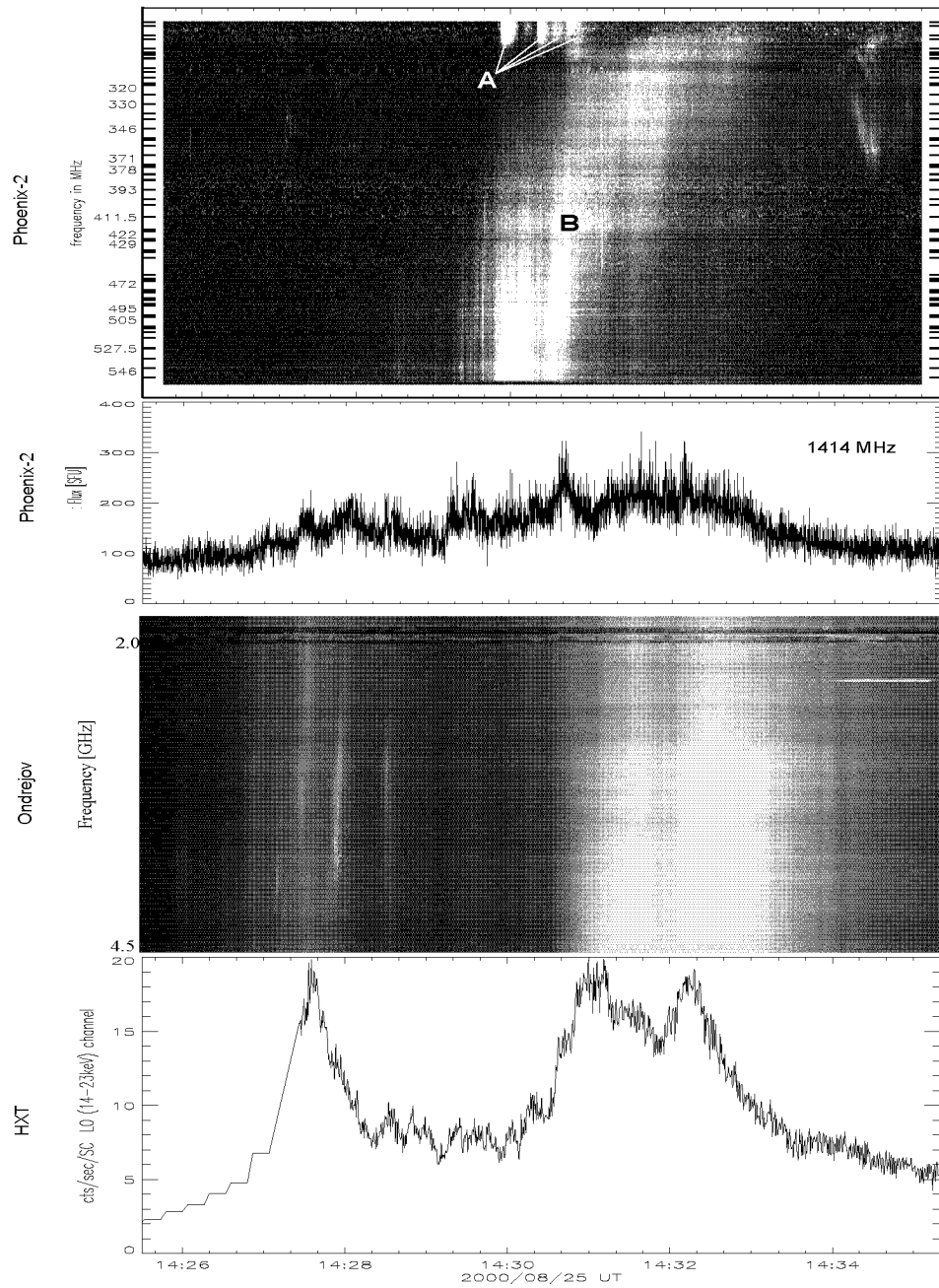


Figure 2.5: Time profiles for the 2000/08/25 event. The positions of the emissions 'A' and 'B' are shown in Fig. 2.2b. 'A' are metric type III bursts, 'B' is a DPS.

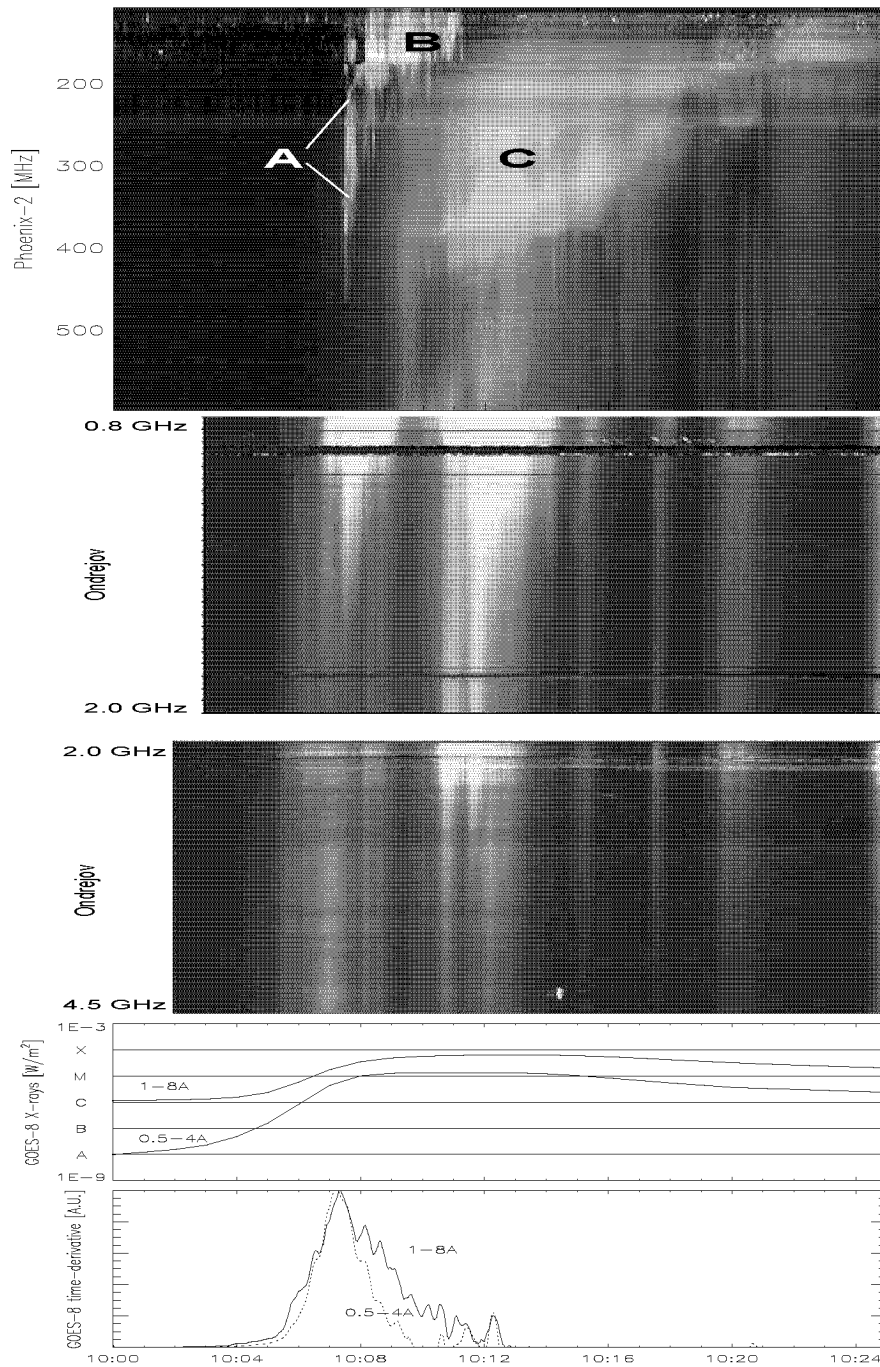


Figure 2.6: Time profiles for the 2001/06/15 event. ‘A’ is the “backbone” of the type II burst, ‘B’ is a group of metric type III bursts, and ‘C’ the DPS. Fig. 2.3 describes their location.

2.3.1 HXR/SXR/EUV observations

All three main events displayed an ejection of matter. It is clear from Figs. 2.1 and 2.4 that the observed ejection of matter occurred before any HXR emission. The movie accompanying this volume shows an ejecta lifting at about 12:10 UT, three minutes before the start of any HXR emission, for the 1999/09/08 event. For the 2000/08/25 event, the first available SXT image (14:27:42 UT) already shows an ejecta $\sim 40''$ above the HXR-emitting region (the image of Fig. 2.2a was taken slightly later, but is of better quality). The ejecta velocity was estimated from successive SXT images to be ~ 300 km/s (Table 2.1), placing the start of the ejecta (assuming it originated in the HXR-emitting region) at $\sim 14:26$ UT, just at the beginning of enhanced HXR flux, 1.5 minutes before peak HXR flux (Fig. 2.5). For the 2001/06/15 event, the ejecta was observed to be flung before 10:05 UT, again at the beginning of HXR emission (Figs 2.3 and 2.6), and ~ 2 minutes before the peak of the HXR flux. As a proxy for HXR emission during early phases of HXR emission for the 2001/06/15 event, the time-derivative of GOES-8 SXR lightcurves were used. HXT lightcurves (and images) are available starting at 10:20 UT.

As seen in the HXR time profiles (Figs. 2.4, 2.5, & 2.6), there are several HXR peaks in each event. Ejection of material seem to occur only before or at the beginning of the first HXR peak in all three cases, and no ejecta was witnessed associated with subsequent HXR peaks.

HXR emission seen in our events generally has the double footpoint shape (see Figures 2.1c, 2.2a, and 2.3a). Some events (1999/09/08, 2001/06/15) showed HXR emission of different peaks to occur at the same places, while others (2000/08/25, 2001/06/15) showed slightly displaced (a few $''$) source locations (but with one of the footpoints remaining at the same place during all HXR flux peaks). The apparent HXR source sizes seem to be always close to about $5''$. Since this corresponds to HXT's spatial resolution, it indicates that the sources are not resolved.

For the 1999/09/08 event, comparing SXT difference images and the EUV ejecta (Fig. 2.7a), it is seen that the SXT increasing part (positive, or white, in the difference image) leads the EUV ejecta front by 5 to 10 arcseconds, whereas the SXT decreasing part (negative, or black, in the difference image) superposes well on the EUV ejecta. The isothermal temperature (using the ratio of SXT's AlMg and Al12 filters) and density in different parts of the AR at HXR peak time are shown in Table 2.3. The

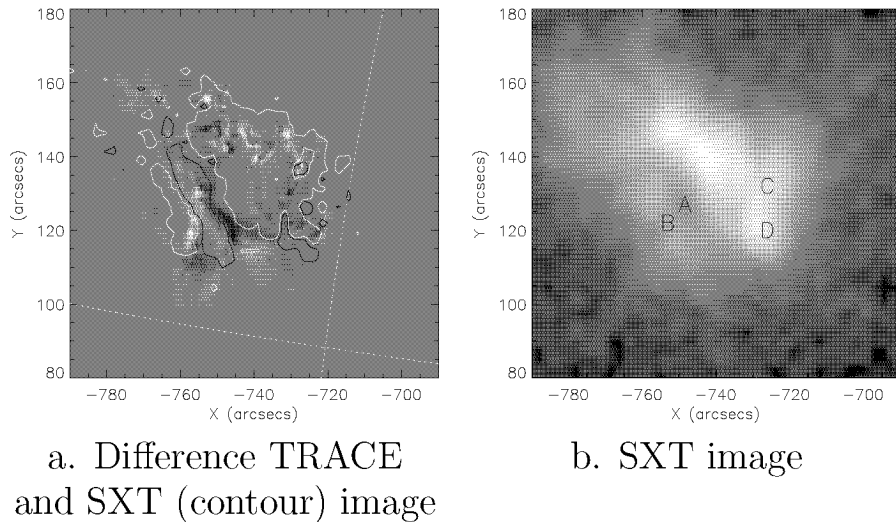


Figure 2.7: (a) TRACE 1600Å difference image (12:13:54 minus 12:13:37 UT), where bright features represent an increase in brightness, and dark ones represent a decrease. Superposed are a set of SXT Al12 difference contours (12:13:59 minus 12:13:45 UT). The white contour shows the +1% level, the black contour the -1% level. (b) SXT Al12 image at 12:13:45 UT. The labels stand for regions where temperature and densities were determined, see text.

Pos.	Description	Te [MK]	Uncertainty factor	Density [cm^{-3}]	Uncertainty	Plasma frequency [GHz]
A	dim cavity between ejecta and AR	13.8	2.3	$2.1 * 10^9$	1.7	0.4115
B	ejecta itself	10.8	1.4	$1.5 * 10^{10}$	1.1	1.1
C	HXR footpoint	9.3	1.1	$8.4 * 10^{10}$	1.03	2.6
D	location of the 327MHz emission	8.7	1.1	$7.9 * 10^{10}$	1.04	2.5

Table 2.3: Temperature and densities of different positions in the AR for the 1999/09/08 event (Fig. 2.7). The real values are expected to lie within the nominal value given, multiplied or divided by the uncertainty factor.

SXT ejecta is remarkably hot and dense whereas the following cavity is even hotter, but an order of magnitude less dense. Apparently coincident with the ejecta is a much cooler plasma emitting C IV (observable with TRACE 1600 Å).

SXR emission measure EM is $\int n^2 A dl$, where A is the pixel area (in cm^2) and we integrate over the line-of-sight length of the column of material. This path length was approximated to be equal to the smallest dimension for features with a clearly dominant dimension (transverse to the line-of-sight) such as a thin loop, or the square root of the feature's area if both length and width were of the same order. The electron density n is assumed constant along the integration path.

Table 2.3 reveals that, of the SXR emitting region, only the cavity ('A' in Table 2.3) between the ejecta and the AR is of low enough density to allow for radio emission as seen by NRH. NRH sees radio emission to the right of this cavity (Fig. 2.1 b and c).

2.3.2 Radio observations

As can be seen from all radio spectrograms (Fig. 2.4, 2.5, and 2.6), metric type III radio bursts occurred shortly (almost immediately for the 1999/09/08 event, after ~ 2 min for the 2000/08/25 event) after the first HXR peak in all of our three main events. Event 2001/06/15 even had a type II burst, indicating a shock wave. In all cases those type III bursts occurred high above the AR, in the general direction where the main ejecta will later be headed. (Figs. 2.1a, 2.2a, 2.3a). The 2000/08/25 event also had a group of type IIIs occurring during the subsequent HXR peaks.

Still in the low frequency range, a few minutes afterwards, there are decimetric pulsations, coming sometimes in patches of varying intensities. These decimetric pulsations (dubbed 'decimetric pulsating structures', or DPS by Khan et al., 2002), actually start with the first HXR peak, as clearly demonstrated by high frequency spectrograms (1 GHz and more), and drift to lower frequencies. The drift rate in the low frequency (220-550 MHz) range is about minus 2 or 3 MHz/s (see Table 2.1). Individual pulses have a 0.5 to 1 second duration, and occur at intervals of 4 to 30 seconds. In the 1999/09/08 and 2001/06/15 events, these DPS seem to stay in the loop structures near the AR (and the HXR footpoints) during the HXR phase. They then slowly drift away from the AR, clearly in a loop-like pattern (see figures 2.1d, 2.3c and d, as well as their related movies). In the 2000/08/25 event, the DPS similarly drifts away from the AR, but also remains close to the main ejecta (the plasmoid - see Khan et al., 2002). This is particularly true for the 327 MHz channel. At the onset of DCIM emission, interestingly, the highest frequency NRH channels (410.5 and 432 MHz, and sometimes also 327 MHz) show sources very close to the AR: a few 10's of arcseconds for the 1999/09/08 and 2001/06/15 events, up to $\sim 100''$ for the 200/08/25 event.

In other events where DPS were witnessed, such as the 2000/08/12 C3.2 flare and the 2000/09/14 C2.1 flare, the DPS also started at the same time as the HXR. In one case, the 2000/09/14 flare, it even started before, and was non-drifting, as are those events studied by Kliem et al.

(2000).

A type II burst also occurred in the 2001/06/15 event. It started before the DCIM, south of the AR (seemingly at a higher altitude), whereas the DCIM occurred north of the AR.

The polarisation of the DCIM pulsations is variable from event to event (observed to be from 0 to about 50%), but remained approximately constant within an event. We also note for the 2001/06/15 event a DPS occurring ~ 0.5 hour after the HXR peak drifted to higher frequencies with a polarization opposite to that of the ‘standard’ DPS feature that occurred shortly after the HXR peak.

2.3.3 LASCO observations:

As a big CME was expelled an hour before the 1999/09/08 12:25 UT flare, which might explain why no CME was witnessed associated with this flare (the first CME was still going on and enhanced density such that the second event might have passed unseen). Starting on 2000/08/25 at 14:54, LASCO observations show a strong CME being expelled, from about the flare site, and with the same direction of travel as the ejecta. Starting on 2001/06/15 at 10:31, LASCO observations show a strong CME being expelled, from about the flare site, and with the same direction of travel as the ejecta.

2.4 Discussion

The fact that ejecta seem to be already on their way when hard X-rays are emitted would support the scenario of a driven magnetic reconnection, where magnetic energy is released rapidly because magnetic structures are pushed together. This is in contrast to the spontaneous reconnection model, where the local Lorentz force is responsible for the reconnection. On the other hand, in other similar events, no ejecta was witnessed. SXT only faintly saw the ejecta in the 1999/09/08 event, whereas TRACE’s 1600 Å filter saw it very clearly. The ejecta (plasmoid) of the 2000/08/25 event was clearly seen by SXT, but only faintly by TRACE’s 171 Å filter. From this, we speculate that ejecta may be often present, but too weak or not seen because at the wrong temperature with respect to the filters at our disposal.

Type IIIs occurring simultaneously with HXR result from accelerated electron beams, propagating along magnetic loops or open field lines that reach interplanetary space. They appear first at a far distance (80" in Fig. 2.1a) from the HXR source. The very weak sources at 410 and 432 MHz are not much further in, suggesting that the acceleration of the type III electrons may be at high altitude.

What causes the DCIM emission? The individual pulsations could be due to electrons trapped at the edges of the ejecta. In a widely accepted scenario, electrons trapped in coronal magnetic loops develop a loss-cone distribution which is unstable and supports plasma emission at the fundamental or harmonic of the local upper-hybrid frequency (Kuijpers & Slottje, 1976).

This is the hypothesis that Khan et al. (2002) defend: the detected radio emission comes from trapped particles in the vicinity of a plasmoid, which would account for the fact that the radio sources move with the plasmoid (or ejecta). It is the case of the 2000/08/25 event, but obviously not of the 1999/09/08 and 2001/06/15 events. In the 2000/08/25 event, the DCIM was clearly seen to follow the ejecta/plasmoid. In the 1999/09/08 and 2001/06/15 events, the DCIM was initially very close to the AR at HXR peak flux time, but then moved further away in a loop-like pattern (that was in the path of the ejecta in the 1999/09/08 event, but on the ejecta's path in the 2001/06/15 event). The discrepancy actually suggests two different situations, although their respective spectrograms are very much alike, and exhibit the same features.

In particular, what causes the pulses seen in all of the events studied in this chapter? NRH measurements show brightness temperatures above 10^{11} K, if one corrects for pulse time vs. integration time. This value might easily be orders of magnitudes higher, since our radio sources seem not to be resolved. This then precludes any non-coherent emission mechanism such as gyrosynchrotron emission (Dulk, 1985). Additionally, a broader-band emission would have been expected from such a mechanism.

As seen in Table 2.1, the individual pulses exhibit very high drift rates, more than 1000 MHz/s. These can generally not come from *broad-band spikes* emitted from one localized source, as the group delay (e.g. Benz, 2002) would lead to negative-only drift rates, and we do observe positive drift rates. Another possibility is the *extended source* scenario (e.g., a magnetic loop with an oscillating diameter), where the source is

modulated simultaneously at all frequencies. The drift rate is then given by the variable source distance from the observer (Aschwanden & Benz, 1986):

$$\frac{\partial\nu}{\partial t} = +\frac{\nu c \cos(\theta)}{2 H_n \cos(\phi)}, \quad (2.1)$$

where θ is the angle between the source's main extension and the radial direction from the Sun, ϕ is the angle between the source's main extension and the observer's line of sight, ν is the center frequency, c the speed of light, and H_n is the density scale height. The drift rates for the 1999/09/08 event would easily fit an extended source with $\theta = 15.1$ degrees and $\phi = 51.8$ degrees. This scenario seems plausible for both the plasmoid (2000/08/25 event) scenario, and for the majority of cases (such as the 1999/09/08 and 2001/06/15 events), where the DCIM seem to originate from a single, loop-like structure. We would expect from such a structure to produce predominantly positive drift rates (which is the case), as high frequencies, being produced further down in the corona, reach us last (on the other hand, Aschwanden & Benz (1986) report also negative drift rates for such structures). We might expect to see another similar 'mirror' footpoint. The fact that this was not witnessed might be due to beaming or refraction effects.

Assuming alternatively that the emission originates from *electron beams* propagating in the corona, the drift rate (treated in a proper relativistic fashion) is given by:

$$\left(\frac{\partial\nu}{\partial t}\right)_{Rel} = -\frac{\nu c\beta \cos(\theta)}{2 H_n (1 - \beta \cos(\phi))} \quad (2.2)$$

where β is the beam velocity (in units of c). It was assumed that the speed of propagation of the radiation is constant throughout the corona, and equal to the speed of light in vacuum (this assumption must be taken, as the group velocity varies along the path of the radiation: from close to zero at $\omega \approx \omega_p$ to almost the speed of light at $\omega \approx 2\omega_p$).

According to Eq. (2.2), no drift rate observed and occurring in the hemisphere nearest us can be higher than $+\frac{c\nu}{2H_n}$, at least for beams propagating at less than $0.7c$. This means that $\frac{\dot{\nu}}{\nu}$ cannot be higher than $+1.5$, assuming a barometric 2 MK atmosphere. The ratio of $\frac{\dot{\nu}}{\nu} \geq +2.33$ observed in Table 2.1 would imply that the radio emission takes place in a

region where the corona is cooler than 1.3 MK. This might be the case sometimes, but is probably not the rule, as we would need for a sizable portion of the corona to have a lower than the usually accepted 1–2 MK temperature, wherever and whenever the DCIM emission occurs!

Another possibility are beams of electrons going through temporary inhomogeneities in the corona. Such inhomogeneities could have scale heights as small as a few tens of kilometers. Taking our drift rate of $\frac{\dot{\nu}}{\nu} = 2.33 = +\frac{V_h}{H}$, and H about 85 km, a value of $V_h \sim 200$ km/s is obtained, a typical ejecta or (slow) solar wind velocity.

Among the proposed emission mechanisms, the beam model in the case of an inhomogeneous corona seems a likely candidate, although the extended source scenario cannot be ruled out.

2.5 Conclusions

To summarize, here are the main points:

- major HXR flares are often associated with ejecta seen in SXR and/or EUV.
- ejecta seem to start before HXR or DCIM emission, suggesting a driven reconnection process.
- DCIM continua occurring nearly simultaneously with the first HXR peak are located close to the HXR source and may be a good indicator of the location of the main acceleration region.
- LASCO: a CME was observed 20 to 30 minutes after the flare in most cases.
- the main DCIM pulsations seem to be emitted by particles possibly trapped in the legs of magnetic loops carried outwards by the ejecta/plasmoid and are apparently not associated with the initial acceleration mechanism responsible for the HXR emission.
- in flares not in our selection, features like ejecta and DCIM pulsations are not always apparent, even during strong flares: possibly due to ejecta temperature and radio propagation in the corona.

- DCIM is apparently not gyromagnetic, nor from broadband emission spike in origin, but could be from extended sources or from type III burst-like emissions occurring in density inhomogeneities.
- metric type III bursts occur within $\sim 1-2$ min after first peak in the HXR flux. Faint decimetric type III bursts were sometimes observed to occur a $\sim 1-4$ minutes before the first HXR peak.
- DCIM observed at high frequencies are generally better related to the HXR timing and located closer to the HXR source. This observation opens the possibility that future observations of DCIM at even higher frequencies (1 - 3 GHz) may find them even nearer and thus closer to the main acceleration region.

Chapter 3

The RHESSI Experimental Data Center

Big things are made out of the sum of many small things.

Common folk saying

ABSTRACT: The RHESSI Experimental Data Center (HEDC) at ETH Zurich aims to facilitate the use of RHESSI data. It explores new ways to speed up browsing and selecting events such as solar flares. HEDC provides pre-processed data for on-line use and allows basic data processing remotely over the Internet. In this chapter, we describe the functionality and contents of HEDC, as well as first experiences by users. HEDC can be accessed at <http://www.hedc.ethz.ch>. Additional graphical material and color pictures are available online¹.

3.1 Introduction

The Reuven Ramaty High Energy Solar Spectroscopic Imager (RHESSI) images the Sun in the 3-17000 keV range (soft and hard X-rays, as well as gamma rays) with unprecedented spatial, temporal and spectral resolutions². RHESSI's main objective is to deepen our understanding of energy release and particle acceleration taking place in solar flares. Furthermore,

¹http://www.astro.phys.ethz.ch/papers/shilaire/HEDC_CDROM_material/

²See Appendix C

it provides spectroscopic information on cosmic gamma-ray bursts, and even image such extra-solar objects as the Crab Nebula (Lin et al., 2002).

RHESSI's nine rotating modulation collimators (RMC) modulate the incoming X-rays on the detectors at the end of each RMC. As each RMC's grid pair has different pitches, a set of nine Fourier-like components are obtained, and are used to reconstruct the original image (Hurford et al., 2002). As each incoming photon is tagged in time, energy and RMC, these photons can be binned in a specified energy band for image reconstructions, lightcurves, and spectra.

A good proportion of existing astrophysical databases concentrate on archiving raw data from one or a few instruments such as Yohkoh, TRACE, RHESSI, or ground-based observatories such as Phoenix-2. Examples are the Solar UK Research Facility (SURF³) and the TRACE Data Center⁴. Other databases offer a selection of data (e.g., synoptic maps) from several observatories and provide usually easier or faster access to these data than the primary archives. Examples are the Base de données Solaire Sol 2000 (BASS2000⁵) (Mendiboure, 1998) and the SOHO Summary⁶ and SOHO Synoptic⁷ search engines.

Most other observatories' data are stored in an immediately usable form, albeit not (fully) calibrated, but suitable for quick perusal. RHESSI data poses the problem that it must be reconstructed to be of any use, much like Hard X-ray Telescope (HXT) data, but on a larger scale.

Image reconstruction can take from less than a minute (for a basic *back projection*) to a several hours (for a tedious *pixion* reconstruction) on a state-of-the-art workstation. Image reconstruction must be done by each data analyst and requires significant hardware and software resources, including the commercial product Interactive Data Language (IDL).

Each flare may require many images, at different times, energy intervals, accumulation time intervals, image sizes and resolution, etc. If we consider the importance of spectra, lightcurves and other ancillary data, we realize that large amounts of computing time are needed to create the derived (i.e. Level-1) data an observer will sift through, to home in on datasets of interest.

³<http://surfwww.mssl.ucl.ac.uk/surf/>

⁴<http://vestige.lmsal.com/TRACE/DataCenter>

⁵http://bass2000.bagn.obs-mip.fr/New2001/Pages/page_acceuil.php3

⁶http://sohowww.nascom.nasa.gov/cgi-bin/summary_query_form

⁷http://sohowww.nascom.nasa.gov/cgi-bin/synop_query_form

These preparatory, but necessary, computational activities partially overlap among each observer and project. This realization provides the starting point for the RHESSI Experimental Data Center (HEDC). Its purpose is to automatically generate an exhaustive amount of ‘quicklook’ data products and assemble them in an on-line data warehouse that will allow fast browsing and other services.

The ‘E’ in the HEDC acronym stands for ‘Experimental’: HEDC introduces several innovations but also serves as a platform for deepening our understanding of scientific data warehouses. HEDC is not simply another data repository, but also a database of scientifically useful derived data. Furthermore, every derived data item is accessible on-line, e.g., through the use of any Web browser.

On-line data processing (on the HEDC’s servers) by users supplements the available data products. Users can add their own data products to the database, and the derived data on events of special interest thus increases in a self-organizing way. User participation will increase the scientific return of HEDC, and ultimately of RHESSI.

HEDC is a joint project of several groups at ETH Zürich: the Institute of Astronomy, the Institute of Information Systems, and the Laboratory for Software Technology (the last two are in the Department of Computer Science).

Section 3.2 describes the HEDC system. Section 3.3 explains how to use HEDC. Section 3.4 summarizes first experiences by users and concludes this chapter. Addendum 3.6 describes the contents of the HEDC Extended Catalog (events and data products). Addendum 3.7 lists of all user-relevant query attributes on HEDC.

3.2 Description of HEDC

HEDC classifies its data as *events* and *data products*. An event (sometimes more specifically referred to as an *HEDC event*) can be a solar flare, a gamma-ray burst, or a terrestrial electron precipitation. The term *other event* is reserved for future extensions or events that are not yet determined. An event consists of a list of attributes (such as start and end times, total counts, peak count rates in certain energy bands, etc.) and a list of associated data products. Data product is the generic term that refers to all derived data: images, lightcurves, spectra, spectrograms, etc.

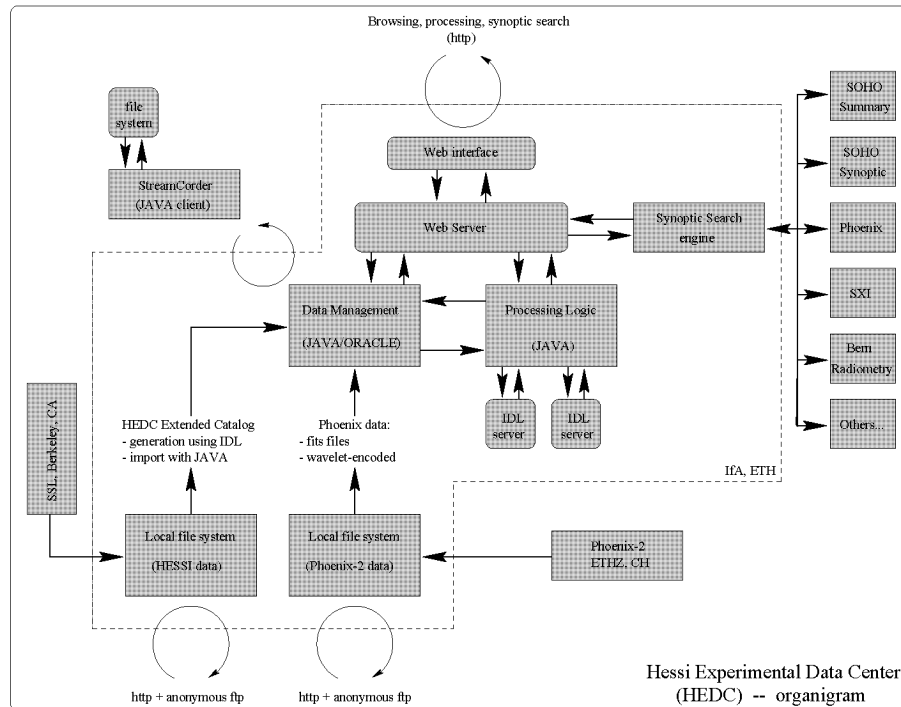


Figure 3.1: The HESSI Experimental Data Center at ETH Zürich

A data product consists of a list of attributes (in this case, the more important parameters that were used to generate the derived data, such as accumulation times, energy bands, etc.) and a picture (PNG or JPEG format). The list of attributes for both events and data products are tables for database querying.

The main services provided by HEDC are:

- On-line database for events and data products;
- On-line RHESSI data processing;
- On-line RHESSI Level-0 data repository that contains the raw data;
- Other on-line services such as a Synoptic Search engine that quickly retrieves other solar quicklook data of relevance.

Figure 3.1 shows an organigram of the different parts of HEDC. Its principal components are:

- A file system for all Level-0 RHESSI and Phoenix-2 (Messmer et al., 1999) calibrated data files;

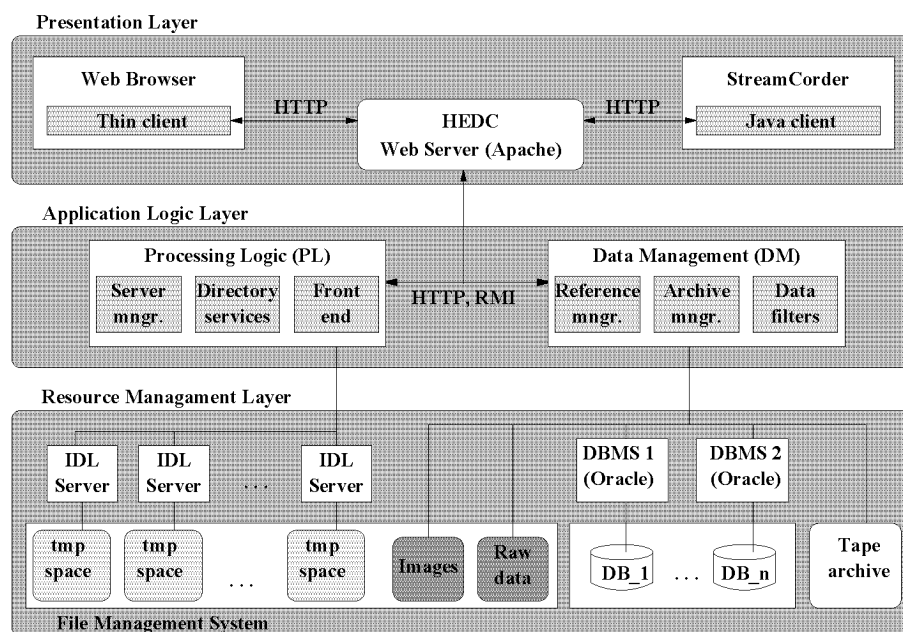


Figure 3.2: Architecture of HEDC

- The HEDC Extended Catalog generation (using IDL) subunit;
- The Data Management (DM) subunit;
- The Processing Logic (PL) subunit and the IDL servers;
- The Synoptic Search engine;
- A Web server providing the main user interface;
- The StreamCorder, an alternative to the Web (browser) interface that provides more flexibility.

3.2.1 Architecture

HEDC is implemented as a 3-layer architecture (Figure 3.2), where the intermediate application logic layer relays requests for data and/or processing by *clients* (programs that run on local workstations) to an Oracle Relational Database Management System (DBMS) and a number of processing *servers* (remote computers at ETH) at the resource management layer. The application logic layer consists of two components: (1) The Data Management (DM) component takes care of all data storage issues.

(2) The Processing Logic (PL) component acts as an intermediary between the DBMS and the IDL servers. Both are implemented in Java and run as stand-alone programs. HEDC can be accessed through either a Web-based client (e.g., a conventional browser)⁸ or a Java-based client, the StreamCorder. With any of the two interfaces, users can query and download raw data, view data products and perform new processing steps. The Java-based client offers some functionality not available in the Web interface, e.g., tools for data visualization and system administration.

HEDC currently runs on a SUN Enterprise Server with 2 GBytes RAM, two 450 MHz processors, two hard-disk drives of 36 GBytes each, and two RAIDs of 654 and 1795 GBytes. Critical data, such as the database configuration information, is stored on RAID with tape backup, as are the derived data and the raw data files. The IDL processing servers execute on the SUN server and on Linux PCs.

3.2.2 On-line RHESSI data repository

RHESSI raw data (the Level-0 data) are stored in the form of FITS files, from which all RHESSI derived data are produced, using the RHESSI data analysis software⁹ (Schwartz et al., 2002).

The raw science data are mirrored daily from the Space Science Laboratory in Berkeley (CA, USA) in their entirety. In keeping with RHESSI's open data policy, all RHESSI data files are publicly available via anonymous FTP¹⁰ or by HTTP access from the HEDC home page. The raw data come in at a rate of about 1.8 GBytes per day, taking about three hours to download. The data are usually available one or two days after observation, slightly more in case of a big flare (because of the limited downlink time between spacecraft and ground stations).

3.2.3 HEDC Extended Catalog generation

Along with the Level-0 data files usually comes 'quicklook' derived data (included are images and a flare list, amongst other items, see the online software documentation for further details). HEDC includes those quick-

⁸<http://www.hedc.ethz.ch/>

⁹<http://www.hessi.ethz.ch/software/>

¹⁰<ftp://hercules.ethz.ch/pub/hessi/data/>

look data products (called here the *standard* catalog) and adds a large amount of other derived data, giving rise to the HEDC *extended* catalog.

The raw data are scanned for events of interest: this is presently done mostly via the flare list incorporated with the quicklook data. Parameters of interest for each event (total counts, peak count rates, etc.) are then extracted and stored in the DBMS as attributes for database queries. A set of data products is then generated for each such event: spectra at different times, images at different times using different energy bands, lightcurves, etc. Whenever possible, additional data relevant to the event are added, e.g., Phoenix-2 radio spectrograms, or the quicklook images or spectra.

Addendum 3.6 gives the current list of the data products computed automatically for each event. All new events and data products are inserted in the HEDC database, and may be recovered by anyone.

The whole process of creating the extended catalog, using IDL and the *SolarSoft*¹¹ (SSW) libraries, and inserting its elements into the database is fully automated, producing a standardized set of data products for each event.

The automatic generation of the extended catalog is still complicated by the changing SSW environment. It has been constantly improved and completed over the course of the mission, and has reached a satisfactory stage. All data since mission start will have been reprocessed by early 2005. Further improvements are still possible.

3.2.4 The data management (dm) component

The Data Management (DM) component handles data requests by external clients and by the processing logic (PL). It offers HTTP and Remote Method Invocation (RMI) interfaces that hide the complexity of the lowest layer and provide an abstraction from the database schema (i.e. the list of database attributes).

Web clients access the DM through the HEDC Web server. Requests are first analyzed to determine the sub-systems needed to create the response. Then the relevant data and data references are retrieved from the database and data repositories, and a dynamic HTML response page

¹¹<http://www.lmsal/solarsoft/>

is generated. StreamCorder clients access the DM directly through RMI, so that no HTML pages need to be created.

In astrophysics, system architectures are typically kept simple to cope with the high amount of data provided. Often, access systems are based on FTP combined with simple query scripts. Within the DM component, HEDC uses a commercial object-relational DBMS to manage the meta-data describing the derived data created by users and automated routines. Using a database simplifies the design of the data center as complex tasks can be left to the database rather than implemented anew. Furthermore, it offers greater flexibility for adding new features as need dictates.

Advantages of using a DBMS rather than a file system include consistent data updates with concurrent users, automatic as well as dynamic creation and maintenance of indexes, flexible query capabilities, efficient in-memory data caching for faster access and query processing, view materialization to avoid repetitive work in answering complex queries, and a flexible framework as the number of users increases and HEDC widens its scope. These are all important features that help HEDC to provide much more sophisticated capabilities than file based systems at a lower development and maintenance cost. The database also takes care of efficient disk utilization and reorganization in an automatic manner and without requiring manual intervention. This is an important feature given the amount of data involved and the high update frequency. These and many other advantages have also been observed by other projects that have followed a similar approach (see, for instance, the work related to the Sloan Digital Sky Survey (Szalay et al., 2000, 2002)).

Moreover, the fact that HEDC is built upon a database has allowed us to extend the architecture in several interesting directions that would have been cumbersome to pursue if HEDC would have been based on a file system. For instance, one of the HEDC interfaces, the StreamCorder, is meant to reside in the user's computer. Under the covers, the StreamCorder contains another object-relational DBMS that mirrors the database schema at the server. As the users work and process HEDC data using the StreamCorder, raw data and derived data are cached locally, thereby greatly speeding up overall processing. Users of the StreamCorder can work disconnected from the HEDC server using the data stored locally. They can also update this local data with new data products which will be automatically uploaded into the HEDC server once the user is on-line again. The StreamCorder has been designed so that

users can gradually create their own HEDC data center provided they have the storage space. Everytime a user performs an operation with the StreamCorder (executes a processing, formulates a query), the StreamCorder checks whether the data is available locally. If that is not the case, it retrieves the data from the HEDC server and caches it locally. Over time and without any effort on their part, users will find that most of the data relevant for their work are stored locally in their small version of the HEDC server. This mechanism helps both HEDC, since it reduces the load at the server, and the final users, who get a much faster access to the data relevant to them.

3.2.5 The processing logic (pl) component

The Processing Logic (PL) allows each user to compute data products beyond those that are part of the existing extended catalog provided by HEDC. Currently, three types of processing are supported, corresponding to the three main objects of the RHESSI software: images, lightcurves and spectra. Each processing activity can be configured with a set of basic parameters.

Users access the PL through the Web-based interface. Each user interacts with the system in a personalized session. Processing steps are specified as tasks that are handled by the system in accordance with the availability of computing resources. Processing is done in the background so that users can submit several tasks at once. Each task is an individual batch operation. This design choice has been taken to avoid user-specific resource reservations on the server. This leaves the scheduling of individual tasks unconstrained, leading to improved resource utilization.

Online processing is integrated with the DM in the following two ways: (1) At the user interface, the PL can be easily accessed while browsing so that the standard attributes of a data product from the extended catalog are copied into the *processing submission form* of the PL. (2) Processing results (PNG and FITS format) can be submitted to the DM and stored permanently into the database.

The implementation of the PL is based on an object-oriented software framework. The system has been designed to easily accommodate changes and additions in the supported types of processing activities; the task control and scheduling system is strictly separated from application-

specific issues, such that more than 95% of the code is independent of the three currently implemented processing activity types. The structure of the system is based on service modules that execute independently and allow distributed task execution in a network of workstations. The session and task management overhead is marginal compared to the cost of data transfers and computation.

Duration of individual tasks can vary significantly. We limited the total CPU time per task to 20 minutes and constrained the set of admissible input parameters (i.e., no *pixon* image reconstructions). Those limitations may be alleviated in the future, depending on usage of available computing resources.

3.2.6 Other services

Synoptic Search

The synoptic search subsystem serves to quickly browse through ancillary data related to a particular event in remote astro-archives. The data obtained are usually daily GIF or JPEG images.

The query mechanism resembles a Web-crawler: first, online requests are issued to several remote archives in parallel; then, the results are collected, grouped and displayed to the user.

This service operates largely independent from other subsystems of HEDC. The service is best effort (if a query to a remote archive times out, no results are available). This light-weight approach of rendering synoptic data accessible through HEDC has proved to be practical and robust. In its current configuration, six remote archive sites are searched, including the SOHO summary/synoptic data archive and the RAPP archive at ETH Zurich. Due to its flexible software architecture, additional Internet-archives can be easily integrated.

Data in FITS format are better suited for data analysis, but are not displayed by the usual Web browsers, hence slowing down the search for datasets of interest. The RHESSI Synoptic Data Archive¹² (Schwartz et al., 2002) provides an ample amount of such FITS data from other observatories, concentrated around RHESSI flare times.

¹²<http://orpheus.nascom.nasa.gov/~zarro/synop/>

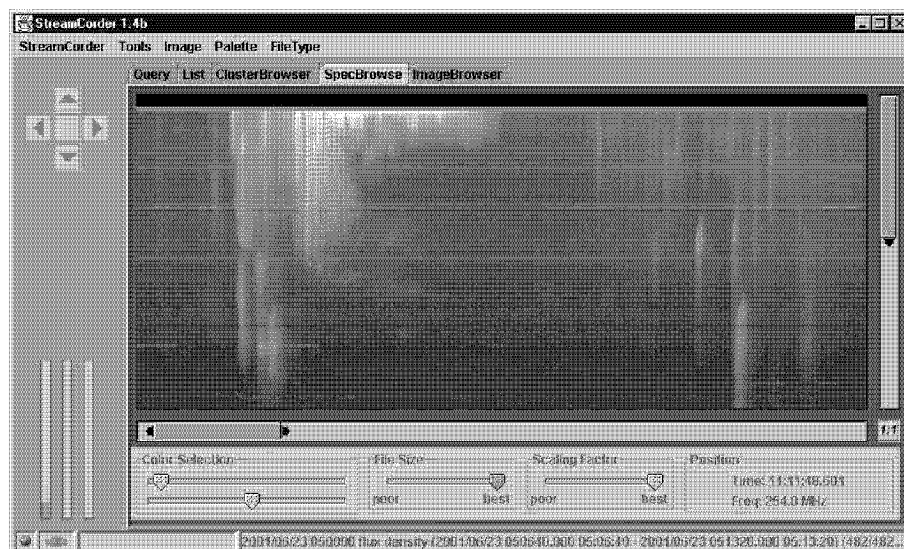


Figure 3.3: The StreamCorder is an alternative to the Web interface. It can search and display all HEDC data products. Here, it is displaying a wavelet-encoded radio spectrogram from Phoenix-2.

The StreamCorder

HEDC is not only accessible through a Web browser, but also through the StreamCorder (see Figure 3.3), which must be installed locally¹³. Except for some performance-sensitive hardware-dependent routines, it has been completely implemented in Java. The architecture is extensible and modules are loaded according to the current data context. Modules may access core services such as stream management, request queues and local analysis programs. Currently available modules support browsing and download of all data types stored in HEDC, allow local and remote processing and offer administrative tools. During RHESSI data processing, the StreamCorder coordinates the asynchronous download, caching, decoding and processing of the data. A local database transparently caches query results and manages downloaded files. The local DBMS schema and the structure of the local file-system archive are identical to the ones on the server. Thus, offline work is possible.

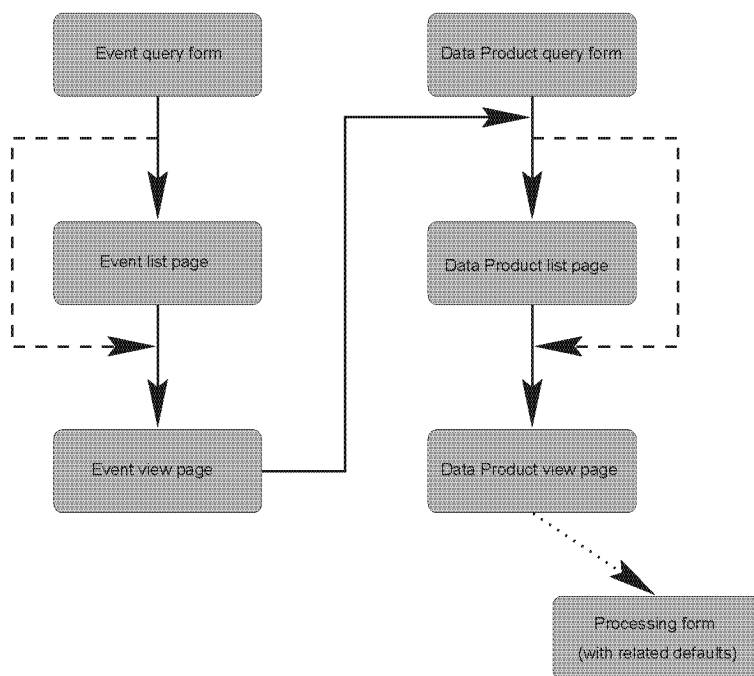


Figure 3.4: Browsing the HEDC using the Web interface. There are two possible entry points: the event query form or the data product query form. After submitting the appropriate query form, a list page containing the result set appears. Clicking on one of its elements leads to the view page, where the full set of database attributes can be examined, as well as a picture in the case of data products. If a query results in a single set, then the list page is bypassed. To the event view page is appended a data product list page, containing the data products associated with that event. The data product view page also has icons to access the processing form: using those instead of directly going to the processing form via the main link on the left of the Web page has the advantage that most of the processing form's attributes are already defaulted to those of the data product just examined.

3.3 Using HEDC

The term *browsing* is used in this chapter to refer to one of these activities: making database queries (either by event or by data products), exploring the result set by going through the links, making another query (perhaps a finer one, or an entirely new one), etc.

The standard workflow model shown in Figure 3.4 for users of HEDC is to browse back and forth for events and/or data products, eventually to make new data products online, and to add them to the HEDC database. Once a user has zeroed in on a dataset of interest, he or she will have to make a thorough scientific analysis on his or her workstation, perhaps downloading some of the images previously made on HEDC. Of course, a user may decide to use only parts of HEDC for browsing, processing, or synoptic searching.

3.3.1 Browsing with the Web interface

The HEDC Web interface currently offers two types of querying: either by event or by data products (Figure 3.4). Both possibilities can be done using either a standard Web form, or a more advanced one.

The *standard* Web form is intended for use by casual users. It is simple and intuitive: there should be no need to consult the on-line documentation. However, only a handful of query fields are available. The *advanced* form should be used by people more familiar with the system, and offers the full range of user-accessible database queries.

Once the query has been submitted, a *list page* appears. There is a current limit of 100 entries on this list. Each entry represents a different event or data product, with a few attributes (time intervals, energy bands, imaging algorithm, etc.) to guide the next choice of the user. Each entry is actually a link to an event (or data product).

Clicking on an event will lead the user to an *event view page*, an HTML page that displays all the event's database attributes (e.g., count rates), as well as a list of all associated data products. A data product view form also lists that data product's attributes (imaging algorithm, etc.), as well as a picture (i.e. 2-D plots or 3-D intensity maps).

¹³<http://www.hedc.ethz.ch/release/>

A comprehensive set of examples are available in the online documentation.

All RHESSI images on HEDC may be downloaded in FITS format (as produced by the RHESSI software *fitswrite* method), by clicking on the appropriate icon in the *data product view page*.

3.3.2 Processing with the Web interface

Whereas browsing is open to the public, an account is needed to perform processings on HEDC (account requests can be made online).

Once a filled processing form is submitted, a *job list* appears. It is a listing of all job requests that were sent with their states (pending, running, finished, failed). Submitted jobs do not share CPU time: rather, each job is queued or executed as fast as possible using one of the available CPUs.

If a job successfully ends, an icon that displays the resulting picture appears in the job list. Clicking on this icon allows the user to view the full picture, as well as to obtain relevant database attributes and other items pertaining to it. One such item is the IDL output, particularly useful in understanding the cause of a failed job. The current setup allows a maximum of 10 jobs at any time per user.

Jobs stay on the job list until the user logs out, up to a maximum of one week. Clicking on the ‘update’ button will update the job list to its latest status.

User events: folders for users’ data products

Once a new data product has been generated and is being viewed by a user, it is possible to store it permanently in the HEDC database. Each user-made data product must be saved in a *user event*, which is just another event on HEDC, and serves as folder (or directory) for users’ data products. In this manner, individual users can create several different folders, one for each of their projects, and put in them whatever data products they process on HEDC. User events do not have any attributes, except for a *code* starting with the username. This means that a query for *events* using time intervals does not reveal user-made events, even if the user-made data products stored inside are within that time interval.

If one is interested in all data products ever generated for a given time interval, one should browse using the *data product query form*. Both user-made and HEDC-made data products are shown (HEDC-made data products have a code similar to their parent event, always starting with ‘HX’).

3.3.3 Synoptic engine

Using the HEDC’s Synoptic Engine is straightforward: a user enters an approximative date and time of interest and submits the request. A list of available links to pictures appears. Choosing a longer time-out than the default value may result in more links found.

3.3.4 The StreamCorder

The StreamCorder provides the user with most of the previously described functionalities but in a more flexible manner than the browser-based interface. As it is a client side application (it runs on a user’s local workstation), it uses local resources for processing, in contrast to the browser-based interface that employs the HEDC server. This offloads work from the server and allows for faster interactions with the system in case of repetitive queries and processings.

The StreamCorder also implements additional features that would be too expensive (in terms of CPU requirements) to provide in a centralized manner. Some examples are (1) a ‘MovieCordlet’ extension allows users to rapidly view a sequence of images made on HEDC, (2) the ‘Spectrum Browser’ enables users to look at wavelet-encoded Phoenix-2 radio spectrograms, allowing for fast exploration of the raw data (Stolte & Alonso, 2002), (3) IDL sessions can be run locally or remotely, (4) a ‘Cluster Browser’ allows users to visualize the density of *event* or *data product* population in a phase space, where a ‘phase’ corresponds to any numerical database attribute (Stolte & Alonso, 2002). The StreamCorder is fully operational, although slight improvements are still being applied to increase ease-of-use.

3.4 First experiences and conclusions

From a user's standpoint, HEDC addresses the major software constraints that create a barrier to starting the analysis of RHESSI data: (1) the purchase, maintenance, and installation of IDL, (2) the installation, configuration, regular update of software unique to RHESSI, (3) the need to learn the detailed use of RHESSI software. Users can easily and quickly examine a huge variety of RHESSI data products, or create their own, with only a Web browser. As a side effect, HEDC is appreciated by those working at home, and who do not have available the necessary software or who lack sufficient transmission bandwidth to download raw data files.

As HEDC uses the SSW/RHESSI software to produce data products, the results are exactly the same as if they were produced from a standard IDL session. Relying on the SSW/RHESSI software makes it easy to compare results obtained at HEDC with other results. Furthermore, the substantial effort in writing (and evolving) this software is not duplicated. Of course, HEDC is therefore tightly coupled to the overall SSW/RHESSI software development and exposes the user to the perils of a dynamic software environment. However, the benefits obtained now (and in the future, after the final release) outweigh any temporary glitches.

Having a database to classify all pertinent RHESSI data products instead of a file system-based archive is a big advantage: a single event can warrant so many data products that users get lost trying to sort them again if they rely on a standard file system. HEDC allows for quick, easy searches.

For the astrophysics researcher, the determination of flare position has been found to be most useful. Many small flares not in the catalog are located by users and stored. Also in high demand are mission-long lightcurves and the visualization of the data in the observing summaries of satellite orbits.

3.5 ADDENDUM: Status as of October 2004

As of October 2004, HEDC has produced data products for over 10000 solar flares. With the increasing number of flares in the database, the

number of users has grown and is still growing. The following statistics was collected from October 19, 2003 to August 17, 2004 (303 days):

1. BROWSING: Altogether 10915 queries were made, or ~ 36 per day, including week-ends. 7699 (70.5%) were made outside ETH.
2. PROCESSING: 284 processing requests were made (~ 0.93 per day, including week-ends). Most from outside ETH.
3. SYNOPTIC engine: 53 requests were made (~ 0.17 per day, including week-ends). Most from outside ETH.

The users include people from all over the World, in particular Japan, USA, UK, Brazil, Germany, and Austria in this order. Browsing is clearly a success when considering the small size of the RHESSI community (~ 100 people). Some of the people using it would never go through the trouble of doing the full data analysis themselves. Others speed up their searches by orders of magnitude.

Processing is not much used in-house and abroad, because serious data analysis requires more tools and flexibility. Nonetheless, it is used by people who miss their pre-selected event in the Extended Catalogue, in particular people (incl. PSI, ISDC (Versoix, GE)) wanting to check for gamma-ray bursts with high time-resolution lightcurves. Synoptic engine was a small addition that did not require too much time or resources to implement. The lack of usage mainly comes from the fact that other similar *integrated* tools exist in the SolarSoftware environment commonly used by the solar community.

3.6 ADDENDUM: HEDC Extended Catalog contents

This addendum describes the current state of what is generated and stored on HEDC. It is liable to change. Consult the on-line documentation for the latest updates. Currently, the generation of the HEDC extended catalog is done about a week after observation by RHESSI. Later reprocessings will occur periodically and incrementally, following improvements or additions to the catalog generator, or major modifications to the raw data or the flare list. The newest, reprocessed versions of HEDC events and

their associated data products will replace previous versions. Of course, user-made events and data products will never be reprocessed.

3.6.1 Detection of events

Currently, only solar flares and some ‘other’ flares (i.e. with parameters still undefined) are being looked for and generated. Later, this might be extended to gamma-ray bursts and electron events.

Solar flares are given by the flare list attached to the Level-0 data. Basically an increase in photon count rates in the 12-25 keV energy band is looked for. The signal must also be strongly modulated in RHESSI’s two coarsest detectors (number 8 and 9). See the RHESSI Data Analysis Software pages¹⁴ for more details on this.

‘Other flares’ are those enhancements in the count rates as seen by HEDC or the flare list, and for which no other classification was (yet) found.

After an event is detected, and its type determined, a set of attributes is determined which characterize the event for later database queries.

3.6.2 Determination of event attributes

Attributes for each events (such as start and end times, total counts, peak count rates in certain energy bands, SAA and eclipse flags, etc.) are determined as each event is generated. Those attributes can be used as search fields during database queries.

Addendum 3.7 gives a full listing of HEDC event attributes.

3.6.3 Data Products automatically generated with each event

For all events:

- overviews made from Observing Summary (McTiernan, 2002) data: count rates in different energy bands; RHESSI trajectory on a Mercator projection of Earth; modulation variance lightcurves; flags; geomagnetic latitude (Figure 3.5, 3.6 and 3.7).

¹⁴<http://www.hessi.ethz.ch/software/>

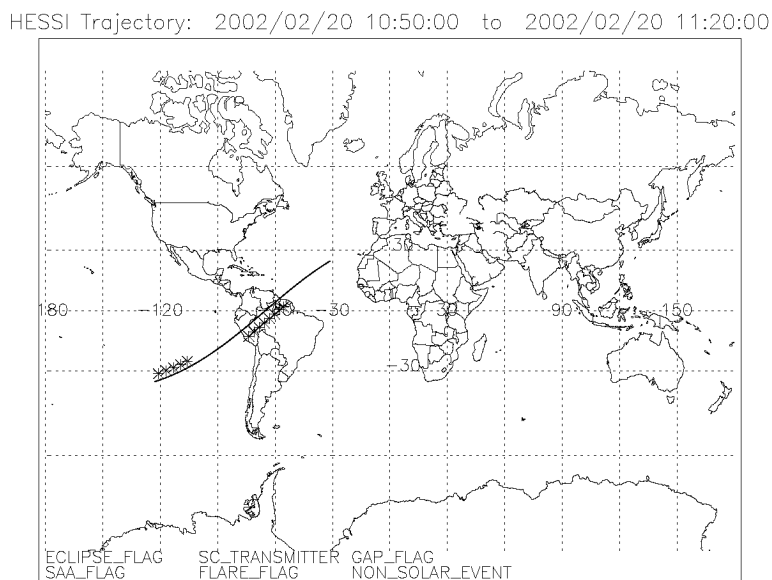


Figure 3.5: For each event, HEDC has a projection of RHESSI's subpoint on a mercatorian view of the Earth. A list of Observing Summary flags is shown at the bottom of the plot. Those are the flags that are being checked for and displayed with stars along the trajectory. This normally color-coded map is available at the web site indicated at the beginning of this chapter.

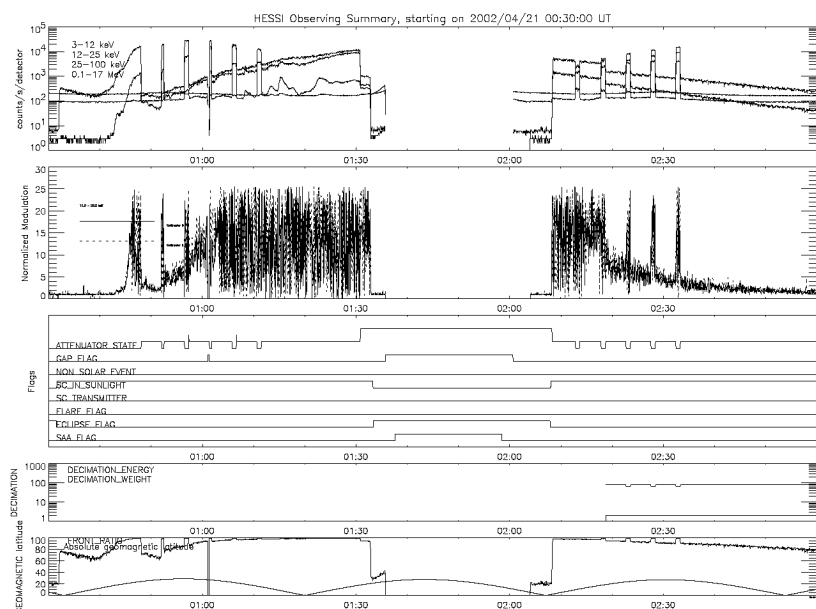


Figure 3.6: For each event, HEDC has an 'Observing Summary page', showing several products available in the Observing Summary, as well as RHESSI's geomagnetic latitude. The usual color-coded version is available at the web site indicated at the beginning of this chapter.

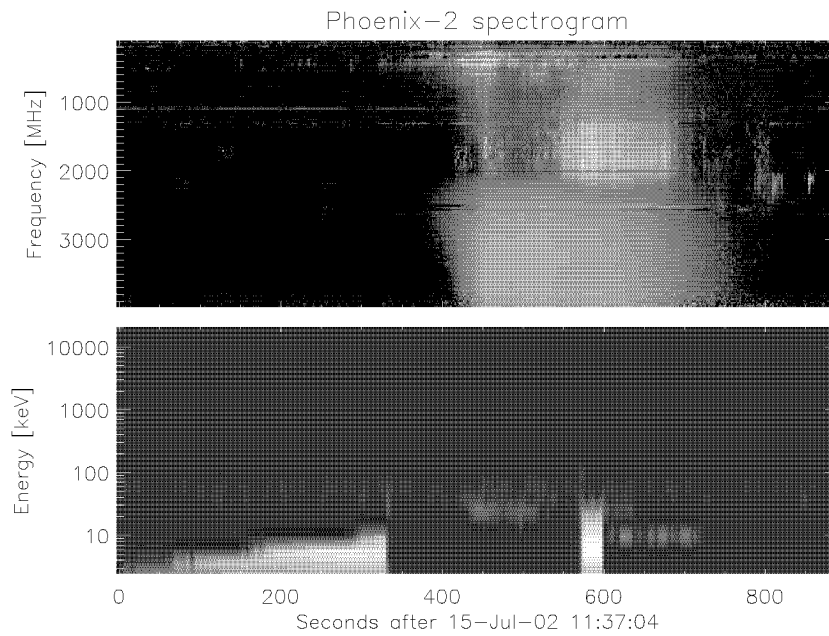


Figure 3.8: For each event, HEDC has a background-subtracted spectrogram from both RHESSI and Phoenix-2 radio data.

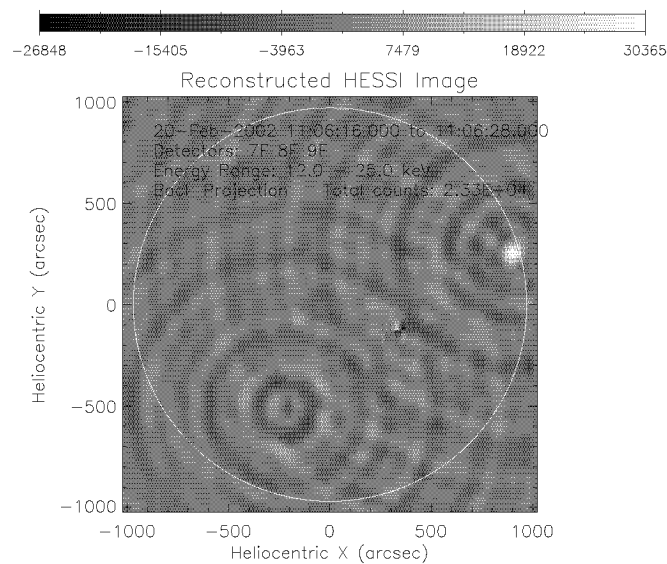


Figure 3.9: For each event, HEDC has a full-Sun back-projected image, at the peak of the 12-25 keV flux. Note flare position (850,280), spin axis (350,-150) and ghost image (-220,-520).

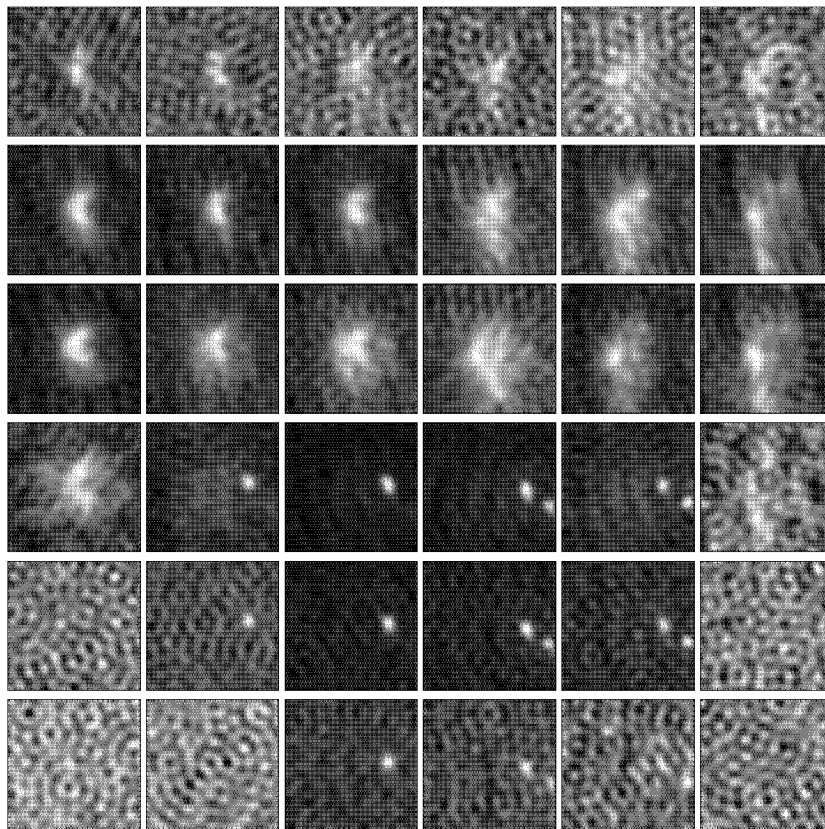


Figure 3.10: For each event, HEDC has a panel of CLEANed images showing the evolution of the flare in time (horizontal) and energy (vertical). Rows, from first to last, correspond to the following energy bands: 3–6, 6–12, 12–25, 25–50, 50–100, and 100–300 keV. Columns, from first to last, correspond to the following times 2003/10/24 02:40:22, 02:44:22, 02:45:22, 02:51:22, 02:57:22, and 03:02:22 (1-minute accumulations).

- RHESSI spectrograms are generated. If possible, they are also superimposed with radio spectrograms from Phoenix-2 (Figure 3.8). Both are background-subtracted.

Additionally, for ‘solar flare’ events only:

- full-Sun image (Figure 3.9), using back-projection.
- movies, i.e. series of images in the following energy bands: 3-12, 25-50, 50-100 and 100-300 keV.
- panel of images in time and in energy, showing the spatial, and temporal evolution of flares in different energy bands (Fig. 3.10).
- Imaging spectroscopy panel, where thermal and non-thermal spectra are fitted to different sources.
- Movies from EUV images from either SOHO EIT or TRACE, with RHESSI contours.

Addendum 3.7 gives a full listing of data product database attributes. The time taken to generate a single ‘solar flare’ event and its associated data products is less than one hour for the above list of data products. More images per event will certainly be generated later on, increasing the processing time accordingly.

3.6.4 Others

RHESSI mission-long daily lightcurves in different energy bands are available through the home page.

3.7 ADDENDUM: Attributes used for browsing queries

Tables 3.1 and 3.2 are lists of the attributes that may be used by users to query for data on the HEDC using the Web interface’s ‘expert’ query form. The on-line documentation provides an up-to-date listing, as well as additional details.

Code	The 'name' of an event. Typically 'HXS202261026', where HX is an event made by HEDC, 'S' for solar flare, and '202261026' for the peak time of the February 26th, 2002 10:26 flare). Another possible format is 'hadar', 'hadar001', etc. for an event generated by user 'hadar'.
Event ID	An internal, unique ID number for each event.
Event type	'S' for solar flares, 'G' for gamma-ray bursts, 'E' for electron events, 'O' for other flares.
Flarelist	Time-concurrent flare list number for a solar flare.
Minimum energy	Lower edge of highest energy band where flare counts were seen.
Maximum energy	Upper edge of highest energy band where flare counts were seen.
Total counts	Total counts of the flare, in the 12-25 keV energy band.
Distance to sun	Solar flare's offset from Sun center, in arcseconds.
X pos	Solar flare's West-East offset on the Sun, in arcseconds.
Y pos	Solar flare's North-South offset on the Sun, in arcseconds.
Creation date	Creation date of the event.
Start DATE+TIME	Date and time of the start of the flare, 12-25 keV band.
End DATE+TIME	Date and time of the end of the flare, 12-25 keV band.
Start time-of-day	Time, in seconds since midnight, of the start of the flare.
End time-of-day	Time, in seconds since midnight, of the end of the flare.
Duration	Time between flare's start and flare's end, in seconds.
Peak D+T (3-12keV)	Date and time of the peak of the flare, 3-12 keV band.
Peak t-o-d (3-12keV)	Peak time, in seconds since midnight, 3-12 keV band.
Total counts (3-12keV)	Total counts of the flare, in the 3-12 keV band.
Peak rate (3-12keV)	Count rate at peak time, in the 3-12 keV band.
Peak D+T (12-25keV)	Date and time of the peak of the flare, 12-25 keV band.
Peak t-o-d (12-25keV)	Peak time, in seconds since midnight, 12-25 keV band.
Total counts (12-25keV)	Total counts of the flare, 12-25 keV band.
Peak rate (12-25keV)	Count rate at peak time, 12-25 keV band.
Peak D+T (25-100keV)	Date and time of the peak of the flare, 25-100 keV band.
Peak t-o-d (25-100keV)	Peak time, in seconds since midnight, 25-100 keV band.
Total counts (25-100keV)	Total counts of the flare, 25-100 keV band.
Peak rate (25-100keV)	Count rate at peak time, in the 25-100 keV band.
Ratio 25-50/12-25	Ratio of counts in the 25-50 keV and 12-25 bands at peak time.
Source multiplicity	Number of sources in a solar flare. Not operational yet.
Active region	Where the flare occurred, as given by the flare list.
Is simulated data	0/1 or NO/YES flag.
S/C in SAA flag	0/1 or NO/YES flag. S/C stands for spacecraft (i.e. RHESSI).
S/C in night flag	0/1 or NO/YES flag. S/C stands for spacecraft (i.e. RHESSI).
Background rate	Background count rate. Not operational yet.
Comments	Added automatically by HEDC, or by a user for a user-made event.
Reserves:	
-S20_HLE_RESERVE1	is simulated set ?
-S20_HLE_RESERVE2	GOES class
-I10_HLE_RESERVE1	Flarelist number
-F10_HLE_RESERVE1	GOES max flux ($\mu\text{W}/\text{m}^2$)

Table 3.1: List of query fields for HEDC events

Code	The 'name' of a data product. For a data product associated with an HEDC-made event, the data product's code is usually the same as the HEDC event's (e.g., HXS202261026). For user-made data products, any combination of 12 characters is possible.
Product ID	An internal, unique ID number for each data product stored on HEDC.
Product type	'IM' for images, 'SP' for spectra, etc. See the online documentation for a complete listing.
Imaging algr	'BACK' for back projection, etc. See the online documentation for a complete listing.
Movie code	Most of the RHESSI images made on HEDC are meant to be viewed in sequence, i.e. they share energy bands, imagingalgorithm, etc., and differ only by their time ranges. All those images have the same movie code.
Movie frame	The order in which an image which is part of a movie appears.
Creation date	Creation date of the data product.
Start DATE+TIME	Date and time of the start of the accumulation time.
End DATE+TIME	Date and time of the end of the accumulation time.
Start time-of-day	Time, in seconds since midnight, of the start of the accumulation time for the data product.
End time-of-day	Time, in seconds since midnight, of the end of the accumulation time for the data product.
Duration	Accumulation time for the data product.
Min energy	Lower edge of the energy bands used for the data product.
Max energy	Upper edge of energy bands used for the data product.
Time resolution	Time binning for lightcurves (corresponds to LTC_TIME_RES).
Front segments used?	0/1 or NO/YES flag.
Rear segments used?	0/1 or NO/YES flag.
Subcollimator used	example: 101111100.
Distance to sun center	Angular offset (in arcseconds) of the center of an image with respect to Suncenter (image data products only).
Xpos	Angular x-offset from Suncenter of the center of an image.
Ypos	Angular y-offset from Suncenter of the center of an image.
Xdimension	Number of horizontal pixels in an image (images only).
Ydimension	number of vertical pixels in an image (images only).
Xpixel size	Horizontal size (in arcseconds) of a pixel (image data products only).
Ypixel size	Vertical size (in arcseconds) of a pixel (image data products only).
Data quality	Unused yet.
Is simulated data	0/1 or NO/YES flag.
Is background-subtracted	0/1 or NO/YES flag. Not used yet.
Other alg. params	Information on some other parameters of the data product.
Comments	Text added by HEDC or by users, for their own data products.
Reserves	Unused yet.

Table 3.2: List of query fields for data products

Chapter 4

Energy budget and imaging spectroscopy of a compact flare

Politics is for the moment, while an equation is for Eternity.

Albert Einstein, on refusing the presidency of the new state of Israel in 1952

ABSTRACT: The energy budget of a compact flare that occurred on 2002/02/26 at 10:26 UT, seen by both RHESSI and TRACE is presented in this chapter. The size of the nearly circular hard X-ray source is determined to be $5.6(\pm 0.8)''$, using different methods. The power-law distribution of non-thermal photons is observed to soften with increasing distance from the flare kernel. The energy of the precipitating flare electron population amounts to $1.7(\pm 0.2) \times 10^{29}$ erg above a 40 keV cutoff energy, assuming thick-target emission. The thermal energy content of the soft X-ray source (isothermal temperature of $20.8(\pm 0.9)$ MK) and its radiated power were derived from the thermal emission at low energies. TRACE has observed a low-temperature ejection in the form of a constricted bubble, which is interpreted as a reconnection jet. Its initial energy of motion is estimated. Using data from both satellites, an energy budget for this flare is derived. The kinetic energy of the jet bulk motion and the thermal and radiated energies of the flare kernel were more than an order of magnitude smaller than the derived electron beam energy.

A movie is available online¹. The kinetic energy of accelerated electrons (cf. Table 4.2) differs from the published paper version of this chapter. Appropriate corrections were deemed necessary after extensive study of the low-energy cutoff problem (cf. Chap. 5).

4.1 Introduction

The energy of solar flares is commonly assumed to be magnetic in origin, but its release is still unclear. MHD theory of reconnection predicts equal shares of energy for local heating by electric resistivity and the motion of the plasma ejected from the reconnection region (e.g. Priest and Forbes, 2002). However, early observations of centimeter radio and hard X-rays (HXR) from flares made clear that a considerable fraction of the flare energy is initially transferred into energetic electrons (Neupert, 1968; Brown, 1971; Lin and Hudson, 1976) and possibly ions (Ramaty *et al.*, 1995). These "non-thermal" particles carry a large fraction of the energy away from the flare region and deposit it partially in the chromosphere, where plasma is heated to tens of million degrees, rises into the corona and emits soft X-ray emission (Neupert, 1968). The knowledge of the energy content in the various forms of primary and secondary energy is essential in formulating flare scenarios and modeling flares.

The partitioning of the energy is not well known, as the exact evaluation of the various amounts of energy is hampered by observational limits. Early estimates by Strong *et al.* (1984) of a simple flare using several instruments on SMM find a ratio of 1.3:1.7:1 for the distribution between electron beam, mass motion, and thermal energies, where the mass motions were measured in a Ca XIX line and may include also evaporative motions. It may be partially a secondary form of energy, derived from the kinetic energy of energetic particles. de Jager *et al.* (1989) have compared beam and thermal energies of 19 flares with similar results. Observations indicative of reconnection jets have been reported in the literature (e.g. Shibata *et al.*, 1994; Pohjolainen *et al.*, 2001; Zhang, Wang, and Liu, 2000). The identification as a reconnection jet in the corona was often based on the motion of dense material. As the process of reconnection is not predicted to substantially increase the density, these observations suggest that reconnection took place in a high-density region. This may

¹http://www.astro.phys.ethz.ch/papers/shilaire/Ebudget_ImSpec_CDRom_material/

not necessarily be the case in all flares. The heating of reconnection jets is not understood. Although the plasma heated by resistivity is ejected, the jets also contain plasma at preflare temperature in the MHD scenario. Innes *et al.* (1997) have reported reconnection jets in the quiet Sun having a temperature of a few 10^5K . On the other hand, stochastic electron acceleration by transit-time-damping of low-frequency waves is currently the most preferred mechanism (Miller *et al.*, 1997). It is expected to take place preferentially in the turbulent plasma of reconnection jets and may also heat them.

With the new generation of solar instruments in EUV lines, soft and hard X-rays, a more accurate determination of energies becomes feasible. Of particular relevance is the Reuven Ramaty High Energy Solar Spectroscopic Imager (RHESSI) launched on February 5, 2002 (Lin *et al.*, 2002). RHESSI's germanium detectors, flown in space for the first time, register photons in the energy range from 3 keV to 17 MeV with 1 keV resolution at low energies (Smith, 2002). For the first time it is possible to explore the low-energy limit of non-thermal electrons, where most of the beam's energy resides. Nine absorbing grids modulating by satellite rotation provide the basis for imaging. The new method allows reconstructing the image of a flare anywhere on the visible disc of the Sun with a resolution of about $2''$ at low energies (Hurford *et al.*, 2002). Thus, RHESSI's spatial resolution also allows determining the size of the high-temperature thermal flare plasma, necessary to estimate its energy content. Furthermore, RHESSI can model the thermal plasma by fitting the low-energy spectrum and determine its temperature and emission measure. The spatial resolution of an instrument like TRACE (Handy *et al.*, 1999) allows measuring the motion of coronal plasma at relatively low temperature predicted by MHD models for parts of the reconnection jets.

In this chapter, we use the new capabilities for the first time to estimate the various flare energies in a well-observed, simple flare. The observations and some relevant analyses are presented in Sections 2 through 6, and in Section 7 the energies are evaluated and compared. A movie is available on the CD-ROM accompanying this volume.

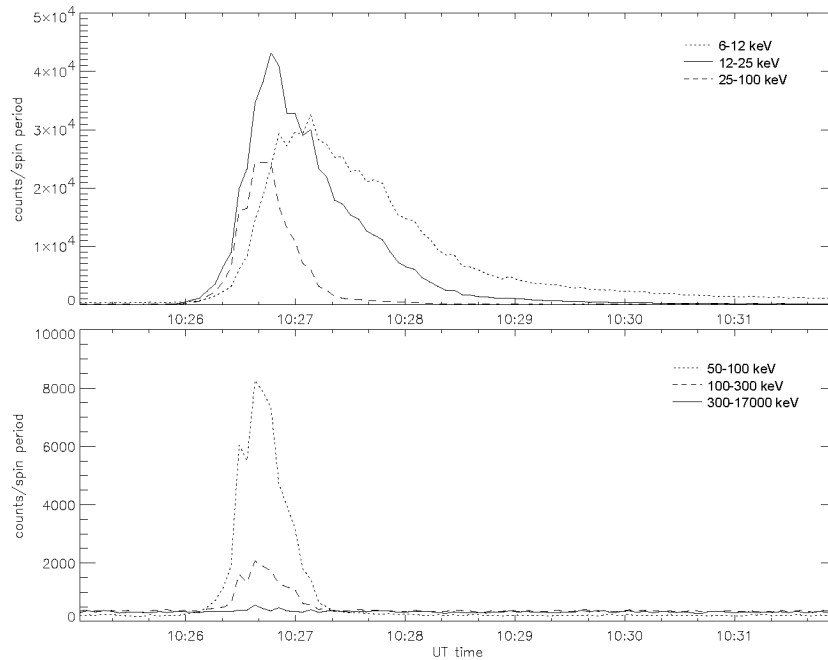


Figure 4.1: Lightcurves of RHESSI observations in uncalibrated counts per 4.35s rotation period. All RHESSI front detector segments were used.

4.2 Lightcurves and other generalities

A flare occurred near the western limb of the Sun on February 26, 2002, and was observed by both RHESSI and TRACE. NOAA/GOES reported it as a C9.7 class flare.

Figure 4.1 shows that this event, while not the most powerful of flares, did have a non-negligible flux of high-energy photons (i.e. higher than 100 keV): enough to allow images to be reconstructed (Fig. 4.3). The Phoenix-2 radio spectrometer (Messmer et al., 1999) saw gyrosynchrotron radiation during the high-energy part of the HXR emission (Fig. 4.2), but very little decimetric emission. It consisted of three reverse drifting type III bursts between 1.2-2.0 GHz and a regular type III burst (620-800 MHz) with possible narrowband spikes at 850 MHz. All these faint coherent emissions (not visible in the overview of Fig. 4.2) occurred after the HXR peak.

RHESSI's attenuator state was '1' (thin in, thick out) at all times. No decimation occurred, RHESSI was 'in the clear' throughout the event (no SAA or eclipse). The flare took place when RHESSI was at high geomagnetic latitude (43 degrees).

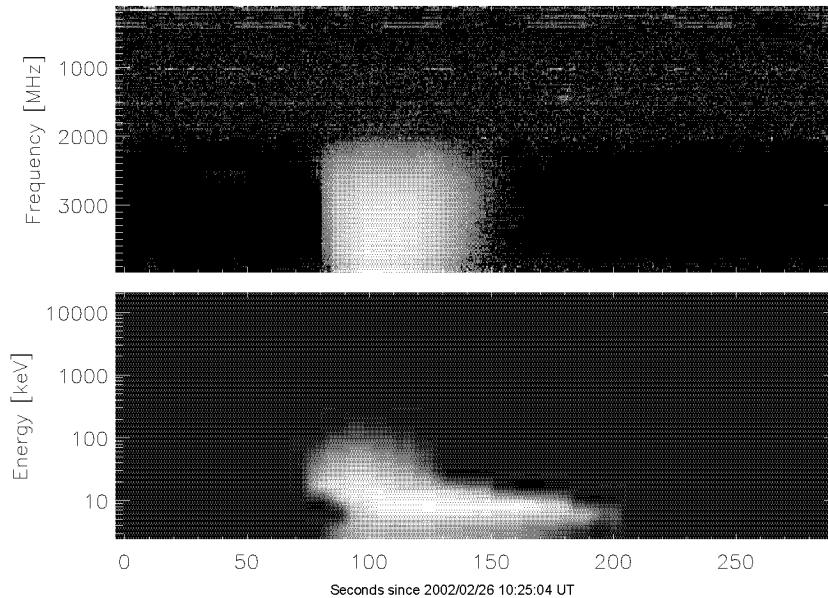


Figure 4.2: Phoenix-2 radio (top) and RHESSI (bottom) spectrograms of the event. Both are background-subtracted.

As the average count rates per detector (total for all energy bands) was less than 6000 counts/s, no pile-up in the detector is expected (Smith et al., 2002). No data gaps were recorded, aside from the fact that detector 2 was turned off at the time of the flare, and the presence of the usual *dropouts*. Dropouts are short data gaps (≤ 1 s) that occur randomly in every RHESSI detector, and are most likely the result of cosmic ray hits that momentarily saturate the detector electronics (Smith et al., 2002) – the imaging reconstruction software deals with those by ignoring them, i.e. during those times, no weighted modulation pattern contribution is added to the back-projected map.

4.3 Source size

Figure 4.3 shows the flare at different times and energies. As the flux diminishes with higher energy, the brightness of the images has been adjusted. It can be seen that its spatial shape is nearly circular and remains practically constant during the HXR emission (special care has been taken to ensure that the *same* aspect solution was used for all the images.). The deviation from circular at 100 – 300 keV is not to be

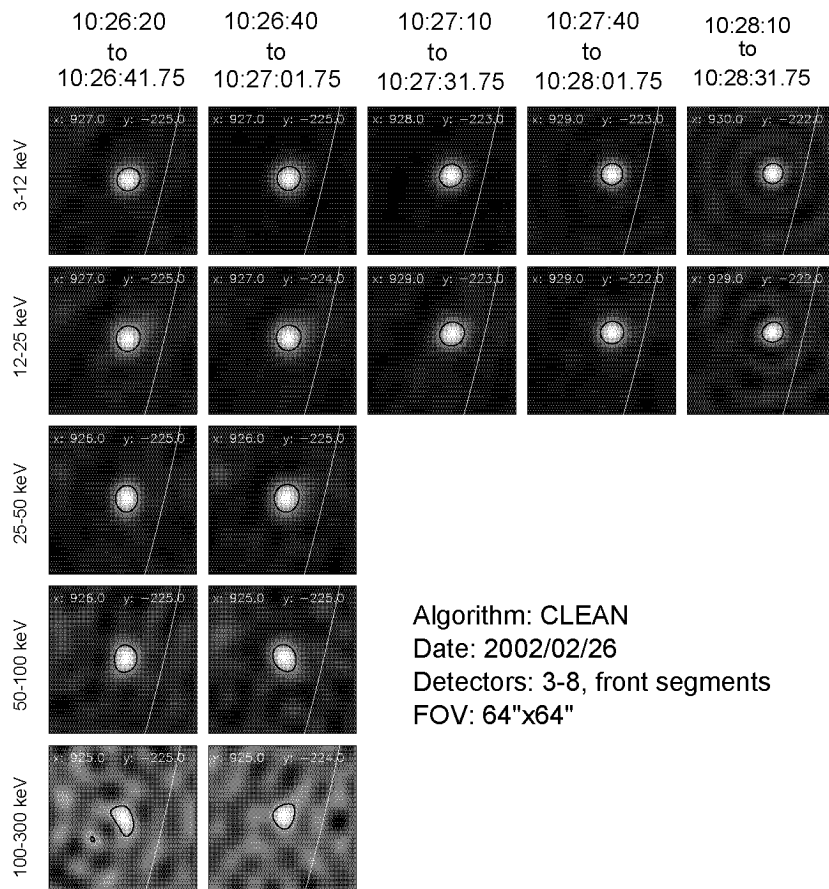


Figure 4.3: Panel of images: time (horizontal) vs. different energy bands (vertical). The black contour show the 50% level of the image. The white line is the photospheric limb of the Sun. The white numbers on each panel refer to the position, in arcseconds from Sun center, of the brightest pixel in the image.

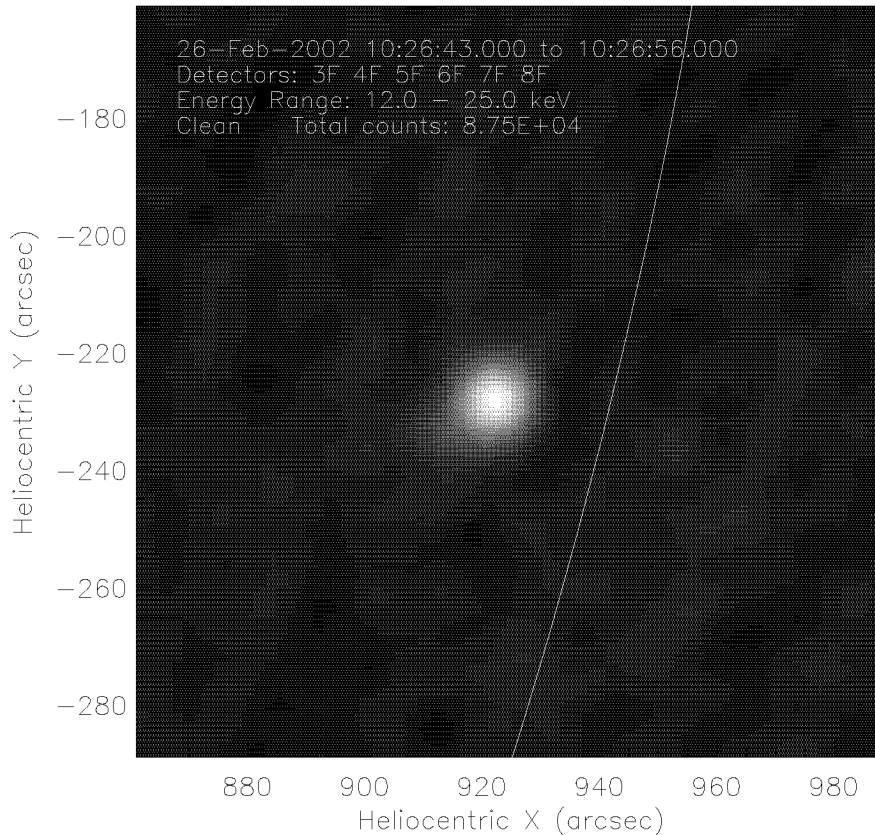


Figure 4.4: RHESSEI CLEANed image made at peak 12-25 keV flux time (10:26:43 to 10:26:56 UT).

considered statistically significant.

Figure 4.4 is a close up of the flare, as seen by RHESSEI. It is the result of careful elimination of unbeneficial collimators and detectors. The first panel of Figure 4.5 shows that subcollimator 1 would not have contributed in a useful manner to the overall image: a pattern of minima and maxima of size and spacing comparable to that subcollimators’s FWHM. Taking a longer accumulation time, i.e. the whole time interval when HXR counts were above background and the source spatially stable (10:26:20 to 10:27:10 UT), does not yield a better result, even though the estimated total number of counts above background (~ 25000) should have been sufficient. We conclude that subcollimator 1 has over-resolved the source. Detector 2 was unfortunately turned off at that time. Detector 9 (FWHM of $186''$) was also removed, as its low resolution does not add any new features to the image. Hence, our imaging capabilities are limited by subcollimator 3, which has a FWHM point spread function of $\sim 6.9''$.

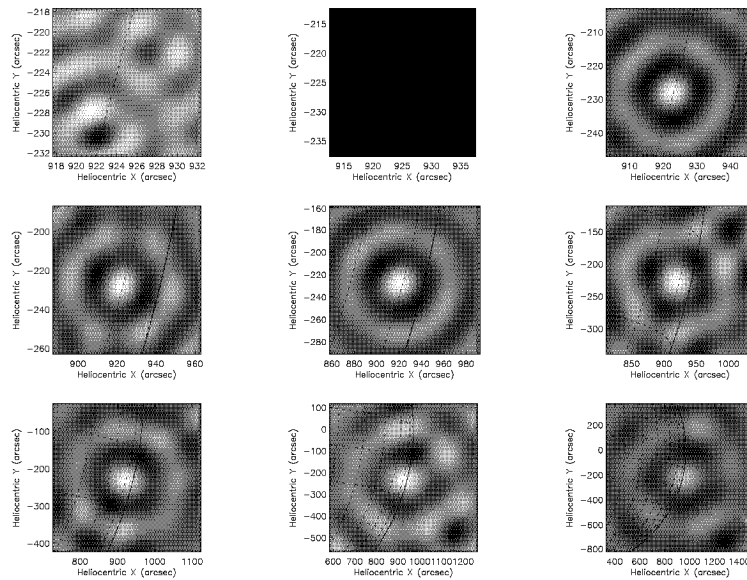


Figure 4.5: Back-projected images for each subcollimator (1 to 9), other parameters are the same as for Figure 4.4. The field of view and the pixel size are adjusted to the resolution of each subcollimator, such that the spatial sampling is twice the resolution.

Table 4.1 lists the results of several methods used to determine the source size. The ‘modulation amplitude’ method will be described in this section, whereas the ‘imaging spectroscopy’ method will be described in section 4. A source imaged with RHESSI appears larger than its true size σ_s , the standard deviation of an equivalent gaussian. The observed source size σ_{obs} results from convolution with the point spread function σ_{psf} of the instrument, where $\sigma_s = \sqrt{\sigma_{\text{obs}}^2 - \sigma_{\text{psf}}^2}$, assuming that both source and point spread function have gaussian shapes.

The FWHM of the source was determined from the 50% contour of its image reconstructed by back projection, CLEAN and Maximum Entropy Method (standard RHESSI software)². The FWHM of the point spread function of RHESSI collimators 3–8 was measured the same way. Back projection and CLEAN yield results that agree within the error bars. The larger result obtained with forward fit might be due to the presence of an important halo for this flare (Schmahl and Hurford, 2002). The very small FWHM obtained by MEM-Sato may be caused by what has been dubbed ‘super-resolution’, and is not to be trusted.

Image reconstructions (with both back projection and CLEAN) using

²<http://hesperia.gsfc.nasa.gov/rhessidatcenter/>

Method	convolved FWHM	deconvolved or true FWHM
FWHM of maps:		
‘back proj.’ using SC 3-8	$10.5 \pm 0.7''$	$5.4 \pm 1.4''$
CLEAN using SC 3-8	$10.6 \pm 0.4''$	$5.6 \pm 0.8''$
MEM Sato, using SC 3-8	$2.9 \pm 0.2''$	-
Forward Fit, using SC 3-8	$17.0''$	-
Pixon, using SC 3-8	$5.9 \pm 0.7''$	-
imaging spectroscopy	$11 \pm 0.5''$	$6.3 \pm 0.9''$
modulation amplitude		$4.7 \pm 1.5''$

Table 4.1: Size of non-thermal HXR source (12–25 keV), derived by different methods. The error of the convolved size from RHESSI maps indicate the total range.

the RHESSI simulation tools has been done for different gaussian source sizes. For a true source size of $\sim 6''$, the apparent source size resulting from the simulated map agrees well with that of the observed map, and is close to the value found in table 4.1. Another method of determining source size was also attempted using *modulation profiles*.

Figure 4.6 displays the modulation profiles that were used to produce Figure 4.4. From those, the *relative modulation amplitudes* (Schmahl and Hurford, 2002) were determined. The relative modulation amplitude A is defined as follows:

$$A = \frac{1}{M} \frac{C_{max} - C_{min}}{C_{max} + C_{min}} = \frac{1}{M} \frac{C_{max} - \langle C \rangle}{\langle C \rangle} \quad (4.1)$$

C_{max} and C_{min} are the maximum and minimum counts per time bin in a modulation cycle. M is the *maximum modulation amplitude*. It is determined by the angle of incidence on the grid as well as the effective slit/pitch ratio. The software calculates it for each time bin. Schmahl and Hurford (2002) give an analytical formula for A in the case of gaussian sources:

$$A = e^{-0.89 \left(\frac{\Delta\theta_s}{\Delta\theta_{coll}} \right)^2}, \quad (4.2)$$

where $\Delta\theta_s$ is the source’s FWHM, and $\Delta\theta_{coll}$ is the collimator’s FWHM. Thus, the modulation disappears gradually as the source dimension exceeds the collimator resolution.

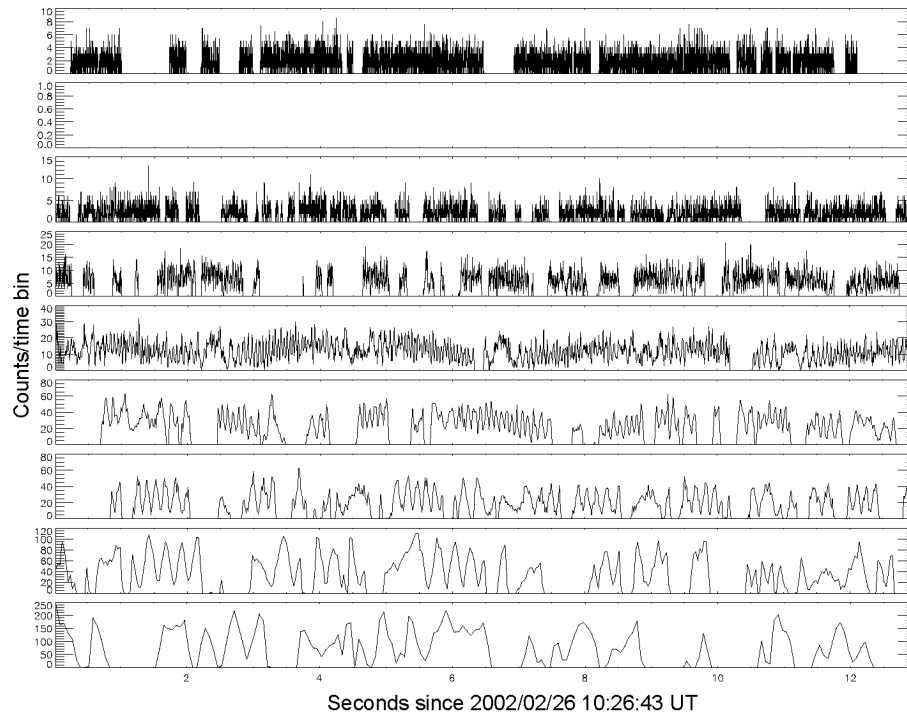


Figure 4.6: Sample of modulation profiles for each subcollimator (1 through 9: from top to bottom) for the time interval used for the image in Figure 4.4.

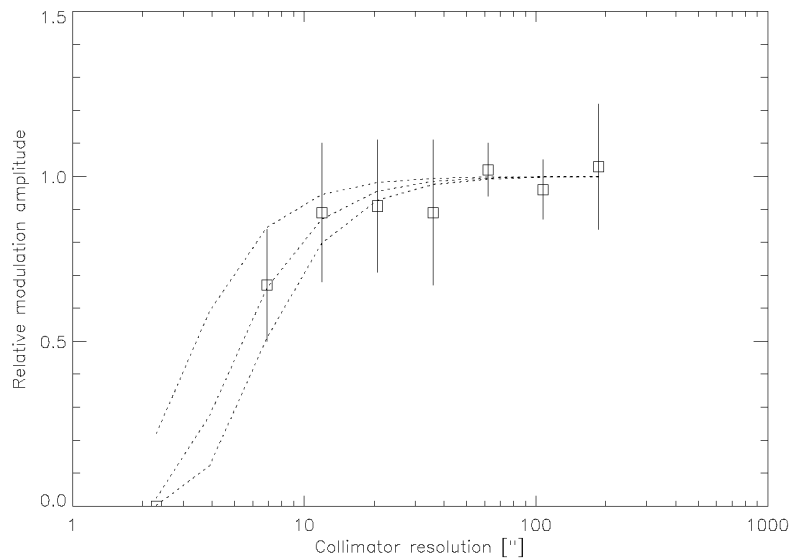


Figure 4.7: Observed relative modulation amplitude vs. subcollimator resolution, from the modulation profiles of Fig. 4.6. The dotted curves were computed using Eq. (4.2). The upper one for a source size of 3" FWHM, the middle one for a size of 4.7" FWHM, and the lower one for a size of 6" FWHM.

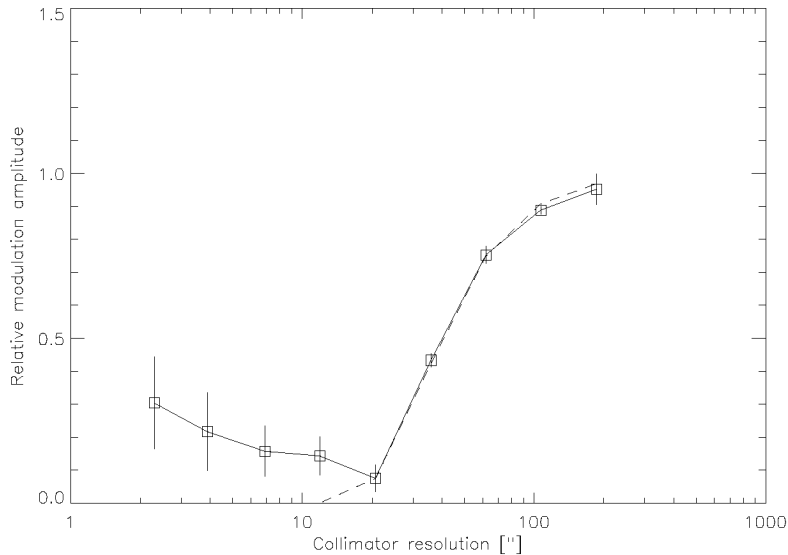


Figure 4.8: Relative modulation amplitude vs. collimator resolution (FWHM), for a simulated 2-D circular gaussian source of size $\sigma=15''$ ($= 35.3''$ FWHM). The solid line links the data points, whereas the dashed line was computed using Eq. (4.2).

C_{max} and C_{min} were determined manually and averaged over several modulation cycles (from 3 for subcollimator 9 to 60 for subcollimator 3, also yielding a standard deviation) in the modulation profiles (Fig. 4.6). Thus, the contaminating effects of dropouts have been removed. The results are displayed in Figure 4.7. The relative modulation amplitude was set to zero for the first (finest) subcollimator, where photon fluctuation was clearly dominant. The relative modulation amplitude of subcollimator 2 was ignored, as it is not available. Few modulation cycles without dropouts were available (Fig. 4.6) for subcollimator 9, resulting in a large standard deviation. Otherwise, the error bars increase with decreasing subcollimator coarseness. This is because the size of the time bins that were used also decreased with decreasing subcollimator coarseness, thus increasing the effects of photon counting noise. Comparing the data points with the theoretical curves, a source size of $4.7 \pm (1.5)''$ is assumed, and will be used in the numerical computations of section 7.

The method was tested on gaussian sources of different sizes using the RHESSI simulation software tools. The match is almost perfect for regions with low photon fluctuations. Figure 4.8 is one such plot, made with 5×10^5 photons/s/detector, for a source size of $35.3''$ FWHM, and in the same 12-25 keV energy band as used previously. The existence of

non-zero relative modulation amplitudes at low collimator resolution is due to photon counting noise, and the manual technique for finding the peaks, which does not make any use of the phase (as a forward fitting method would).

The $4.7(\pm 1.5)''$ source size derived from the modulation amplitude method is consistent with the previous results. As all the deconvolved results are consistent (Table 4.1), and as CLEAN yielded the deconvolved result with the smallest error bar, its value of $5.6(\pm 0.8)''$ will be the source size considered for the remainder of this chapter.

4.4 RHESSI imaging spectroscopy

Imaging spectroscopy is limited by photon-counting noise. Hence, we will simply concentrate on doing imaging spectroscopy during the peak HXR flux of the flare. As the images obtained are not fully calibrated through the spectral response matrix (Schwartz et al., 2002), only energies above 10 keV and below 100 keV were considered.

The flare was imaged (using CLEAN) between 10:26:43 and 10:26:56 UT, from 10 to 100 keV (using 1-keV energy bins from 10 to 20 keV, then 5-keV bands), and using detectors 3, 4, 5, 6, and 8. The image was over-sampled by taking $1''$ pixels. The 26 images thus obtained are not shown here. A ‘crosshair’ of pixels (10 vertically, 10 horizontally), centered on the flare, was considered. Figures 4.9 and 4.10 show results obtained by averaging pixel fluxes at equal distance from the flare’s center.

Figure 4.9 shows that the portion of the spectrum above the thermal bremsstrahlung component is close to a power-law, with photon spectral indices varying from 3.4 ± 0.2 (flare center, associated with the brightest pixel in the map) to 3.9 ± 0.2 (at $10''$ from flare center), with the fits made in the 20-40 keV energy bands.

The hardening of the spectral index towards the center of the flare kernel may be due to a harder electron distribution (more fast electrons) near the center of the flare.

This observation does not support proposed models such as a superposition of thermal distributions (Brown, 1974) mimicking a power-law of energy spectral index, e.g. $\gamma = \frac{1}{2} + \frac{3}{\eta}$ from a sum of thermally emitting spherical co-centric shells with temperatures $T(r) = T_0(\frac{r_0}{r})^\eta$.

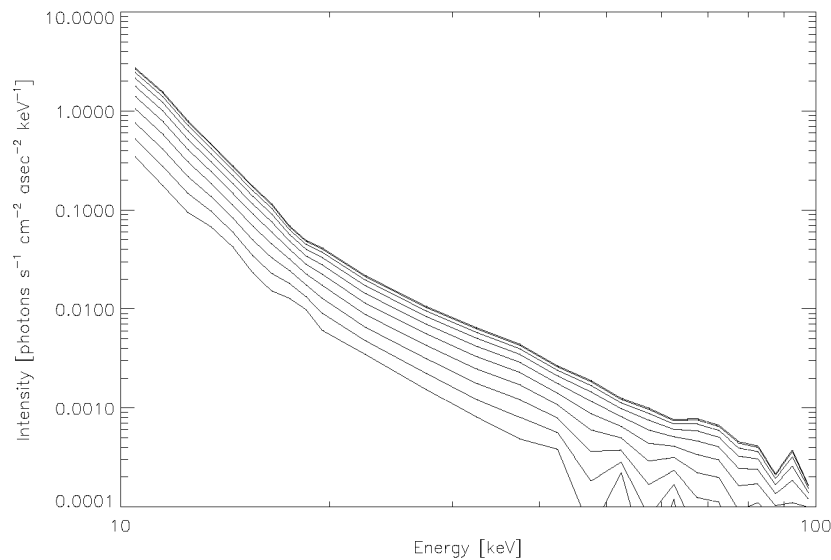


Figure 4.9: Imaging spectroscopy I: spectra at different distances from flare center position at the time of peak HXR flux. Spectra from top to bottom were taken at increasing distances, 1'' increments, starting at 0'' for the topmost spectrum. At high energies and large distances, photon fluctuation effects become important.

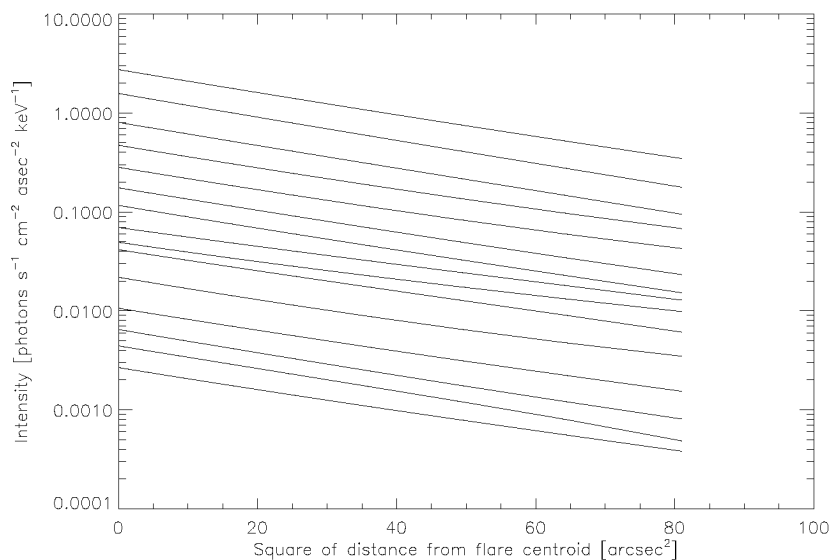


Figure 4.10: Imaging spectroscopy II: flux vs. distance from flare center position, for different energy bands. The flux in different energy bands (from 10 to 45 keV) are ordered with increasing energy, from top to bottom. From 10 to 20 keV, 1-keV bands were used. From 20 to 45 keV, 5-keV bands were used.

The flare had a gaussian shape at all energies (Fig. 4.10). The slope ($=-1/2\sigma^2$) was about -0.023 ± 0.002 , implying an apparent source sigma of $4.7(\pm 0.2)''$, or FWHM of $11(\pm 0.5)''$ in the 10-45 keV band. Note that the apparent source size is again a convolution of the true source size with the point spread function of the imaging instrument.

4.5 Spectral features

Figure 4.11 shows a spatially integrated spectrum accumulated during the peak of the HXR flux. As RHESSI's spectral response below 10 keV is not yet completely known (particularly when a shutter is in, as is the case here), spectral fitting (using the full spectral response matrix) has been done on energies above 10 keV. The data points were fitted using the SPEX³ software, with a thermal free-free bremsstrahlung and double broken power-law model.

The thermal bremsstrahlung component of the fit model yields a temperature of $T = 19.7 \pm 1.0$ MK, and an emission measure of $EM \sim 0.2 \times 10^{49} \text{cm}^{-3}$ (accurate to within a factor 2), assuming an isothermal source and $\bar{Z}=1.2$. The temperature derived from GOES-8 3-second data peaks at 10:26:51 UT at 16.7 MK, with an emission measure of $0.6 \times 10^{49} \text{cm}^{-3}$.

The power-law component had a photon flux at 50 keV of 1.5 ± 0.2 photons $\text{s}^{-1} \text{cm}^{-2} \text{keV}^{-1}$, and a spectral index of 3.0 ± 0.1 . This value is not significantly different than the ones derived in the previous section, where a different time interval was used, and where only energies in the 20-40 keV range were considered. A break in the power-law is located at 54 ± 3 keV. After this break, the photon spectral index is 3.5 ± 0.1 . Breaks are commonly observed (see, e.g. Lin & Schwartz, 1987) and do not significantly influence the energy budget (section 7).

An emission volume V can be inferred from the size of the source observed with imaging: $V = \frac{4\pi}{3}R^3$, where R is the size of the source. With $R = 2.8(\pm 0.4)''$, one finds an emitting volume of $V = 3.5 \times 10^{25} \text{cm}^{-3}$, with $2.2 - 5.2 \times 10^{25} \text{cm}^{-3}$ the range of possible values.

The thermal energy and density can then be calculated, using:

³<http://hesperia.gsfc.nasa.gov/rhessidatacenter/spectroscopy.html>

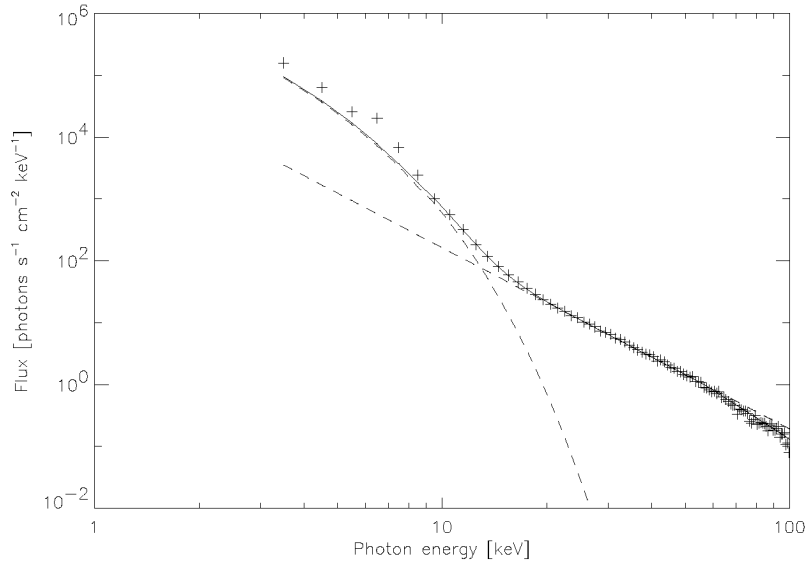


Figure 4.11: Spectrum accumulated from 10:26:05 to 10:27:23 UT, during enhanced HXR >25 keV flux. Only the front segment of detector 4 was used. The ‘+’ symbols are the data points. A fit with a thermal bremsstrahlung and a power-law is also drawn (solid line).

$$E_{th} = 3 \cdot k_B T \sqrt{EM \cdot V \cdot q} \quad , \quad (4.3)$$

$$n_e = \sqrt{\frac{EM}{V} \cdot q} \quad , \quad (4.4)$$

where EM , the emission measure, and T , the temperature, are the ones derived above. The filling factor is represented by a fraction q . An inhomogeneous medium possesses less thermal energy than a homogeneous one, for the same temperature and emission measure. $q = 1$ is assumed throughout this chapter. Eq. (4.4) yields a density of $n_e = 2.6 \times 10^{11} \text{cm}^{-3}$ (range: $2.1 - 3.3 \times 10^{11} \text{cm}^{-3}$), comparable to what is derived from TRACE in section 7.

For determination of the thermal energy in the flare (section 7), temperature and emission measure determined at the peak of the soft X-ray (SXR, <12 keV) flux are needed. Spectral fitting done around 10:27:10 UT, accumulated over three RHESSI rotations of 4.35s, yields $T = 20.8 \pm (0.9)$ MK and $EM = 2.9 (\pm 0.5) \times 10^{48} \text{cm}^{-3}$ (always assuming an isothermal plasma).

4.6 TRACE images with RHESSI overlays

Figure 4.12 shows TRACE images with RHESSI overlays at different energies. The TRACE images had exposure durations of 20–30 seconds, except for the fourth one (EUV peak), which had an exposure duration of 8 seconds. All TRACE images have been translated 10'' northerly, to align with RHESSI. The EUV band pass is dominated by a spectral line of Fe XII (195 Å) having a maximum emissivity at 1.4 MK. At high temperatures (15–20 MK), an Fe XXIV line (192 Å) appears and may add significant flux (the filter's response around 15–20 MK is still two orders of magnitude less than at 1.4 MK).

The RHESSI images' accumulation times (as labelled on top of each image) correspond loosely to the time difference between TRACE images (in integer multiples of the spin period of 4.35 s), and were all made using the CLEAN reconstruction algorithm, and subcollimators 3 to 8. Again, care has been taken to use the same aspect solution for all RHESSI images.

The TRACE observations clearly show an ejection occurring with the flare, starting in the second image of Fig. 4.12. Later it develops into the shape of a bubble, which gets constricted at the bottom (best visible in Fig. 4.12, fourth image). It does not rise beyond the TRACE field of view, but becomes turbulent (see movie available on the CD-ROM). The formation, development and constriction of the bubble is suggestive of a reconnection jet scenario speeding from the apparent X-point located at (930,-220) arcseconds from Sun center in Fig. 4.12 (fourth image). The proposed scenario is depicted in Fig. 4.13.

RHESSI overlays show that the HXR (12–25 and 25–50 keV) are emitted in the flare kernel (marked by B in Fig. 4.13). At the peak flux of HXR >25 keV, the peak positions of the sources >25 keV are shifted to smaller radial distances from Sun center ($\sim 1\text{--}2''$, best seen with Figure 4.3), consistent with the interpretation that, after being accelerated by a reconnection event, the mildly relativistic electrons precipitate in the lower corona by emitting thick-target HXR radiation. The electrons with the higher energies will lose their energy (mostly via Coulomb collisions) only in the deeper, denser chromosphere. The hot plasma being heated by the precipitation of electrons (<25 keV overlays or images in Figure 4.12 and 4.3) was apparently in the same volume. After 10:27:20 UT, when the HXR emission above 25 keV ceases, a slow outward (NW direction)

movement of the 3–12 and 12–25 keV (thermal) sources is witnessed, at a speed of about 30 km/s.

4.7 Energy budget

Table 4.2 summarizes the different energies found. In this Section, their derivation from the data is described.

Kinetic energy of precipitating electrons $E_{\text{kin,beam}}$: Assuming that the power-law component in our spectra is related to the HXRs emitted by precipitating electrons in the lower corona (thick target), an electron distribution can be determined from the relations in Brown (1971) and Hudson (1978):

$$\frac{\partial^2 N_e}{\partial E \partial t} = 3.28 \times 10^{33} b(\gamma) \frac{F_{50}}{50^{-\gamma}} E^{-\gamma-1} \quad [\text{e}^- \text{s}^{-1} \text{keV}^{-1}] \quad (4.5)$$

where γ is the photon spectral index, F_{50} is the photon flux (in photons $\text{s}^{-1} \text{cm}^{-2} \text{keV}^{-1}$) at 50 keV, E is the electron kinetic energy in keV, and $b(\gamma)$ is equal to 7.05 for $\gamma = 3$.

At low electron energies, the distribution must become flatter, reducing the photon distribution below the cut-off energy. Power-law distributions with low energy cut-offs have been fitted to the spectrum (Fig. 4.11). A cut-off above 10 keV decreases the match with observations, below 10 keV it has little influence on the fit of the photon spectrum. In the absence of effects that enhance the low-energy photon flux (such as non-uniform target ionization, Kontar et al., 2002), we initially concluded that the low-energy cut-off for the photon power-law spectrum was ≤ 10 keV. However, after careful review of this problem (cf. Chap. 5), and through the use of more appropriate fitting techniques (routine “brm_bremthick.pro” from the SolarSoft libraries), it was found that the cutoff energy seem in fact to be 39.8 keV. In the following, an electron power-law cut-off energy of 39.8 keV is used.

Determining the number of electrons that precipitated, as well as their total kinetic energy, is simply done by integrating over time and energy (from 39.8 keV to ∞). The total kinetic energy in all precipitating electrons is 1.7×10^{29} erg. At peak time, an average of 2.2×10^{34} electrons/s precipitated, for a total of about 1.7×10^{36} electrons.

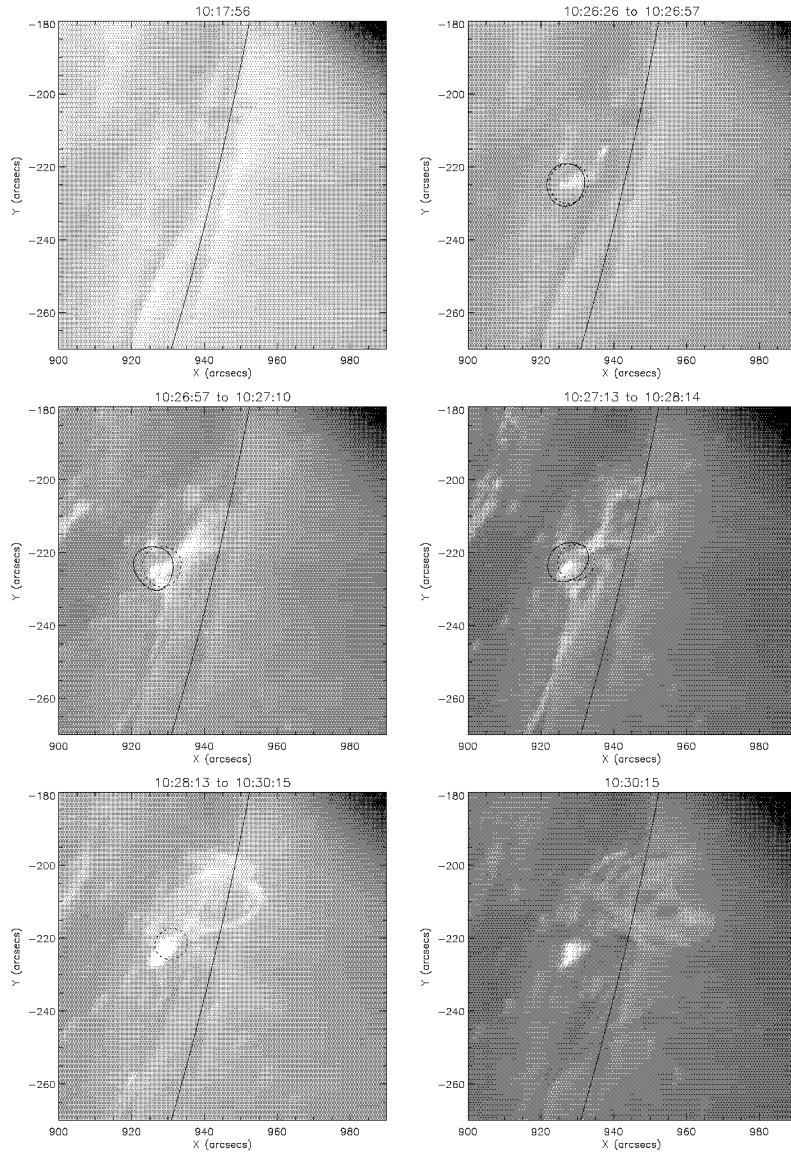


Figure 4.12: TRACE images at 195\AA with RHESSI overlays of different energy bands. The contours correspond to the 50% level. The dotted black contour corresponds to the 12-25 keV band, the full black contour to the 25-50 keV band. As shown in Fig. 4.3, the 3-12 and 12-25 keV images differ by less than $1''$ throughout the flare, as do the 25-50, 50-100, and 100-300 keV images. The first image shows the region of interest before the flare. The second one was taken during the rise of the HXRs. The third one is between HXR and SXR peaks, the fourth one between SXR (3-12 keV) and EUV peak (flash phase). The last two were taken during the decay phase.

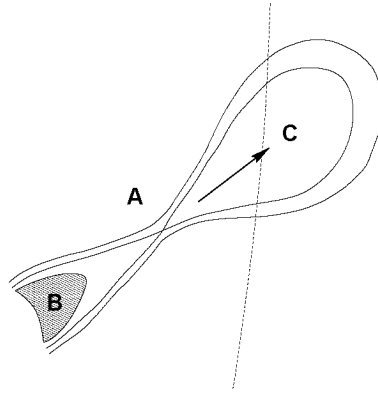


Figure 4.13: Schematic drawing of field lines and interpretation of TRACE image: A = X-point (reconnection site), B = flare kernel, C = upward reconnection jet.

Kinetic energy of ejected plasma (bulk motion) E_{mot} : Assuming isothermal plasma, each of TRACE’s CCD pixel possesses a flux:

$$F = f_{195}(T) \cdot EM, \quad (4.6)$$

where F is the flux (‘data number’, in TRACE parlance, normalized to 1 second) in the pixel (CCD dark currents have been subtracted), EM the emission measure observed in that pixel, and $f_{195}(T)$ a known function of the temperature T (the filter response function) (Handy et al., 1999). As TRACE was observing with only one filter band (195Å, with one aluminium filter in the FOV), temperature and emission measure cannot be determined without additional information or assumptions. $f_{195}(T)$ peaks at $T=1.4$ MK. Given a certain flux in a pixel, this temperature yields a lower limit of the emission measure (and hence, the density). RHESSI spectral fitting (section 5) yields an independent measurement, a temperature of 20.8 MK for the flare kernel. Assuming that the ejecta temperature is in the range 1.4-20.8 MK, lower and upper limits can be found for the emission measure, and in particular, the density.

To determine the total thermal energy and the energy of bulk motion of the ejecta, we need to know the number of particles in the ejecta. This was done for the third TRACE image in Figure 4.12 in the following manner. The volume of material in a pixel is $V = (\text{pixel area}) \times l$, where l is the smallest dimension of the ejecta feature being examined. Combined with Eq. (4.4), and knowing that pixel’s emission measure (cf. Eq. 4.6), a density can be calculated. The average densities $n_{e,\text{ejecta}}$ derived in this manner (assuming unity filling factor) were $5 \times 10^9 \text{cm}^{-3}$ for $T=1.4$ MK and 10^{11}cm^{-3} for $T \sim 10$ MK (the temperature were the filter response

was lowest). These densities can be compared with those indicated by the observed decimetric type III bursts in the range $1.2 \times 10^9 < n_e < 1.3 \times 10^{10} \text{cm}^{-3}$ (assuming emission at the second harmonic).

The shape of the ejecta seen here can be approximated by a truncated cone. The volume of all the ejected material was estimated to be $V_{ejecta} = (1.1 \pm 0.2) \times 10^{27} \text{cm}^3$. Hence, $(n_{e,ejecta} \cdot V_{ejecta})$ yields 4.5×10^{36} to 1.3×10^{38} electrons. In the flaring kernel, TRACE finds a density of $n_{e,kernel} \approx 3.5(\pm 0.1) \times 10^{11} \text{cm}^{-3}$, for temperatures in the range 15-20 MK.

As a self-consistency check, the emission measure of the brightest EUV region outside the flare kernel (the X-point in Fig. 4.13, fourth image) was determined (assuming an upper limit temperature of 20.8 MK). The result of $1.8 \times 10^{47} \text{cm}^{-3}$ is below the $EM_{kernel} = 2.2 \times 10^{48} \text{cm}^{-3}$ determined from the RHESSI spectrum for the flare kernel. As RHESSI's dynamic range is currently about 10, this means that this region would have been indeed invisible to imaging, even if it were as hot as the flare kernel.

The bulk motion of the ejecta during the impulsive phase of the flare was determined by TRACE difference images (Fig. 4.12, two and three), and was found to be $v = 290 \pm 70 \text{ km/s}$. It is used to compute the energy of motion of the ejecta, $E_{mot} \approx 0.5 m_p (n_{e,ejecta} \cdot V_{ejecta}) v^2$, where m_p is the proton mass. This yields a result between $2.0 \times 10^{27} \text{erg}$ and $1.3 \times 10^{29} \text{erg}$.

Thermal energy of flaring kernel $E_{th,kernel}$: Using the RHESSI-derived values from section 5 and Eq. (4.3), a value of $8.7 \times 10^{28} \text{ erg}$ is derived. The possible range of values is $6.0 - 12 \times 10^{28} \text{ erg}$.

Thermal energy of ejected plasma $E_{th,ejecta}$: We again use $3 k_B T n_e V$, where T is assumed to be between 1.4 and 20.8 MK, and n_e and V now relate to the ejecta. This yields: $E_{th,ejecta} = 2.6 \times 10^{27}$ to $1.1 \times 10^{30} \text{ erg}$.

Radiated energy from the flaring kernel: $E_{rad,kernel}$: assuming a temperature of 19.7MK, using $EM_{kernel} = 2.2 \times 10^{48} \text{cm}^{-3}$, and integrated between 10:26:05 to 10:27:23 UT, an amount of $3.5(\pm 1.7) \times 10^{27} \text{ erg}$ has been radiated as the plasma cooled down. The energy radiated in EUV was not considered.

Total radiated HXR from precipitating electrons E_{HXR} : integrating the power-law in section 5 between 10:26:05 to 10:27:23 UT yields a total of $3.2(\pm 1.1) \times 10^{23} \text{ erg}$.

Type	best estimate	range
$E_{kin,beam}$	1.7×10^{29} erg	1.5 to 2.1×10^{29} erg
$E_{th,kernel}$	8.7×10^{28} erg	6.0 to 12×10^{28} erg
$E_{th,ejecta}$	$\sim 10^{28-29}$? erg	2.6×10^{27} to 1.1×10^{30} erg
$E_{mot,ejecta}$	$\sim 10^{29}$ erg	2×10^{27} to 1.3×10^{29} erg
$E_{rad,kernel}$	3.5×10^{27} erg	$\pm 1.7 \times 10^{27}$ erg
E_{HXR}	3.2×10^{23} erg	$\pm 1.1 \times 10^{23}$ erg

Table 4.2: Energy budget of the flare on 2002/02/26 during the impulsive phase (from about 10:26:10 to 10:27:10 UT).

4.8 Conclusions

The thermal energy content of the hot flare plasma (flare kernel) is slightly less than, but of the same order as, the energy in the non-thermal electron beam (Table 4.2). This is consistent with the standard flare scenario where the energy is first released into non-thermal particles and then converted into thermal energy. As some of the target may not be heated to high enough temperatures to radiate X-rays, the energy input by the particle beam can exceed the output visible in soft X-rays. The ratio of beam energy over thermal energy in the kernel is ~ 2 . de Jager et al. (1989) had found such ratios, and also ratios of more than an order of magnitude! A major uncertainty of the energy budget is the source volume, from which several parameters are derived, such as density, mass and energy. The low-energy cut-off of the non-thermal electron spectrum is the major inaccuracy of the beam energy.

The size of the source was stable in energy and time. The flare kernel contained initially both the thermal and non-thermal electrons. Later, after the HXR emission above 25 keV ended, the thermal source drifted slowly (~ 30 km/s) outwards.

If interpreted by reconnection at point A (Fig. 4.13), the conclusion is that the geometry of energy release and partition was unsymmetrical. In the downward jet, not observed by TRACE, the energy was largely transferred to accelerate electrons. The proposed scenario also suggests that the accelerated electrons mostly moved downward from the reconnection site or were accelerated only in the downward reconnection jet. If the observed ejecta is interpreted as the other reconnection jet, this upward jet involved less energy, which showed up mostly as heat. However, the

energy estimate of the latter is less accurate.

RHESSI imaging with improved dynamic range may be able to search for the thin-target emission of energetic electrons in the ejecta. Nevertheless, the absence of appreciable decimetric radio emission corroborates the conclusion that acceleration took place mostly below point A and in the downward direction.

The now available high-resolution RHESSI and TRACE observations allow a more quantitative investigation of flare energies. The study of a compact flare yields a detailed scenario (that may not apply to all flares). Based on the above interpretations, we conclude that energy partition is not symmetric about the X-point of reconnection. Most of the initial energy first appears as energetic electrons in the lower, stationary part, and less than half is manifest in thermal energy and even less in bulk motion of the upper part.

More flares need to be analyzed to study the influence of the magnetic field geometry and density on energy partition.

Chapter 5

Thermal and non-thermal energies of solar flares

The tale grew in the telling.

J.R.R. Tolkien (1892–1973)

ABSTRACT: The energy of the thermal flare plasma and the kinetic energy of the non-thermal electrons in 9 medium-sized solar flares have been determined from RHESSI observations. The emissions have been carefully separated in the spectrum. The turnover or cutoff in the low-energy distribution of electrons has been studied by simulation and fitting, yielding a reliable lower limit to the non-thermal energy. It remains the largest contribution to the error budget. Other effects, such as albedo, non-uniform target ionization, hot target, and cross-sections on the spectrum have been studied. The errors of the thermal energy are about equally as large. They are due to the estimate of the flare volume, the assumption of the filling factor, and energy losses. Within a flare, the non-thermal/thermal ratio increases with accumulation time, as expected from loss of thermal energy due to radiative cooling or heat conduction. Our analysis suggests that the thermal and non-thermal energies are of the same magnitude. This surprising result may be interpreted by an efficient conversion of non-thermal energy to hot flare plasma.

5.1 Introduction

In the standard model of solar flares, a major part of the energy is first released into energetic, non-thermal electrons and possibly ions. These particles, guided by magnetic field lines, may be lost in interplanetary space, but mostly precipitate into the lower corona or upper chromosphere where they lose their energy by Coulomb collisions with the denser medium. This energy is believed to heat up the ambient plasma to tens of millions of degrees, which will rise and fill the coronal loop. An interesting question is thus the relation between non-thermal and thermal energies. The difference between them may indicate conversion losses and/or other forms of primary energy release.

How does total kinetic energy of electrons that precipitated compare to the thermal energy of the plasma? In the pre-RHESSI era and in RHESSI first results papers, this issue had been addressed (see e.g. de Jager et al., 1989; Saint-Hilaire & Benz, 2002), with the result that the kinetic energy was often reported up to an order of magnitude or more than the observable thermal energy. Others (Gan et al. 2001) have managed to conclude just the opposite.

The hot thermal plasma emits soft X-rays. They differ in the spectrum from the X-rays emitted by the non-thermal electron bremsstrahlung at higher energies. Soft and hard X-rays can thus be used to determine the thermal and non-thermal energies, respectively. In practice, however, many uncertainties limit the precision of the energy determination. Unfortunately, the two emissions are usually cospatial and overlap in photon energies in the range from about 10 to 25 keV. This is furthermore the range of the emission of the non-thermal photons that carry the information on the dominant lowest-energy part of non-thermal energies. The distinction between the two forms of energy requires a high spectral resolution in the critical range.

An accurate derivation of non-thermal energy from the spectrum is not trivial. In previous work the observed hard X-ray spectrum was converted into electron energies assuming that they impinge onto a thick target. The energies were integrated starting at some assumed lower limit or at the crossover between thermal and non-thermal emissions in the observed photon spectrum. As the derived electron energy distribution is a power law with large index, the result depends much on the lower bound of integration. In addition, the photon spectrum is influenced by

several effects. The non-thermal bremsstrahlung of a coronal source is reflected by the dense layers below, thus appears to be brighter (Bai & Ramaty 1978; Alexander & Brown 2003). Precipitating electrons above some energy penetrate into the chromosphere where they lose energy by collisions with neutrals and are more efficient in bremsstrahlung radiation than in the completely ionized corona (Kontar et al. 2003). The Sun is not a simple cold, thick target (Emslie et al. 2003). Finally, the various approximations for electron cross-section used in the literature yield different values in particular at relativistic particle energies.

On the other hand, the accurate determination of the thermal energy also poses problems. Thermal energies are best estimated from the thermal bremsstrahlung spectrum, yielding the plasma temperature and the emission measure. The volume of the thermal plasma must be estimated from the size of the source and an assumption on the filling factor. The ambient plasma cools down by either heat conduction or radiative cooling (i.e. thermal bremsstrahlung of an optically thin plasma) (Porter and Klimchuk, 1995; Aschwanden et al. 2001). Thus, thermal energy is lost before measured. A reliable determination of the errors is therefore as important as the final ratio between the two forms of energy.

In this chapter, we determine energy budgets for several flares observed by the Reuven Ramaty High Energy Solar Spectroscopic Imager (RHESSI) (Lin et al. 2003). The imaging capabilities, high spectral resolution and broad photon energy coverage of RHESSI make this instrument ideal to determine the two energies with much higher precision and study their relation. Medium-sized flares (upper C and lower M class) have been selected to avoid photon pile-up, complicated source structure and other conundrums of larger flares. With a careful RHESSI analysis, some -but not all- of the uncertainties or assumptions used by previous authors may be removed, and more accurate results obtained.

This chapter will start with a section discussing already well-established effects of solar flare bremsstrahlung emissions and the various high-energy electron cross-sections available in the literature. The next section will deal with the method proposed to determine flare energies. Observational results from RHESSI will then be presented, and the ratios of cumulative non-thermal energy over thermal energy increase during the same time intervals will be examined.

5.2 Basic theory

5.2.1 Thick-target bremsstrahlung emission

An initial (injection) electron beam with distribution $F_0(E_0)$ electrons $\text{s}^{-1} \text{keV}^{-1}$ passing through a dense –although still optically thin– plasma emits HXR radiation according to the following formula (Brown 1971):

$$I_{thick} = \frac{1}{4\pi D^2} \int_{E_0=\epsilon}^{\infty} F_0(E_0) \int_{E=\epsilon}^{E_0} \frac{Q_B(E, \epsilon)}{E Q_c(E)} dE dE_0, \quad (5.1)$$

where $I_{thick}(\epsilon)$ is the observed photon spectrum seen at distance D (assumed to be 1 AU in the following) from the site of emission, in photons $\text{s}^{-1} \text{cm}^{-2} \text{keV}^{-1}$. Isotropic emission is assumed throughout this work. $Q_B(E, \epsilon)$ is the bremsstrahlung differential cross-section, for an electron of energy E emitting a photon of energy ϵ . $Q_c(E)$ is the energy-loss cross-section due to Coulomb collisions with the ambient plasma.

In the thick-target model, the electrons are assumed to lose all their energy due to Coulomb collisions (thereby heating the local medium) within the spatial resolution of the instrument. Energy losses due to bremsstrahlung are neglected (they start to be competitive for electrons above ~ 300 MeV: those energies will not interest us in this work). The inner integral corresponds to the photon spectrum emitted by an electron of initial energy E_0 , being slowed down to energy ϵ . Photons are assumed to reach the observer unimpeded.

The Coulomb collisional cross-section for energy-loss is taken to be

$$Q_c(E) = \frac{2\pi e^4 \Lambda}{E^2} = \frac{K}{E^2} \quad (5.2)$$

where Λ is the Coulomb logarithm for collisions. For a fully ionized plasma, where collisions are mostly against free electrons, $\Lambda \approx 20$, leading to $K = 2.6 \times 10^{-18} \text{cm}^2 \text{keV}^{-2}$. For a partially ionized plasma of ionization level x Brown (1973) and Kontar et al. (2003) give

$$Q_c(E) = \frac{2\pi e^4 \Lambda}{E^2} (\lambda + x), \quad (5.3)$$

where $\Lambda = 12.9$ and $\lambda = 0.55$. The energy-loss cross-section is hence about 2.8 times larger for a fully-ionized ($x = 1$) plasma than for a neutral ($x = 0$) gas, where collisions are mostly against bound electrons.

If the temperature of the target is high, i.e. approaching the precipitating electron's kinetic energy, the non-radiative loss of beam energy by collisions decreases (down to no losses for electrons with kinetic energy comparable to the target's kT). When $E/kT < 1$, the electron exchanges energy with electrons of the thermal plasma that can reemit it by bremsstrahlung at the same energy. Thus the bremsstrahlung efficiency increases. A corrective factor to $Q_c(E)$ is given by Emslie (2003), in the case of a fully-ionized plasma:

$$g_{th} = erf\left(\sqrt{\frac{E}{kT}}\right) - \frac{4}{\sqrt{\pi}}\sqrt{\frac{E}{kT}}e^{-\frac{E}{kT}} \quad (5.4)$$

The correction is more than 10% only for $E/kT < 4$. It will not be relevant for this work because at these low energies the photon spectrum is dominated by the thermal emission.

At high energies, the previous non-relativistic (NR) limit for $Q_c(E)$ no longer holds. The full quantum relativistic Bethe-Bloch formula (Longair, 1992) for energy loss is:

$$-\left(\frac{dE}{dx}\right)_{coll} = \frac{4\pi e^4}{m_e v^2} n_e (\Lambda + \ln(\gamma^2) - \beta^2) \quad , \quad (5.5)$$

where Λ is the usual non-relativistic Coulomb logarithm, γ the Lorentz factor, and $\beta = \frac{v}{c}$. In its NR limit, the Bethe-Bloch formula yields exactly the same cross-section as before ($\sim \frac{1}{E^2}$), up to electron kinetic energies nearing the electron rest mass energy, after which the dependence is approximately $\sim \frac{1}{E}$. Hence, at high energies, Coulomb losses are larger than with the NR approximation (Fig. 5.1), leading to a softening of the emitted thick-target photon spectra, as shown in Fig. 5.2. At non-relativistic energies, the effect is only important for hard electron distributions. Using the NR cross-section thus underestimates the power-law index of the electron distribution even at NR photon energies.

The Bethe-Heitler non-relativistic bremsstrahlung differential cross-section is used most often in the literature. It gives the cross-sectional area for the emission of a photon of energy ϵ by an electron of energy E , per unit photon energy. The Bethe-Heitler bremsstrahlung cross-section (formula 3BN(a) of Koch and Motz 1959, Brown 1971)

$$Q_B(E, \epsilon) = \frac{Z^2 \kappa_{BH}}{\epsilon E} \ln\left(\frac{1 + \sqrt{1 - \epsilon/E}}{1 - \sqrt{1 - \epsilon/E}}\right) \quad [\text{cm}^2 \text{ keV}^{-1}] \quad , \quad (5.6)$$

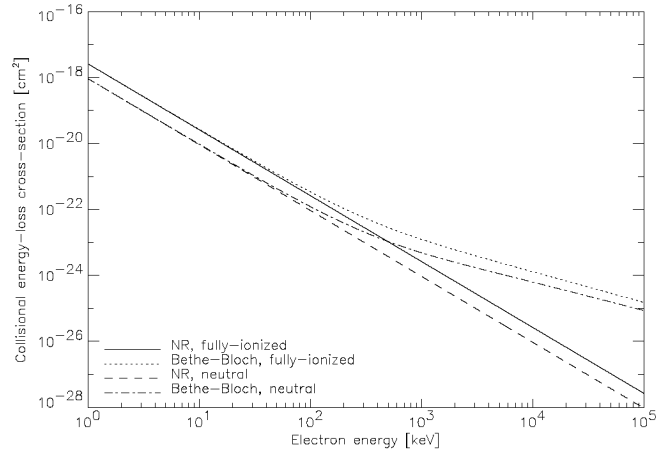


Figure 5.1: Energy-loss cross-section, for the usual non-relativistic (NR) case and from the Bethe-Bloch formula. Notice also the slight dependence of the spectral index at relativistic energies with the ionization level. The spectral index at high energies is ~ 0.93 for a fully-ionized plasma, and ~ 0.87 for a neutral medium.

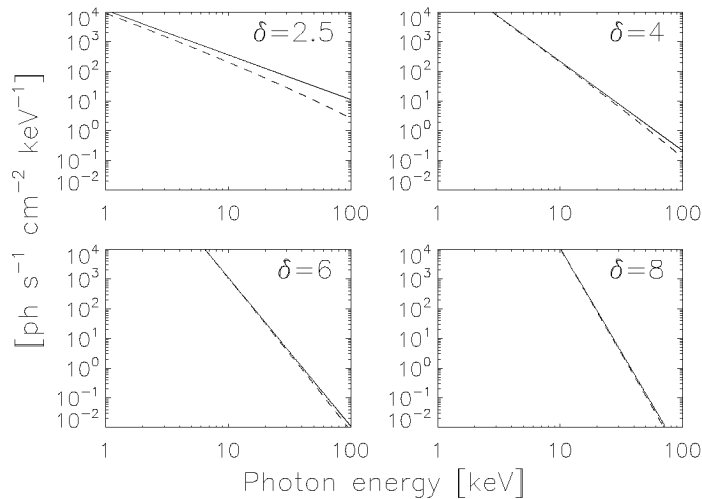


Figure 5.2: Synthetic photon spectra observed at Earth, obtained from power-law injection electron distributions $F(E_0) = A_{50} \left(\frac{E_0}{50}\right)^{-\delta}$, with $A_{50} = 10^{33}$ electrons $\text{s}^{-1} \text{keV}^{-1}$. The *Solid lines* were computed using the non-relativistic (NR) Coulomb cross-section (Eq. 5.2); the *dashed lines* were computed using the Bethe-Bloch cross-section (Eq. 5.5).

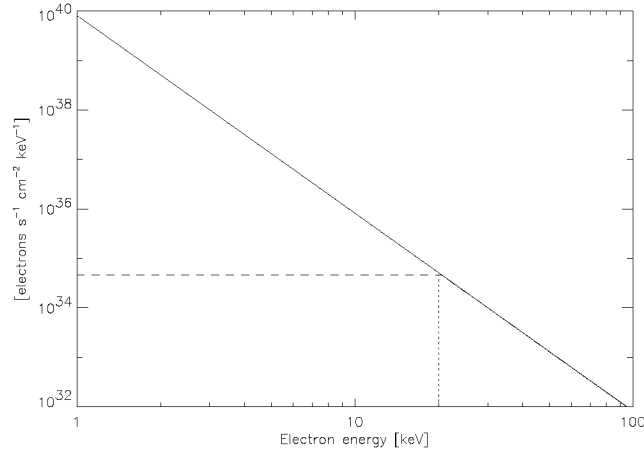


Figure 5.3: Electron power-law spectrum of index 4 and a 50 keV electron flux of $A_{50} = 1.295 \times 10^{33}$ electrons $\text{s}^{-1} \text{keV}^{-1}$ (values derived from the 2002/02/26 10:26 C9.6 flare, during peak HXR flux). *Solid line:* No cutoff. *Dotted line:* cutoff at 20 keV. *Dashed line:* turnover at 20 keV. Above 20 keV, all lines are super-imposed.

$$\kappa_{BH} = \frac{8}{3} \alpha r_e^2 m_e c^2 = 7.9 \times 10^{-25} \text{ [cm}^2 \text{ keV]} \quad (5.7)$$

is not the most accurate of bremsstrahlung cross-sections, but does offer the tremendous advantage of providing an analytical solution to Eq. 5.1, when used in conjunction with the non-relativistic limit for collisional losses (Eq. 5.2) (See Eq. 5.1). Unless otherwise noted, all synthetic photon spectra shown in this section were made with the non-relativistic Bethe-Heitler bremsstrahlung cross-section, for easy comparison with theory.

From Tandberg-Hanssen and Emslie (1988), using Eqs. (5.2) & (5.6), an injected power-law electron distribution of the form $F_0(E) = A_e E^{-\delta}$ into a thick target produces a power-law photon spectrum

$$I_{thick}(\epsilon) = A_\epsilon \cdot \epsilon^{-\gamma} \quad (5.8)$$

with

$$A_\epsilon = \frac{A_e}{4\pi D^2} \frac{\overline{Z^2} \kappa_{BH}}{K} \frac{B(\delta - 2, 1/2)}{(\delta - 1)(\delta - 2)} \quad (5.9)$$

$$\gamma = \delta - 1 \quad (5.10)$$

where A_e is in electrons $\text{s}^{-1} \text{keV}^{-1}$, $\overline{Z^2}$ is 1.44 for typical coronal abun-

dances, and B is the beta function [$B(a, b) = \frac{\Gamma(a)\Gamma(b)}{\Gamma(a+b)}$]. Numerically,

$$I_{thick}(\epsilon) = 1.51 \times 10^{-34} \frac{B(\delta - 2, 1/2)}{(\delta - 1)(\delta - 2)} A_e \epsilon^{1-\delta}, \quad (5.11)$$

where the units are photons $\text{s}^{-1} \text{cm}^{-2} \text{keV}^{-1}$. The non-thermal kinetic power of the injected electron beam may be computed:

$$P = \int_?^{\infty} E \cdot F_0(E) dE \quad (5.12)$$

The introduction of some kind of a cutoff at low energies is necessary by the fact that the integral diverges at zero energy. Assuming that $F_0(E_0)$ remains a power-law below the thermal energy in the acceleration region is not physical. In the past, a sharp low-energy cutoff in $F_0(E_0)$:

$$F_0(E_0) = \begin{cases} A_e E_0^{-\delta} & \text{for } E_0 > E_{co} \\ 0 & \text{for } E_0 < E_{co} \end{cases} \quad (5.13)$$

was often assumed, as shown in Fig. 5.3. This situation seems physically not realistic as such a configuration leads to plasma instabilities. Such instabilities have growth rates typically of the order of the local plasma frequency, i.e. orders of magnitude shorter than the propagation time of the beam within the acceleration region. The turnover model shown in Fig. 5.3 seems physically closer to reality:

$$F_0(E_0) = \begin{cases} A_e E_0^{-\delta} & \text{for } E_0 > E_{to} \\ A_e E_{to}^{-\delta} & \text{for } E_0 < E_{to} \end{cases} \quad (5.14)$$

We note, however, that recent simulations of stochastic electron acceleration, such as by Miller (2000) and Petrosian et al. (Taos workshop, 2003) predict an energy distribution in the acceleration region still increasing below the turnover energy. Such an inclined turn-over would be extremely difficult to distinguish from a flat turnover, as its effects were in the lowest energy photons, where the thermal emission dominates. Thus, the flat turnover model defined in Fig. 5.3 may not be the true distribution, but yields rather a lower limit to the total non-thermal energy estimate. As discussed in Section 5.7, collisional energy losses during propagation in the corona tend to impart such a shape to the electron spectrum before it reaches the denser lower corona or upper chromosphere and emits most

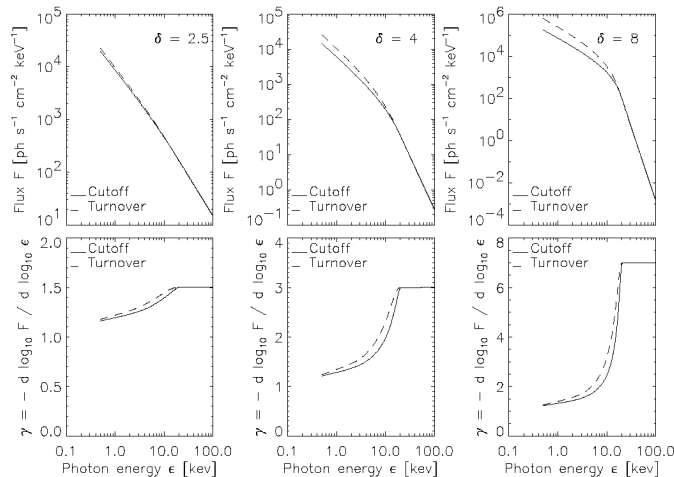


Figure 5.4: *Top:* Photon spectra and their spectral indices (*bottom*), computed from different injection electron power-laws of spectral indices δ , using the Brown (1971) cross-sections. The electron spectra had all a 20 keV cutoff/turnover energy (see Fig. 5.3).

of the bremsstrahlung. Thus, these low-energy electrons mainly heat the corona and do not contribute to the evaporation.

The photon spectra of the different model distributions of electrons in a beam impinging on a thick target have been calculated using the Brown (1971) model (i.e. using the non-relativistic Bethe-Heitler bremsstrahlung cross-section, and non-relativistic collisional losses). Both turnover and cutoff model lead to a photon spectrum that is rounded off at low energies, as electrons produce photons of the same energy or below (see Fig. 5.4). The spectral index of the turnover model is slightly larger than for the cutoff model. Note that it is not a constant value of 1.5 as is sometimes assumed. Both tend asymptotically towards ~ 1.15 for all δ as the photon energy approaches zero. The usually observed superposition of a thermal component (or several of them) to the power-law spectrum further makes an observational distinction in the spectrum exceedingly difficult. As the cutoff model has been widely used in the literature and even seems to be supported by recent RHESSI results, both have been examined in the following.

If $F_0(E_0)$ has a cutoff with the shape defined in Eq. (5.13), the non-thermal kinetic power contained in the beam of electrons is given by:

$$P_{cutoff} = \frac{A_e}{\delta - 2} E_{co}^{-\delta+2} . \quad (5.15)$$

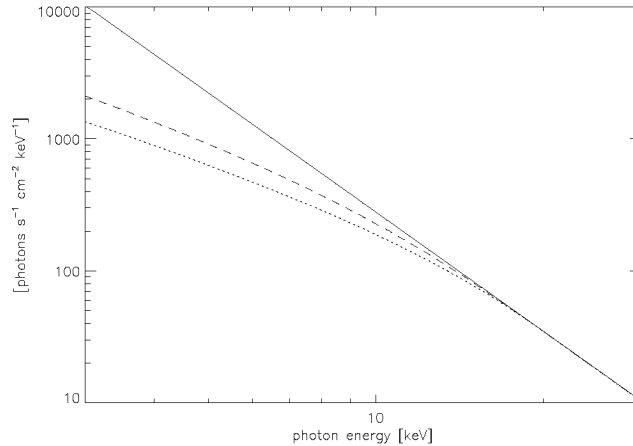


Figure 5.5: Photon spectrum observed at 1 AU, produced by an electron power-law distribution of spectral index $\delta=4$, and a 50 keV electron flux of $A_{50} = 1.295 \times 10^{33}$ electrons $s^{-1} keV^{-1}$. *Solid line:* No cutoff. *Dotted line:* Cutoff at 20 keV. *Dashed line:* Turnover at 20 keV.

On the other hand, if $F_0(E_0)$ has the form of a turnover as described in Eq. (5.14),

$$P_{turnover} = \frac{A_e}{\delta - 2} E_{to}^{-\delta+2} \left(1 + \frac{\delta - 2}{2} \right) . \quad (5.16)$$

Figure 5.5 is an enlargement of the turnover region in the photon spectrum. Note that the apparent photon turnover energy in Fig. 5.5 is below the electron cutoff/turnover energy (20 keV) as electrons emit photons also at energies lower than their initial kinetic energy. This has been further investigated in Figs. 5.6 and 5.7. Synthetic photon spectra were produced from electron distributions with different power-law indices δ , using the Brown (1971) approximation for simplicity. The spectra were then fitted with a double power-law of spectral index 1.5 below the break, and spectral index $\gamma (= \delta - 1)$ above it. The intersection of the two power-laws defines a photon turnover energy ϵ_{to} which is far below the electron cutoff energy E_{co} or turnover energy E_{to} . Fig. 5.7 displays the ratio of the photon turnover energy ϵ_{to} to either E_{co} or E_{to} . These ratios are smaller for the cutoff model than for the turnover model. If the photon turnover energy ϵ_{to} is used instead of E_{co} or E_{to} , the derived non-thermal power in the electron beam may be larger by more than an order of magnitude.

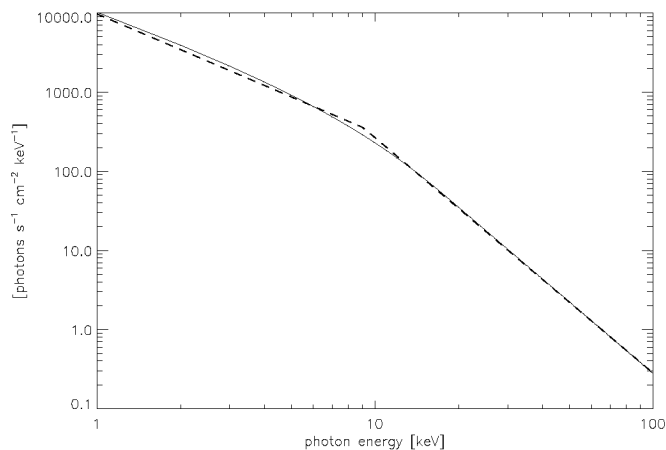


Figure 5.6: Fitting a photon spectrum with power-laws. A synthetic photon spectra (solid line) generated from an electron power-law with $E_{to}=20$ keV and $\delta=4$ (dashed curve in Fig. 5.5) was fitted with a broken power-law (dashed line). The photon power-law spectral index right of the break has a $\gamma=\delta-1=3$ spectral index. The power-law left of the break energy ϵ_{to} had a fixed spectral index of 1.5. For this example, fitting yields $\epsilon_{to}=9$ keV and a photon spectral index of 2.97 right of this break.

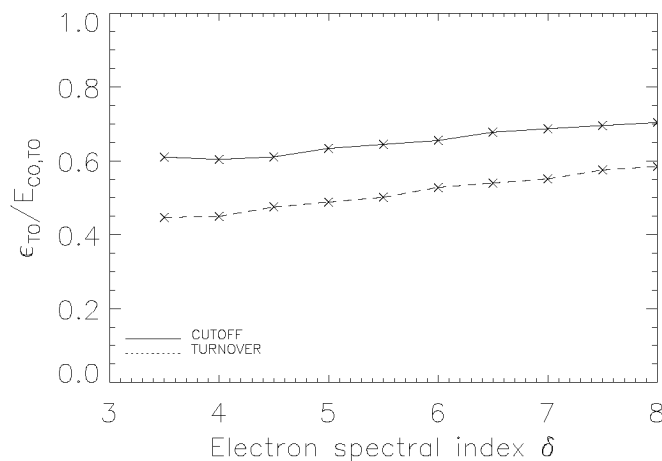


Figure 5.7: The ratio of the fitted turnover energy in the photon spectrum ϵ_{to} to the turnover resp. cutoff energy in the electron beam distribution, as a function of the electron spectral index right of $E_{co,to}$.

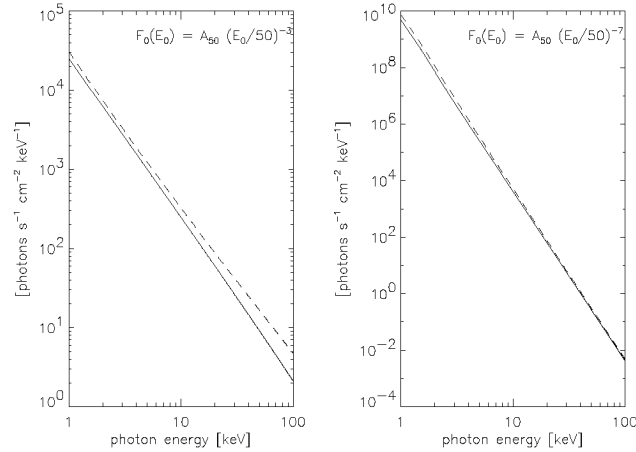


Figure 5.8: Comparisons of photon spectra calculated using different bremsstrahlung cross-sections. The *solid* line was obtained using the non-relativistic Bethe-Heitler cross-section, whereas the *dashed* line was obtained using the Haug cross-section. *Left:* An electron beam with power-law index $\delta = 3$ was assumed, *right:* $\delta = 7$.

5.3 Known and unknown errors in computing non-thermal energies

5.3.1 Errors due to approximations of bremsstrahlung cross-section, collisional energy loss cross-sections, and other factors

Haug (1997) has derived a more accurate bremsstrahlung differential cross-section than the non-relativistic Bethe-Heitler one. The Haug cross-section should hold up to ultra-relativistic electron energies (the worst inaccuracy, of about 5.5%, occurring for 1.8 MeV electrons). Fig. 5.8, 5.9, and 5.10 compare photon spectra obtained using either of the two cross-sections. As shown in Fig. 5.8, the Bethe-Heitler bremsstrahlung cross-section slightly underestimates the emission even at energies below 100 keV. The effect is particularly significant for hard electron distributions.

The difference between the relativistic (Haug) and non-relativistic (Bethe-Heitler) cross-sections for bremsstrahlung is further illustrated in Fig. 5.9. In general, the discrepancy is about 10% , but could be as high as 20% even at energies below about 20 keV (the ones that contribute

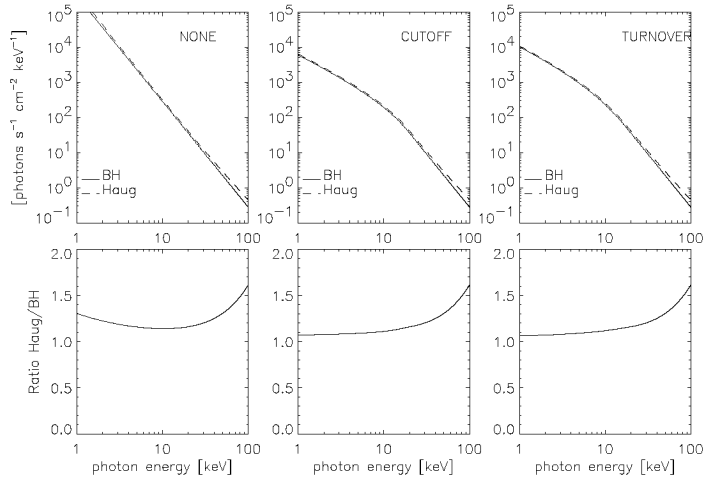


Figure 5.9: Comparisons of photon spectra obtained from electron energy distributions with and without cutoff or turnover as defined in Fig. 5.3. The *upper row* shows both photon spectra, using the Bethe-Heitler bremsstrahlung formula of Eq. (5.6) (solid line) or the Haug cross-section (dashed line). The *lower row* displays the ratio of the two spectra.

the most in determining the total non-thermal energy). For harder electron distribution, the contribution of relativistic electrons to lower energy photons becomes more important, and the difference increases.

Fig. 5.10 displays the effect of different bremsstrahlung cross-sections on the spectral index of the photons γ . The Kramer bremsstrahlung cross-section is a simplified version of the non-relativistic Bethe-Heitler one (Eq. (5.6)) where the logarithm term has been set to 1. Non-relativistic collisional losses have been used. The Haug cross-section is considerably larger for relativistic electron energies. Thus, high-energy electrons produce also more photons with low energies. If the energy distribution is very hard, such as $\delta = 2.5$, the spectrum at low energies has an important contribution from photons produced by relativistic electrons. In reality, the situation is not as drastic as shown in the top leftmost plot of Fig. 5.10: The contribution of highly-relativistic electrons to the production of low-energy photons is limited by the following three factors:

- Collisional losses of relativistic electrons are more important than if using the non-relativistic approximation.
- Furthermore, bremsstrahlung losses become similar –and start to exceed– (relativistic) collisional losses, at around 300 MeV.

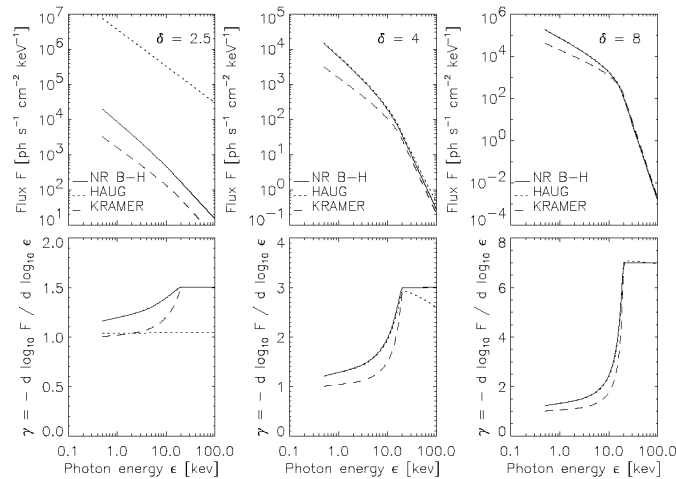


Figure 5.10: *Top row:* Synthetic spectra for different electron power-law distributions (all with a cutoff at 20 keV and index δ) and different bremsstrahlung cross-sections. Spectral indices obtained using different bremsstrahlung cross-sections are shown in the *bottom row*.

- Magnetobremstrahlung can become non-negligible. For example, in a 100 Gauss field, 10 MeV electrons lose about as much energy to synchrotron radiation as by (relativistic) collisions in a 10^{10} cm^{-3} fully-ionized plasma ($\sim 4 \text{ keV/s}$ for each mechanism). Magnetobremstrahlung losses increase with the square of the electron energy, and the square of the magnetic field strength.

We conclude that the choice of the bremsstrahlung cross-section has an effect on the spectrum at energies below the electron cutoff/turnover energy. The relativistic Haug bremsstrahlung cross-section is important for non-thermal electron distributions with small δ . The use of the Kramer cross-section leads to considerable errors and is not recommended.

In this section, the focus has been so far on studying different bremsstrahlung cross-sections. We have already noted in the previous section that the choice of approximation for the collisional cross-section also has an effect as it changes the efficiency for bremsstrahlung emission. The relativistic Bethe-Bloch formula yields a higher collision rate at higher energies and thus reduces the bremsstrahlung emissivity for a given initial electron energy. The effect of using this more proper formula for relativistic collisional losses at non-relativistic energies has been discussed earlier and shown in Fig. 5.2. We note here that the Bethe-Bloch cross-section is very close to what is used in RHESSI software.

In the rest of this section, other approximations and factors are presented that also influence the photon spectrum and thus are possible sources of error for the derived electron energy distribution. Other effects on the photon spectrum are non-uniform target ionization (Brown 1973) and the albedo effect (Compton back-scattering on the photosphere, Bai and Ramaty, 1978). They complicate the observed photon spectra by the simple fact that the amplitude of their effects varies with the energy. Kontar et al. (2003) for non-uniform target ionization and Alexander & Brown (2003) for the albedo effect have provided corrections. We have used their formulas to compute correction factors in the numerical examples given below.

Finally, the possible presence of some high-energy cutoff (or break) in the injected electron distribution affects the photon spectrum at lower energies. The effect has been simulated numerically. A sharp electron high-energy cutoff at energy E_h , would lead to a noticeable deviation from power-law behavior starting already at photon energies above $\sim \frac{E_h}{3}$, where a pronounced rollover in the spectrum should occur. This was not observed in our selection of (mostly M-class) flares, at least below 35 keV, the upper limit of the fitting interval used in our data analysis.

5.3.2 Some numerical examples

How far from the truth are we if, from an observed photon power-law in the 10-35 keV band, we derive its electron power-law energy distribution using the Brown (1971) thick-target model (i.e. perfect power-law at all energies, non-relativistic cross-sections, cold target, no albedo, uniform 100% ionization)? To estimate the effect of the different correction factors, we have computed some numerical examples. Synthetic photon spectra were computed from ideal power-law electron distributions with index δ , using the relativistic cross-sections, and other effects (high-energy cutoffs, ionization, and albedo: See Table 5.1). These synthetic photon spectra were fitted in the 10-35 keV band (1-keV bins) with photon power-laws. Photon spectral indices, γ , and fluxes at 50 keV, F_{50} , were determined from the fits. Using the Brown (1971) model, approximations to the original electron spectral indices (Eq. (5.10)) and normalization factors (Eq. (5.9)) can then be determined, from which non-thermal powers can be computed using Eqs. (5.15) or (5.16) (a 10 keV cutoff or turnover energy was assumed here: This arbitrary value

Type of correction	Quantity	$\delta=3$	$\delta=5$	$\delta=7$
Haug, Bethe-Bloch	$\Delta\gamma$	+0.1	+0.1	+0.1
	f_{50}	0.89	0.91	0.94
	f_{CO}	1.07	1.16	1.23
	f_{TO}	1.02	1.14	1.22
Haug, Bethe-Bloch, Albedo	$\Delta\gamma$	-0.2	0.0	+0.1
	f_{50}	1.54	1.36	1.25
	f_{CO}	0.96	1.285	1.40
	f_{TO}	1.09	1.29	1.40
Haug, Bethe-Bloch, High-E cutoff 50 keV	$\Delta\gamma$	+2.1	+1.2	+0.7
	f_{50}	0.02	0.2	0.47
	f_{CO}	2.64	2.20	1.71
	f_{TO}	1.45	1.95	1.65
Haug, Bethe-Bloch, High-E cutoff 300 keV	$\Delta\gamma$	+0.35	+0.1	+0.1
	f_{50}	0.50	0.90	0.94
	f_{CO}	1.23	1.17	1.23
	f_{TO}	1.02	1.15	1.22
Haug, Bethe-Bloch, $E_* = 5$ keV	$\Delta\gamma$	0.0	0.0	0.0
	f_{50}	2.54	2.67	2.84
	f_{CO}	2.81	2.74	2.63
	f_{TO}	2.74	2.74	2.64
Haug, Bethe-Bloch, $E_* = 25$ keV	$\Delta\gamma$	-0.2	-0.4	-0.3
	f_{50}	2.56	2.30	1.86
	f_{CO}	1.51	1.02	1.01
	f_{TO}	1.74	1.09	1.03
Haug, Bethe-Bloch, $E_* = 100$ keV	$\Delta\gamma$	-0.2	0.0	+0.1
	f_{50}	1.74	1.02	0.96
	f_{CO}	0.95	1.10	1.23
	f_{TO}	1.12	1.10	1.22
Haug, Bethe-Bloch, $E_* = 25$ keV, Albedo	$\Delta\gamma$	-0.4	-0.5	-0.4
	f_{50}	4.42	3.45	2.46
	f_{CO}	1.24	1.12	1.15
	f_{TO}	1.84	1.22	1.18

Table 5.1: Differences in photon spectral indices and normalization factor (flux at 50 keV), as well as computed non-thermal power (cutoff and turnover cases), between reality and assuming the Brown (1971) model. See text for details. E_* , in the context of the non-uniform target ionization model, is the minimum initial energy an electron requires to reach the neutral parts of the chromosphere (same as in Brown 1973; Kontar et al. 2003).

does not greatly change the generality of the problem). We call these quantities δ_{approx} , $A_{e,approx}$, P_{cutoff}^{approx} , and $P_{turnover}^{approx}$. $\Delta\gamma$ (Table 5.1) is the difference between the spectral index γ of the synthetic spectrum and $\delta - 1$, the photon spectral index that would have been obtained with the Brown (1971) model (Eq. (5.10)). Similarly, f_{50} is the ratio of the photon fluxes at 50 keV of the synthetic spectra with those derived theoretically using the Brown (1971) model (Eq. (5.9)). If P_{cutoff}^{real} and $P_{turnover}^{real}$ are the real non-thermal powers (derived from Eqs (5.15) and (5.16)), the factors f_{CO} and f_{TO} :

$$f_{CO} = \frac{P_{cutoff}^{real}}{P_{cutoff}^{approx}} \quad (5.17)$$

$$f_{TO} = \frac{P_{turnover}^{real}}{P_{turnover}^{approx}} \quad (5.18)$$

are the corrections that must be applied to the rough $P_{cutoff,turnover}^{approx}$ estimates. Table 5.1 indicates that the $\Delta\gamma = \gamma - (\delta - 1) = \delta_{approx} - \delta$ is usually slightly positive, i.e. applying the Brown (1971) model to observed photon power-law spectra to determine the original electron power-law spectral index generally slightly underestimates that electron spectral index. In the 10-35 keV range, for usually observed spectral hardnesses ($\delta > 4$), both corrections to the non-thermal power for relativistic effects and albedo are of the same importance, about 15-20%. The correction due to non-uniform target ionization is usually more important, particularly for low δ and low E_* (E_* is the initial energy that electrons need in order to penetrate into the unionized chromosphere). Some of the effects, when combined, might cancel each other out, and all depend on the spectral index δ : General error estimates from each effect (or the sum of them) can only be done for a certain energy band of observation and if an approximate spectral index is known. The $f_{TO,CO}$ corrections on non-thermal power exceed 50% only in extreme cases. The biggest uncertainty comes by far from the low-energy cutoff or turnover energy: the non-thermal power going as $E_{co,to}^{-\delta+2}$. The addition of albedo and/or non-uniform target ionization effects combined with the fact that spectral fitting is somewhat model-dependent may displace this $E_{co,to}$.

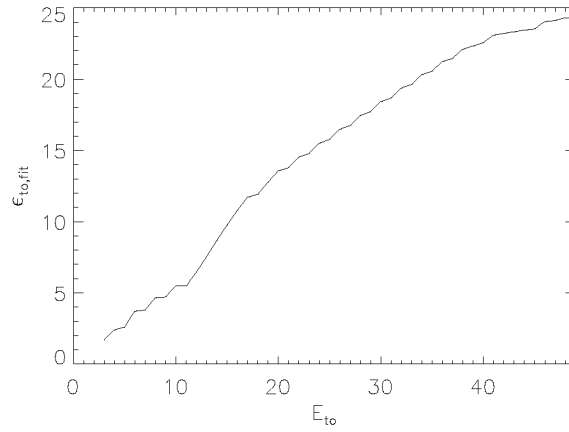


Figure 5.11: The photon turnover energy, ϵ_{to} (in keV), as obtained by fitting synthetic spectra with a weak $EM = 0.03 \times 10^{49} \text{ cm}^{-3}$, $T = 1 \text{ keV}$ thermal component, and a $\delta=5$, $A_{50} = 10^{33} \text{ electrons s}^{-1} \text{ keV}^{-1}$ non-thermal power-law distribution with different turnover energy E_{to} .

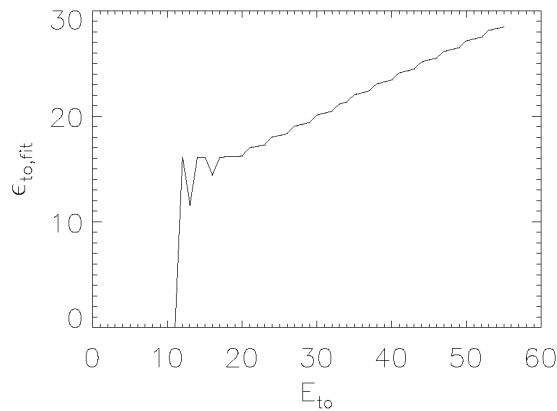


Figure 5.12: As in Fig. 5.11, $T = 1 \text{ keV}$ but with a very strong emission ($EM = 10^{49} \text{ cm}^{-3}$) for the thermal component. For $E_{to} \leq 18 \text{ keV}$, the ϵ_{to} fitting parameter may take any value (below 15 keV), and still yield a very good fit.

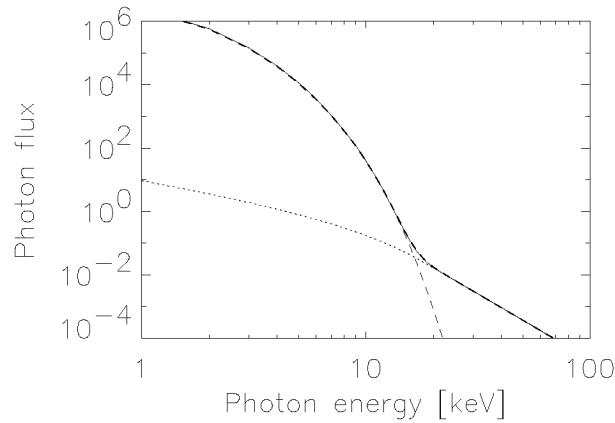


Figure 5.13: Synthetic spectrum obtained with $E_{to} = 20$ keV, other parameters as in Fig. 5.12. The Haug and Bethe-Bloch cross-sections have been used.

5.3.3 Finding the low-energy cutoff or turnover

As shown in Figs. 5.11, 5.12 and 5.13, the presence of a thermal component in the photon spectrum complicates the determination of E_{to} , the electron turnover energy. An unambiguous relationship between ϵ_{to} and E_{to} cannot always be established anymore. Making several fittings with different T , EM , δ , A_{50} , and E_{to} yielded the following rule of thumb: ϵ_{to} , and the E_{to} derived from it, seem reliable only when $\epsilon_{to} > \epsilon_{th \cap nth}$, where $\epsilon_{th \cap nth}$ is the energy where the thermal and non-thermal components of the spectrum intersect.

In a case such as depicted by Figs. 5.12 and 5.13, if the fitted ϵ_{to} is below 15 keV, then only an upper value of ~ 18 keV may be assigned for E_{to} , leading to a lower boundary for the non-thermal power.

5.4 RHESSI flare observations, data analysis

5.4.1 Flare selection criteria

In the remaining part of this chapter, the effects of the corrections and improvements on the computation of electron collisions and bremsstrahlung emission are studied on real data. The direction is now reversed: from the photon spectrum the electron energy distribution is derived and the

total non-thermal energy is estimated. The results of the previous section serve to estimate errors.

Flares have been selected from the first 18 months of RHESSI observations, using the following selection criteria:

- For simplicity's sake from a data analysis point of view, flares (or portions of flares) with the same attenuator states throughout (including background time), no decimation and no pile-up were taken.
- Flares had to have two footpoints, in order to determine a loop volume. HEDC¹ images (7" resolution, in different energy bands) were used to determine this.
- Significant HXR flux above 25 keV was required.
- Only flares above C5.0 GOES X-ray level were selected.

From the many cases 9 flares have been selected. They were relatively simple, but some have more than one HXR >25 keV episode, in which case the peaks were labelled chronologically A, B, C,... All selected flares turned out to have an attenuator state of 1 (thin shutter in). Table 5.2 lists them.

5.4.2 Extracting the thermal and non-thermal flare energies

Spectral fitting

Using the SPEX software package of the RHESSI standard analysis tools, spectral models composed of a thermal bremsstrahlung (and lines) component and a broken power-law are fitted to RHESSI spectra. The low-energy power-law has a fixed spectral index of 1.5, an average photon spectral index at photon energies below the cutoff or turnover energy of an electron power-law distribution (Fig. 5.10). The fitting was done for time intervals varying between 2 to 5 RHESSI spin periods (~ 4 s), in the 6-35 keV band. This band was chosen because lower energies could depend too much on the model used and the accuracy of the instrument's spectral response matrix. We are ignoring the cooler plasma. At higher

¹<http://www.hedc.ethz.ch>

Flare	Time intervals studied (approx.)	pos. [""]
2002/04/09 12:59	12:57:15-13:02:20	-569,405
2002/06/01 03:53 A	03:53:40-03:54:35	-423,-303
2002/06/01 03:53 ABC	03:53:40-03:58:50	
2002/07/11 14:18 A	14:17:15-14:18:10	-791,281
2002/07/11 14:18 AB	14:17:15-14:19:50	
2002/08/22 01:52 A	01:49:25-01:50:10	816,-272
2002/08/22 01:52 B	01:50:10-01:55:20	
2002/09/08 01:39	01:37:10-01:40:20	-911,-205
2002/10/05 22:50	22:50:00-22:52:45	-558,72
2002/11/10 03:11	03:07:00-03:15:00	592,-240
2002/11/14 11:09 A	11:09:15-11:10:35	-887,-262
2002/11/14 11:09 A'	11:09:25-11:09:57	
2003/06/10 02:52 ABC	02:51:15-02:53:50	561,185
2003/06/10 02:52 B	02:51:45-02:52:20	
2003/06/10 02:52 C	02:52:20-02:53:25	

Table 5.2: Flares, the time intervals that were used, and their angular offsets from Sun center.

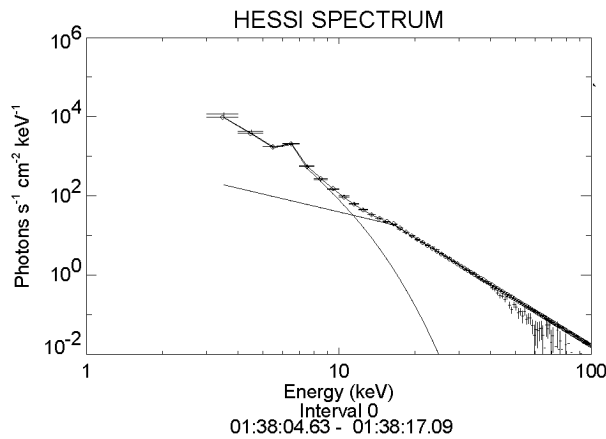


Figure 5.14: RHESSI photon spectrum, taken near the beginning of HXR emission of the 2002/09/08 M1.6 flare. See text for details.

energies, a spectral break may be present. A high-energy spectral break is most likely due to a break in the original injected electron distribution (Miller 1998). For simplicity, the details of the spectrum above this spectral break were omitted as their influence on the non-thermal power is negligible.

The five parameters retrieved are the temperature T and emission measure EM of the thermal component, the spectral index γ , normalization factor F_{50} , and the turnover photon energy ϵ_{to} of the power-law component. Only time intervals with significant HXR flux above 25 keV were studied. This requirement allows better accuracy in determination of non-thermal energies. It also has the effect of dividing the flare into episodes of large energy input for time intervals that are short, and hence with smaller thermal energy losses.

During fitting, high values for ϵ_{to} were started with, tending to yield an upper boundary for this value in cases where it was not well-defined, as happens when the photon turnover occurs near or within the thermal part of the spectrum (leading to a lower limit for the computed non-thermal energy).

Computing non-thermal energies

Non-thermal energies are computed using Eq. (5.15). As the energy turnover is difficult to fit to the observation, a two-step approach is applied. First, the non-thermal energy is computed with E_{CO} being replaced by ϵ_{to} . In the second step, a correction is applied. The rationale behind this approach is as follows:

- Initially, consider an injection electron power-law with known spectral index δ and known normalization factor A_e .
- One can then compute a synthetic thick-target photon spectrum, using the best cross-sections (Haug, Bethe-Bloch), and adding all other known effects, such as albedo. Non-uniform target ionization effects have been neglected in the following, as this correction seems unnecessary in light of the fact that no energy break in the relevant energy band (< 35 keV) for fitting were observed. This could be due to the fact that expected features from non-uniform target ionization the observed photon spectrum might go unnoticed (masking by thermal emission at the low energies, by count statistics at the

high energies): in this case, the non-thermal energies could be over-estimated by as bad as a factor ~ 3 (Table 5.1) or more for hard spectra and small E_* (below 5 keV). Assuming $E_* > 25$ keV, and electron spectral index $\delta > 3.5$, the error is at most $\pm 20\%$, and progressively less as E_* and/or δ increase.

- The synthetic non-thermal photon spectrum is very close to a power-law. One can derive, by fitting, an observed photon spectral index γ_{obs} and flux at 50 keV F_{50} .
- Using the Brown (1971) model (i.e. using Eqs. 5.9 and 5.10), one can determine a first approximation for the electron spectral index δ' and normalization factor A'_e .
- The difference $\Delta\delta = \delta' - \delta$ and ratio $r_e = \frac{A'_e}{A_e}$ both depend *only* on δ .
- To get the second approximation (true) (δ, A_e) values, one simply has to apply the corrections as follows:

$$\delta = \delta' - \Delta\delta(\delta') \quad (5.19)$$

$$A_e = \frac{A'_e(\delta')}{r_e} \quad (5.20)$$

- The second approximation electron cutoff/turnover is derived by interpolating the data points in Fig. 5.7, using δ as input.

The method converges fast and further approximations based on the values derived in Eqs. (5.19 and (5.20) have been found to be unnecessary. Knowing δ , A_e , and $E_{co,to}$, a non-thermal power and energy can be computed, or a corrective factor to what would be found if δ' , A'_e , and ϵ_{to} were used instead.

A few of the data points in the 2002/06/01 03:53 flare were also computed using the time-consuming `f_vth_thick.pro` fitting model in the SSW/SPEX program (which assumes a low-energy *cutoff* in the electron distribution) as a consistency check of the above method. It yielded a total non-thermal power very close to what was derived with the present method, given the fact that the determination of the low-energy cutoff E_{co} (the biggest source of error for the non-thermal energy) is not very reliable in both methods.

Flare	Class	Flare volume [$\times 10^{27} \text{ cm}^3$]	
		Min	Max
2002/04/09 12:59	M1.2	1.0	4.7
2002/06/01 03:53	M1.6	0.48	3.6
2002/07/11 14:18	M1.0	1.3	4.2
2002/08/22 01:52	M7.8	1.9	9.6
2002/09/08 01:39	M1.6	0.55	9.7
2002/10/05 22:50	C6.8	0.12	4.2
2002/11/10 03:11	M2.6	0.66	9.3
2002/11/14 11:09	C5.9	0.38	1.7
2003/06/10 02:52	M2.2	2.5	3.8

Table 5.3: Flare volumes, as determined (Min) by RHESSI 6-8 keV imagery, or (Max) from non-thermal energies (see text).

Computing thermal energies

Thermal energies are computed using:

$$E_{th} = 3k_B T \sqrt{EM \cdot V \cdot f} \quad (5.21)$$

Equal electron and ion temperatures and a unity filling factor f were assumed throughout. Two methods were used to determine the flare apparent volume V , both using RHESSI images done with the CLEAN algorithm, and with different sets of collimators (1-7, 2-7 and 3-7). The first one consisted in making an image in the 6-8 keV band (all flares used in this study had a visible Fe-Ni line complex above the free-free continuum), estimating the flare area A , and using $V = A^{3/2}$ as the flare volume. The second one consisted in looking at images made at non-thermal energies (usually 25-50 keV), estimating the size of footpoints by fitting 2-D elliptical gaussians, then deconvolving for the CLEAN beam. A volume is computed from the sizes and the distance between the footpoints, assuming a perfect arc-shaped loop. The first method yielded a lower value for V and the thermal energy content, while the second one provided an upper value for both. The range of values for V easily reached an order of magnitude. Considering RHESSI's dynamic range, a loop 10 times larger than a smaller one may be invisible: Assuming both loops have the same plasma content, the surface brightness of the larger one is about ~ 50 times lower than that of the smaller one (cf.

5.8). This justifies considering the second method. The *thermal energy increase*, ΔE_{th} , between the start and the end of the HXR flux is the quantity of interest. Tables 5.3 and 5.4 list the flare volumes and the thermal energies derived from them.

Figure 5.15 is an example of the acquired data and some derived quantities for the 2002/11/10 flare. Other flares studied yielded qualitatively similar behaviours, and are not displayed here.

5.5 Results and discussion

As displayed in Fig. 5.15, the peak in the 50 keV flux almost always coincides with a dip in the spectral index of the photon power-law. This common behaviour is thought to be a consequence of the acceleration process (Grigis & Benz, 2004). As observed in all our flares, the emission measure EM (both RHESSI- and GOES-derived) increases during the flare. The RHESSI-derived temperatures are usually above the GOES-derived ones, while the RHESSI-derived emission measures are below the GOES-derived ones. However, the $T\sqrt{EM}$ product is similar most of the time (as can be deduced from the thermal energies of Table 5.4). The RHESSI-derived temperature initially decreases rapidly, then stabilizes during the rest of the time when significant HXR flux > 25 keV is present. This initial decrease in RHESSI-derived temperature is not always observed, and is never present in the GOES-derived temperatures. The RHESSI spectral fittings were often less reliable at those early times, leading the authors to believe that the RHESSI-derived T and EM values are not reliable at those early times. At the later times, thermal energies derived from both RHESSI and GOES T and EM yield similar values. It might be argued that the isothermal spectrum might not always be the best model for fitting the thermal component of X-ray spectra, and that fitting a multi-thermal model, or a full differential emission measure distribution would be more proper, although technically more difficult.

The dashed line in the fifth plot of Fig. 5.15 corresponds to times where the photon turnover energy ϵ_{to} is clearly above the thermal part, hence yielding a reliable value for the corresponding electron turnover energy E_{to} . Later, the thermal part becomes so important that only an upper value for E_{to} may be determined. The turnover energy E_{to} does not seem to change substantially during the main HXR phase, and increases

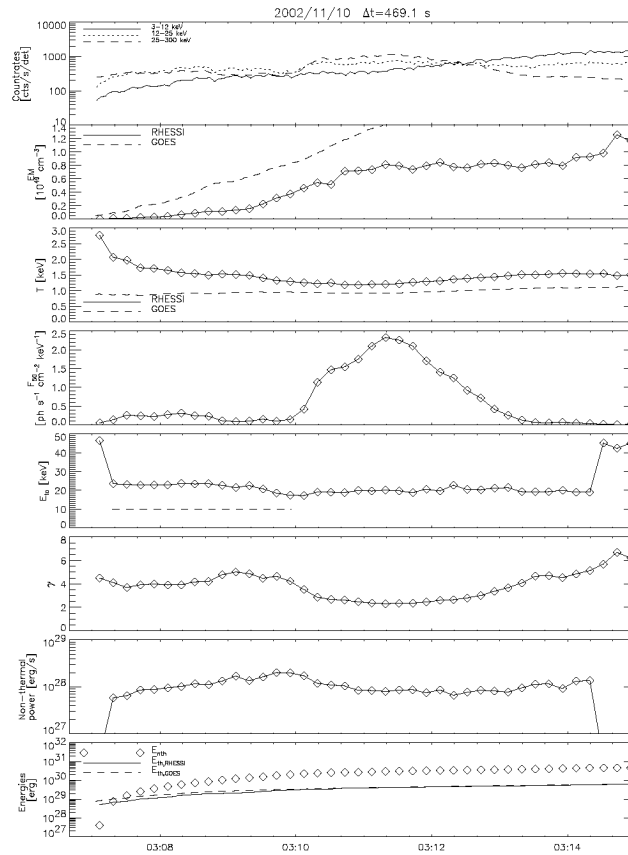


Figure 5.15: Data for the 2002/11/10 flare, during the main HXR peak. *From top to bottom:* (1) Light curves in RHESSI counts at low, intermediate, and high photon energies; (2) emission measure of thermal plasma; (3) temperature of thermal plasma; (4) calibrated photon flux at 50 keV; (5) turnover electron energy (upper limit); (6) photon spectral index; (7) non-thermal power; (8) cumulative non-thermal energy and minimal thermal energy as derived from RHESSI or GOES temperature and emission measures.

Flare	Class	dt[s]	$E_{nth,TO}$ $\times 10^{30}$ ergs	$\Delta E_{th,RHESSI,min/max}$ $\times 10^{30}$ ergs	$\Delta E_{th,GOES,min/max}$ $\times 10^{30}$ ergs
2002/04/09 12:59	M1.2	309.4	2.0	0.49/1.06	0.48/1.04
2002/06/01 03:53 A	M1.6	98.2	0.40	0.19/0.52	0.25/0.68
2002/06/01 03:53 ABC	M1.6	307.0	0.47	0.58/1.59	0.44/1.21
2002/07/11 14:18 A	M1.0	48.1	0.05	0.41/0.74	0.37/0.66
2002/07/11 14:18 AB	M1.0	120.3	0.48	0.48/0.86	0.44/0.79
2002/08/22 01:52 A	M7.8	37.2	0.09	0.04/0.09	0.048/0.11
2002/08/22 01:52 B	M7.8	298.6	21.6	1.74/3.9	1.53/3.4
2002/09/08 01:39	M1.6	162.0	6.9	0.54/2.3	0.46/1.9
2002/10/05 22:50	C6.8	158.7	0.12	0.16/0.95	0.21/1.24
2002/11/10 03:11	M2.6	468.1	4.5	0.58/2.2	0.55/2.1
2002/11/14 11:09 A	C5.9	72.4	0.20	0.18/0.38	0.21/0.44
2002/11/14 11:09 A'	C5.9	32.2	2.1	1.0/2.1	1.1/2.3
2003/06/10 02:52 ABC	M2.2	125.9	6.0	0.62/0.76	0.48/0.59
2003/06/10 02:52 B	M2.2	33.6	0.39	0.19/0.23	0.15/0.18

Table 5.4: Time intervals of significant HXR flux >25 keV, total corrected non-thermal energy for either the *cutoff* or the *turnover* models, ratio of non-thermal energy over the thermal energy increase during that time interval, with the thermal energy increase computed using either RHESSI or GOES T , EM data. The numbers in parenthesis are the range of values, due to the uncertainty in the thermal volume.

Flare volume	T,EM source	Ratio of non-thermal to thermal energies				
		All HXR peaks	$t < 75s$	$75s < t < 200s$	$t > 200s$	
min.	RHESSI	4.2 ± 4.5	1.5 ± 0.9	5.3 ± 5.6	5.7 ± 5.0	6.3 ± 5.0
	GOES	4.7 ± 5.4	1.4 ± 1.0	6.1 ± 7.0	6.5 ± 6.0	6.9 ± 5.6
max.	RHESSI	1.6 ± 1.6	0.7 ± 0.4	1.7 ± 1.8	2.1 ± 1.9	2.4 ± 2.2
	GOES	1.7 ± 2.0	0.7 ± 0.4	2.1 ± 2.3	2.3 ± 2.3	2.7 ± 2.5

Table 5.5: Ratio of non-thermal to thermal energies, for different duration t of HXR emission.

to a higher value later in the flare (see also Holman et al. 2003). The derived time of peak non-thermal power does not exactly coincide with the time of peak photon emission at 50 keV for this flare. This may not be real, as the electron turnover energy E_{to} is only an upper limit at those times.

The cutoff model yield non-thermal energies only 10 to 40 % lower than the turnover model. Fig. 5.7 provides the interpretation: for a given photon turnover energy, E_{to} is larger than E_{co} (by typically ~ 2 keV), leading to a smaller difference in non-thermal power.

In the following, only the *turnover* model is considered. The total non-thermal energy and thermal energy increase for the studied flares are summarized in Table 5.4.

Table 5.5 lists the non-thermal to thermal energy ratios, for different durations of the HXR peak. The non-thermal energies are lower limits, the non-thermal to thermal ratios are hence also lower limits. Ratios obtained using the minimal flare volume are arguably closest to the truth, most notably because of filling factor considerations. It can be noted that short HXR peaks lead to ratios of 1 or 2, whereas longer-duration peaks lead to higher ratios: $\sim 5-7$. This is expected, as radiative cooling or heat conduction (the second being most likely the dominant loss mechanism: Cargill, 1994, Porter and Klimchuk, 1995) tend to lower the thermal energy content, thereby increasing the ratio. Taking time intervals ending well after the main HXR peaks, such as the SXR peak, would tend to lower the thermal energy, and to increase the non-thermal/thermal ratio.

Emslie *al.* (2004), and Holman et al. (2004), using different approaches, reach similar ratios.

All data points have also been plotted on Fig. 5.16. Linear fitting with the bisector method (Isobe et al., 1990), more relevant in cases where variables are truly independent, yields the following relation:

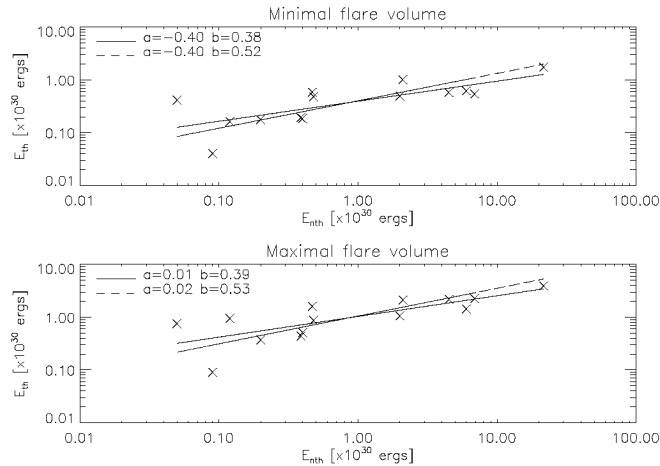


Figure 5.16: Log-log plot of non-thermal vs. thermal energies for all flares in Table 5.4. The *solid line* is a linear fitting, yielding constant a and slope b . The *dashed line* is also a linear fitting, using the bisector method.

$$\Delta E_{th} \sim E_{nth}^{0.5 \pm 0.1} \quad (5.22)$$

This empirical relation may simply state that the thermal energy increase ΔE_{th} does not increase as fast as the cumulative non-thermal energy, due to losses.

5.6 Conclusions

The investigation of the various cross-sections approximations (relativistic vs. non-relativistic) has shown that they played a relatively minor role for our energy estimation, under usual flare conditions. They are important, however, for spectral inversions and accurate derivation of the injected electron spectrum. The determination of the low-energy cutoff or turnover, the largest source of error for non-thermal energies, seems reliable in some flares at the beginning of HXR emission. With the procedure that was used, determining the non-thermal power assuming a cutoff model yielded usually only slightly less (up to $\sim 20\%$) energy than if assuming a turnover model.

The potentially largest sources of error for thermal energy estimations are the uncertainty in filling factors, and the fact that energy losses play a substantial role over long accumulation times.

The non-thermal energies and the thermal energies in a flare seem to be of the same order of magnitude, at least during the initial stages. Later on, radiative cooling or heat conduction lower the thermal energy content, thereby increasing the ratio. The ratio of non-thermal over thermal energies given in Table 5.5 are lower limits: Both lower low-energy cutoffs/turnovers or filling factors might increase it substantially. A bigger than unity ratio was expected because evaporation includes heating and expansion (Benz & Krucker, 1999), and the non-thermal to thermal energy conversion might not be 100% effective (some of the energy might rapidly be lost radiatively by cooler plasma).

5.7 ADDENDUM: Collisional evolution of an injected electron spectrum

Collisional energy losses can be expressed by the following differential equation (Brown et al. 1998) (non-relativistic case):

$$\frac{dE}{dN} = -\frac{K}{E}, \quad (5.23)$$

where $K = 2.6 \times 10^{-18} \text{ cm}^2 \text{ keV}^2$ for a fully-ionized plasma, and N the column density (cm^{-2}). Hence, electrons of energy below $E_* = \sqrt{2KN_*}$ are stopped by column density N_* .

A power-law of electrons $F_0(E_0) = A_e E_0^{-\delta}$ electrons $\text{s}^{-1} \text{ keV}^{-1}$, after undergoing collisional energy losses, has a tendency to turn over at low energies, as shown in Fig. 5.17. Analytically, $F_0(E_0) = A_e E_0^{-\delta}$ becomes:

$$F(E) = \frac{E}{\sqrt{E^2 + E_*^2}} F_0 \left(\sqrt{E^2 + E_*^2} \right) \quad (5.24)$$

Hence, for $E \gg E_*$ (i.e. at high energies), the initial power-law is unchanged, whereas at low energies ($E \ll E_*$), the electron distribution has a linear shape.

Hence, once an electron power-law distribution reaches the thick-target emitting region, it must have "linearized" at the low energies (below about $E_*/2$).

It might be argued that some low-energy flattening & linearization must already have occurred within the accelerator itself. The least energetic electrons that 'never make it out of the accelerator' might be

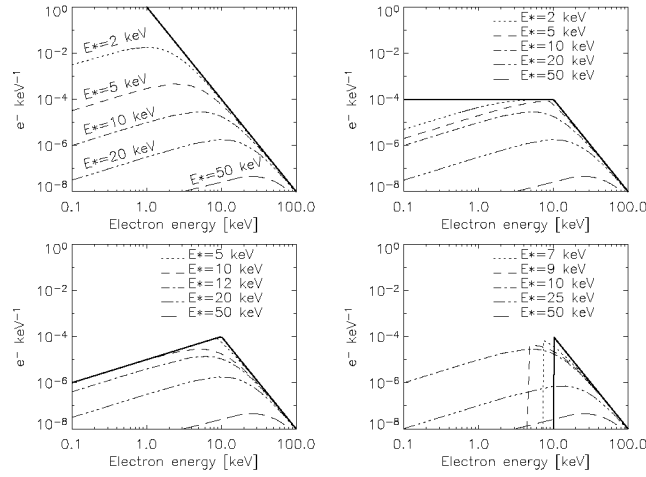


Figure 5.17: Electron power-law E_0^{-4} electrons $\text{s}^{-1} \text{keV}^{-1}$ (no qualitative change with smaller or larger spectral indices) transformed by collisional energy losses in the fully-ionized corona. The thick line is the injected electron energy spectrum. *Top left:* pure power-law. *Top right:* power-law, with a flat spectrum below 10 keV. *Bottom left:* linear slope below 10 keV, power-law above 10 keV. *Bottom right:* power-law with a low-energy cutoff at 10 keV.

recycled into pumping energy into higher-energy electrons, or heating the local corona. The electron spectrum is further flattened & linearized before reaching the denser lower corona or upper chromosphere, where most of the thick-target HXR emission occurs.

5.8 ADDENDUM: Surface brightness of two volumes with the same plasma contents

The surface brightness F of a feature is proportionnal to EM/A , where EM is the emission measure ($EM = n^2V$), and A the feature's area. Let $A = V^{2/3}$. Assuming a constant plasma content (nV) and temperature, F is hence proportional to $V^{-5/3}$. Two features possessing the same plasma content, but of differing sizes, may have a widely differing surface brightness: if the first feature is 10 times smaller in volume, it will have 46.4 times larger surface brightness! The total thermal X-ray flux from the smaller feature will also be 10 times larger.

Chapter 6

Summary and Outlook

A person who never made a mistake never tried anything new.

Albert Einstein (1879–1955)

The man who follows the crowd will usually get no further than the crowd. The man who walks alone is likely to find himself in places no one has ever been.

Alan Ashley-Pitt

6.1 Summary

In this thesis, a better understanding of particle acceleration and energy release in solar flares was sought. To achieve this goal, several solar flares have been examined in details in different wavelengths. The emphasis of most of the observations was on hard X-ray (HXR) emission from flares, with various supporting data from the radio, optical, ultraviolet (EUV) or soft X-ray (SXR) bands. The particle acceleration process *per se* has been mostly treated as a black box, and only the *injected electron spectrum*, coming out of the accelerator was studied.

Using data from the *Yohkoh* Hard X-ray Telescope and Soft X-ray Telescope, EUV images from either TRACE or SOHO, radio imagery from the Nançay radio heliograph and optical images of the corona (SOHO LASCO), temporal and spatial correlations between HXR and decimetric continuum (DCIM) emissions, ejecta, and CMEs have been investigated. Major hard X-ray flares are often associated with ejecta seen in soft X-ray or EUV, or CMEs seen in optical light. These ejecta are seemingly already on their way before any HXR or DCIM are detected, suggesting a driven reconnection process. DCIM continua occurring nearly simultaneously with the first HXR peak of a flare are located close to the HXR source and the ejection of matter, and may be a good indicator of the location of the main acceleration region.

The particle acceleration process seems not to be directly observable. Among all its possible signatures, HXR emissions seem to be the more closely tied. They could be further investigated with the newly-launched RHESSI solar X-ray satellite. Such an instrument is quite complicated, and very time-consuming to use. To speed up some of the scientific process, a data center has been successfully implemented at the Institute of Astronomy of ETH Zürich. It automatically generates a large amount of data products, tremendously helps scientists both inside and outside ETH to quickly choose data sets of interest.

A detailed analysis of one of RHESSI's first observed flare was done: Using its unequalled spatial, temporal, and spectral resolution, as well as EUV images from the TRACE satellite, energy estimates for different components were done (kinetic energy of accelerated particles and of the bulk plasma motion, thermal and non-thermal energy radiated).

The non-thermal X-ray spectral features were studied, and applied to real RHESSI data, for several flares. Injected electron spectra were derived, from which accurate non-thermal energies (i.e. kinetic energy in the accelerated particles) were derived. It was also found that the secondary thermal soft x-ray emission is not always a very good estimator of the flare energies.

The coupling between corona, where particles are accelerated, and chromosphere, which gets excited by energy deposition (cf. Appendix B), and whose material radiates thermally) has not yet been fully unravelled.

6.2 Outlook

DCIM radio emissions observed at high frequencies are generally better related to the HXR timing than all other radio emissions. They are located closer to both the HXR source and the site of matter ejection. This observation opens the possibility that future observations of DCIM at even higher frequencies (1–3 GHz) may find them even nearer and thus closer to the main acceleration region. The upcoming Frequency Agile Solar Radio telescope (FASR, Bastian et al., 1998) would achieve that.

One of the ultimate goals of RHESSI is to help making overall energy budgets. Proper flare energy estimates are important, inasmuch as coronal heating might be wholly explained by the constant nanoflaring of the Sun. The Sun being such an efficient particle accelerator, what are the reconnection and particles acceleration models that are closest to the Truth? For example, Emslie et al. (2004) have estimated that, for the July 23, 2002 X-flare, of the initial $\sim 10^{33}$ ergs of estimated free magnetic energy, 3% were converted into non-thermal electrons, 8% into non-thermal ions (which were observed to be at different location than the electrons!), 1% into thermal plasma, and 10% into CME energy. Solar energetic particles (SEPs) accounted for less than 0.1% (although, in the 2002 April 21 flare, magnetically better connected to Earth, they amounted to 15% of the CME energy). Hence, about 20% of the initial free magnetic energy was converted.

Exploitation of the RHESSI data has not yet reached its full potential: Flare and gamma-ray burst polarization are being investigated, and first imaging of the Crab Nebula in HXR (synchrotron radiation) is also expected.

As separate entities, both imaging and full-Sun spectroscopy are expected to improve, as knowledge of the instrument's response is further increased. With RHESSI's spectral resolution, spectral inversion (determining the original electron spectrum from the observed photon spectrum) is possible for the first time, and could completely replace forward-fitting techniques, which require an *a priori* model. Spectral inversion is constantly being improved, and has reached the point where one has to be careful about the choice of the bremsstrahlung differential cross-section (even including electron-electron bremsstrahlung), Compton back-scattering of HXR on the photosphere, or non-uniform target ionization.

Full imaging spectroscopy is still at its beginning: Spatially separated spectra from thermal, non-thermal, loop top and foot point sources could be the key to a more accurate determination of the low-energy cutoff and its shape (sharp cutoff, smoother turnover ?), and ultimately a better knowledge of the acceleration process.

Appendix

Appendix A

Useful cross-sections

A.1 Bremsstrahlung cross-sections

Brown (1971) introduced the *non-relativistic Bethe-Heitler differential bremsstrahlung cross-section* in his analytical treatment of the thick- and thin-target models of solar HXR emission:

$$\left(\frac{d\sigma_B}{d\epsilon}\right)(E, \epsilon) = \overline{Z^2} \frac{\kappa_{BH}}{\epsilon E} \ln \left(\frac{1 + \sqrt{1 - \epsilon/E}}{1 - \sqrt{1 - \epsilon/E}} \right) \quad [\text{cm}^2 \text{ keV}^{-1}] , \quad (\text{A.1})$$

where E is the electron kinetic energy [keV], ϵ the energy of the emitted photon [keV], $\overline{Z^2}=1.44$ for coronal abundances, and:

$$\kappa_{BH} = \frac{8}{3} \alpha r_e^2 m_e c^2 = 7.9 \times 10^{-25} \quad [\text{cm}^2 \text{ keV}] \quad (\text{A.2})$$

It is exactly the same as Koch & Motz (1959) formula 3BN(a).

The simplified Kramer cross-section:

$$\left(\frac{d\sigma_B}{d\epsilon}\right)(E, \epsilon) = \overline{Z^2} \frac{\kappa_{BH}}{\epsilon E} \quad [\text{cm}^2 \text{ keV}^{-1}] \quad (\text{A.3})$$

allows easier analytical derivations, but is a lot less accurate and should be used with caution.

The Haug (1997) cross-section is the one currently in use in the Solarsoft X-ray packages (brm_bremcross.pro).

The above cross-sections are only for electron-ion interactions. Particularly at high energies, the electron-electron bremsstrahlung should be

added (Haug, 1998; see also Koch & Motz, 1959). Fig. A.1, A.2 and A.3 compare those different cross-sections.

As a rule of thumb in the case of solar flare non-thermal HXR spectra, Eq. (A.1) should be good enough unless the photon power-law spectral index is $\gamma \lesssim 2 - 2.5$.

The *total* electron-ion bremsstrahlung cross-section is estimated to be (formula 4BN(a) of Koch & Motz, 1959):

$$\sigma_B = \frac{16}{3} \alpha \overline{Z^2} r_0^2 \quad (\text{A.4})$$

$$\approx 4.33 \times 10^{-27} \quad [\text{cm}^2] \quad (\text{A.5})$$

in the non-relativistic case. For the relativistic case (formula 4BN(b) of Koch & Motz, 1959):

$$\sigma_B(\gamma) = 4\alpha \overline{Z^2} r_0^2 \left[\ln(2\gamma) - \frac{1}{3} \right] \quad (\text{A.6})$$

$$\approx 3.25 \times 10^{-27} \left[\ln(2\gamma) - \frac{1}{3} \right] \quad [\text{cm}^2] \quad (\text{A.7})$$

γ is the Lorentz factor of the electron. And finally, in the ultra-relativistic case (formula 4BS of Koch & Motz, 1959):

$$\sigma_B = 4\alpha \overline{Z^2} r_0^2 \left[\ln \left(\frac{183}{Z^{1/3}} \right) + \frac{1}{18} \right] \quad (\text{A.8})$$

$$\approx 16.7 \times 10^{-27} \quad [\text{cm}^2] \quad (\text{A.9})$$

Only for electron energies $E \gtrsim 300$ MeV do bremsstrahlung energy losses become higher than those by non-radiative Coulomb collisions (ionization).

A.2 Energy-loss cross-sections

A.2.1 Coulomb energy-loss cross-section

Coulomb losses of high-energy electrons are mostly due to electrons in the ambient plasma. In the non-relativistic approximation, the energy-loss

cross-section is:

$$-\frac{1}{E} \frac{dE}{n_e dx} = \sigma_c(E) = \frac{2\pi e^4 \Lambda}{E^2} = \frac{K}{E^2}, \quad (\text{A.10})$$

where E is in keV, n_e in cm^{-3} , dx in cm, Λ is the Coulomb logarithm (≈ 20 under coronal conditions), yielding $K = 2.6 \times 10^{-18} \text{ cm}^2 \text{ keV}^{-2}$. Coulomb losses are less against bound electrons (neutral medium), by about a factor 2.8. For relativistic electrons, the full Bethe-Bloch formula for energy loss should be used:

$$-\left(\frac{dE}{dx}\right) = \frac{4\pi e^4}{m_e v^2} n_e (\Lambda + \ln(\gamma^2) - \beta^2) \quad (\text{A.11})$$

See Fig. 5.1 for a comparison.

A.2.2 Magnetobremstrahlung (gyro- and synchroton) energy losses

As losses by gyrosynchroton or synchroton are not dependent on the density of the medium, it is not relevant to speak of energy-loss cross-sections. From Lang (1999)[Eq. 4.421], for relativistic electrons of *total* energy E :

$$-\left(\frac{dE}{dt}\right) = -\left(c \frac{dE}{dx}\right) = \frac{2e^4}{3m^2 c^3} \gamma^2 B^2 \quad (\text{A.12})$$

$$= 3.2 \left(\frac{E}{10\text{MeV}}\right)^2 \left(\frac{B}{100\text{G}}\right)^2 \quad [\text{keV/s}] \quad (\text{A.13})$$

To compare, in a $n_e = 10^{10} \text{ cm}^{-3}$ coronal plasma, a 10 MeV electron loses about 4.5 keV/s by non-radiative Coulomb losses.

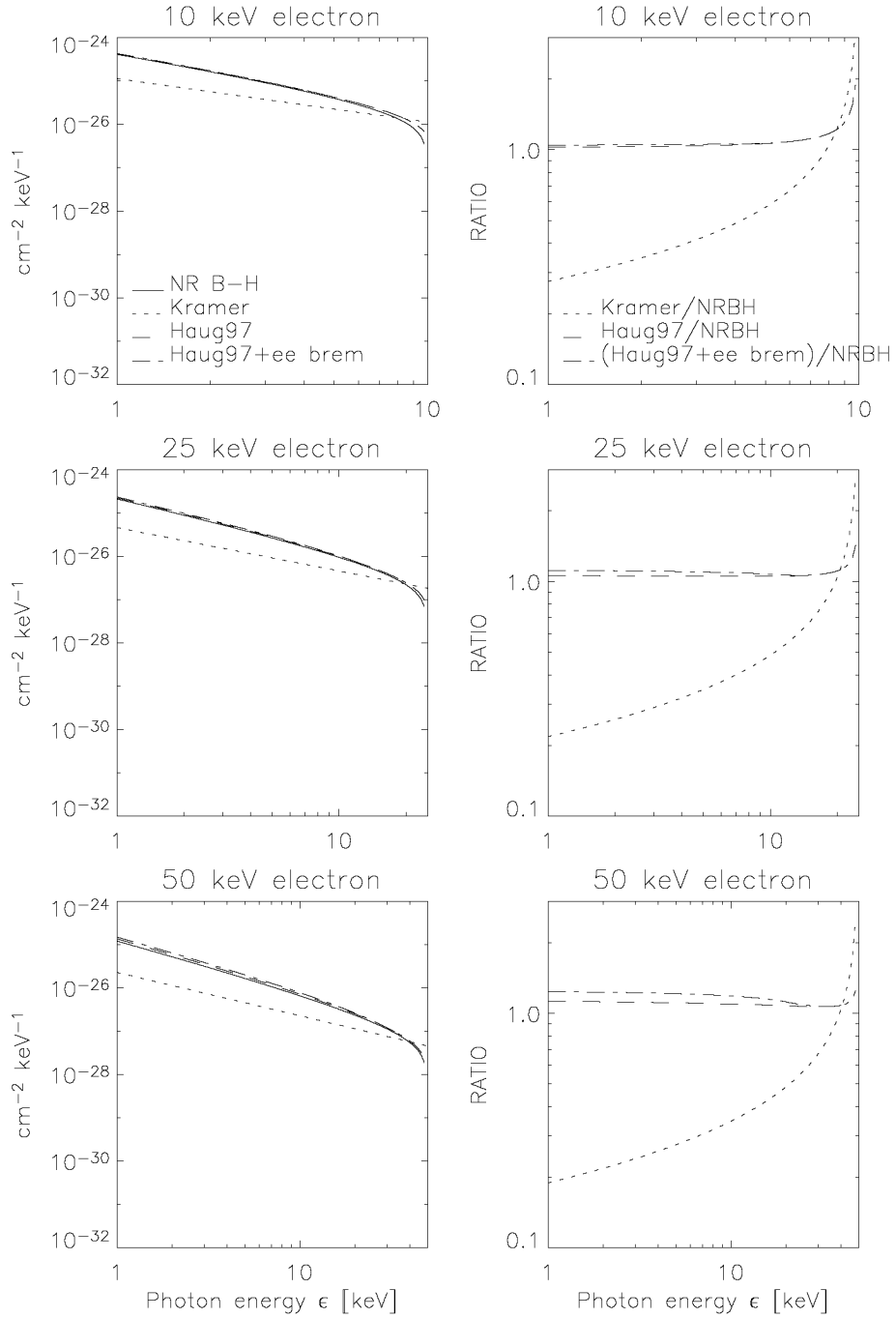


Figure A.1: Bremsstrahlung differential cross-sections, for different electron kinetic energies.

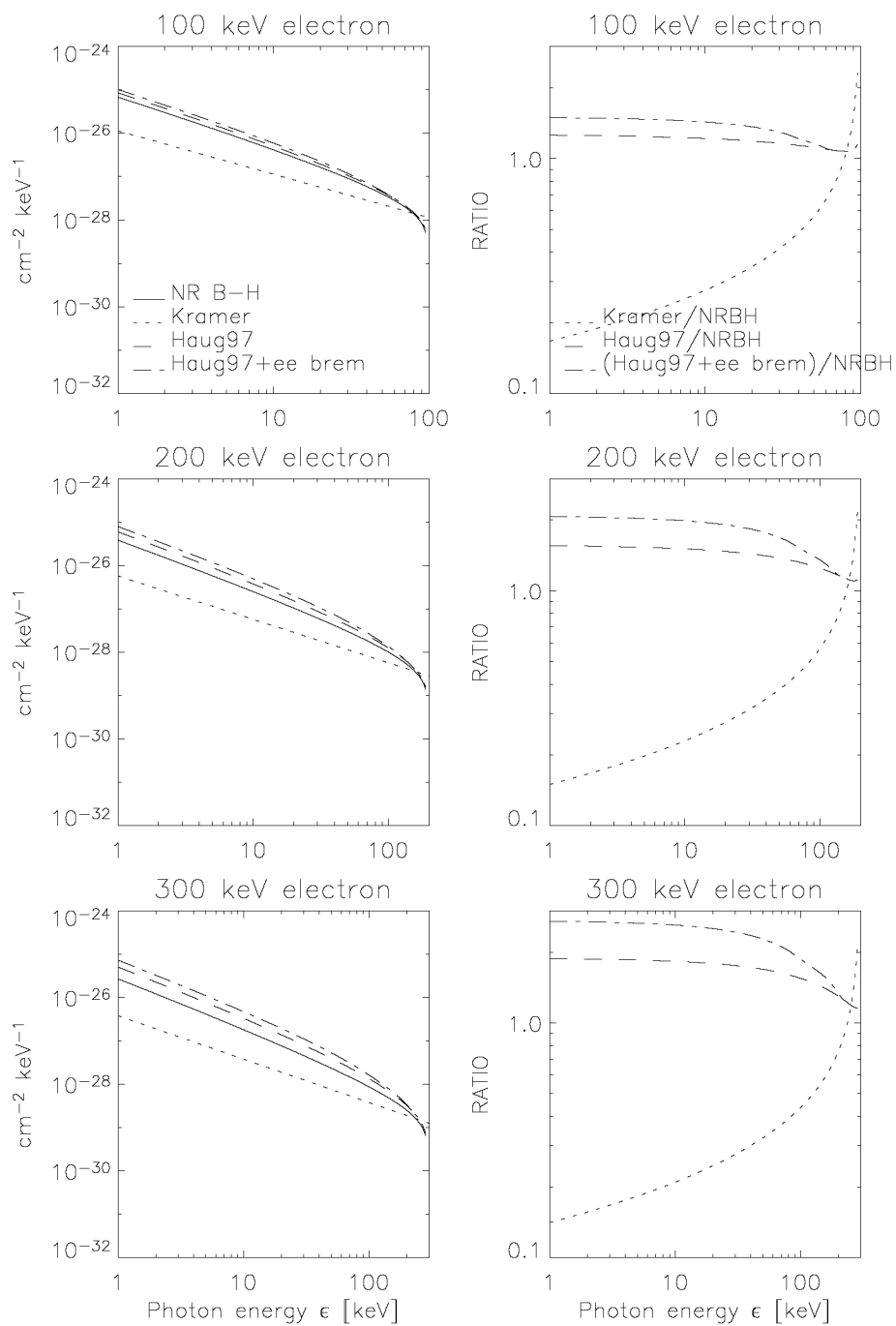


Figure A.2: Bremsstrahlung differential cross-sections, for different electron kinetic energies.

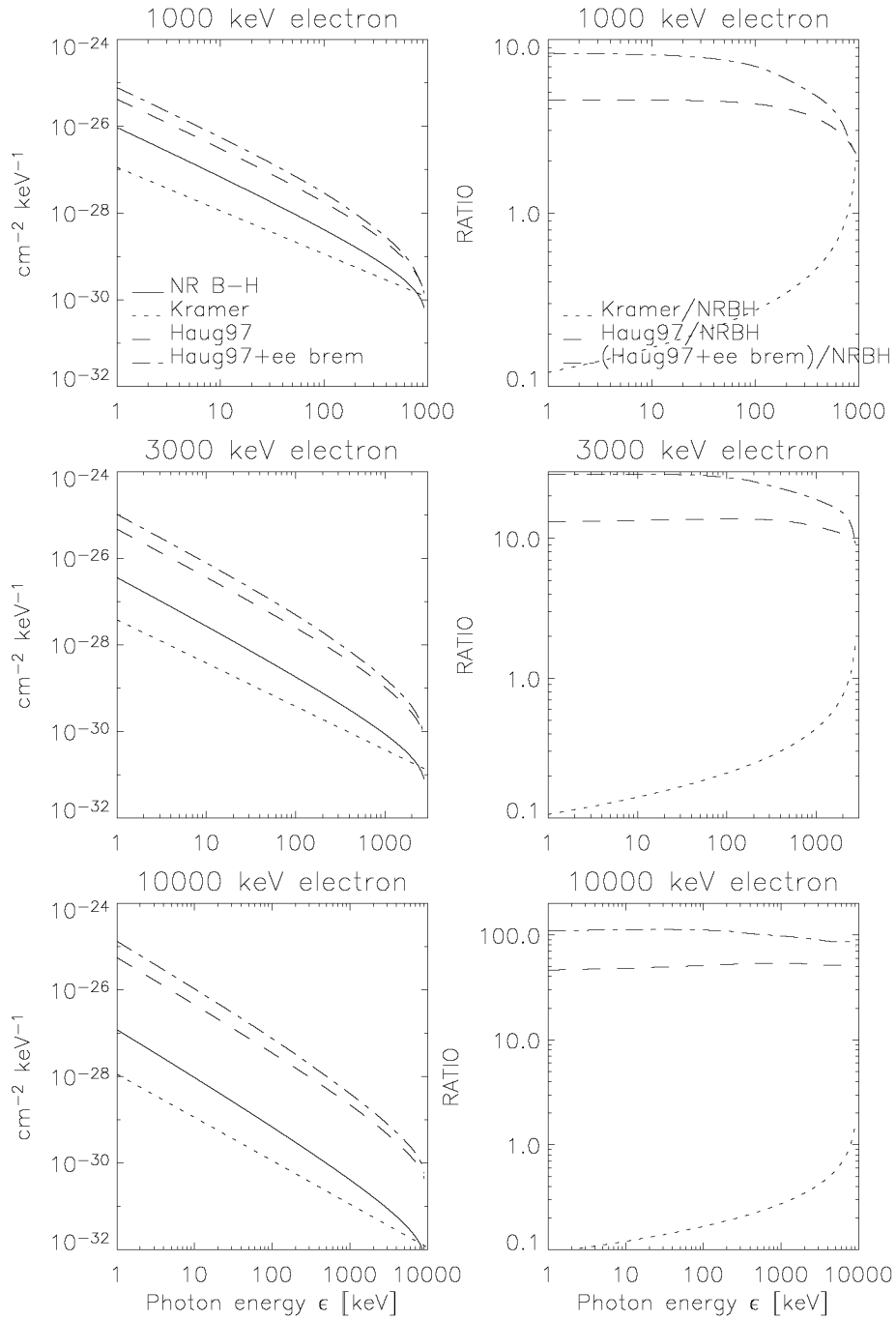


Figure A.3: Bremsstrahlung differential cross-sections, for different electron kinetic energies.

Appendix B

Energy deposition in the upper chromosphere and transition region

Fontenla et al. (1993) provided several model solar atmospheres. Model “P” was considered. This model is appropriate for plage, and may also apply for flares or start of flares. Some of its characteristics have been plotted in Fig. B.1. The data covers the lower photosphere, the chromosphere, and the transition region, stopping at ~ 1750 km of altitude above the photosphere. Figures B.2 to B.6 use these data to compute the energy deposited at different altitudes by electrons injected *downwards*, from an altitude of 1750 km. Unless otherwise specified, the Bethe-Bloch formula has been used for Coulomb losses: It is valid in both the non-relativistic and relativistic regimes.

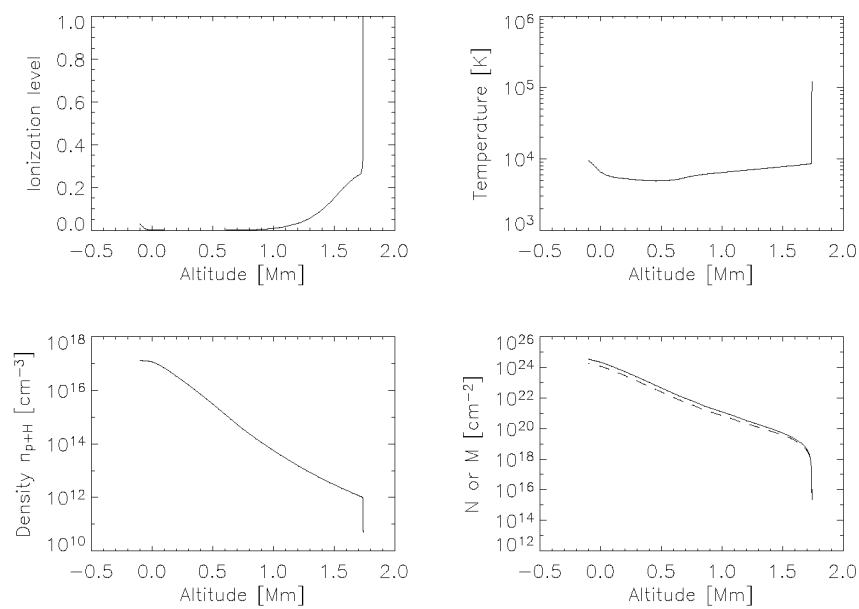


Figure B.1: Some characteristics of Fontenla et al. (1993), as a function of altitude above the photosphere: Ionization level, Temperature, proton+neutral hydrogen densities, column density (N , *solid line*), and ionization-weighted column density (M , *dashed line*).

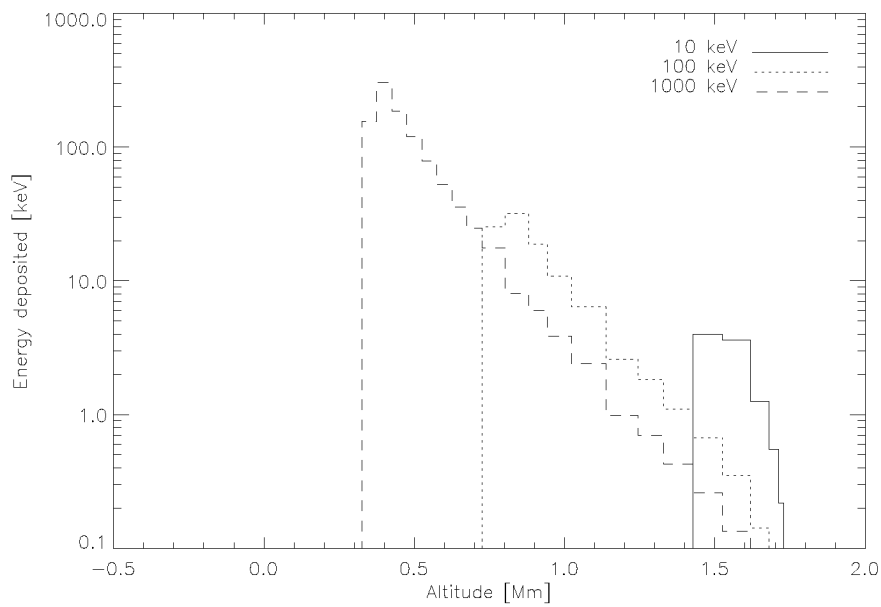


Figure B.2: Energy deposition of single electrons of initial energy 10, 100 & 1000 keV. Time of flight was ~ 5 ms for both 10 and 100 keV electrons, and ~ 2.5 ms for the 1000 keV electron.

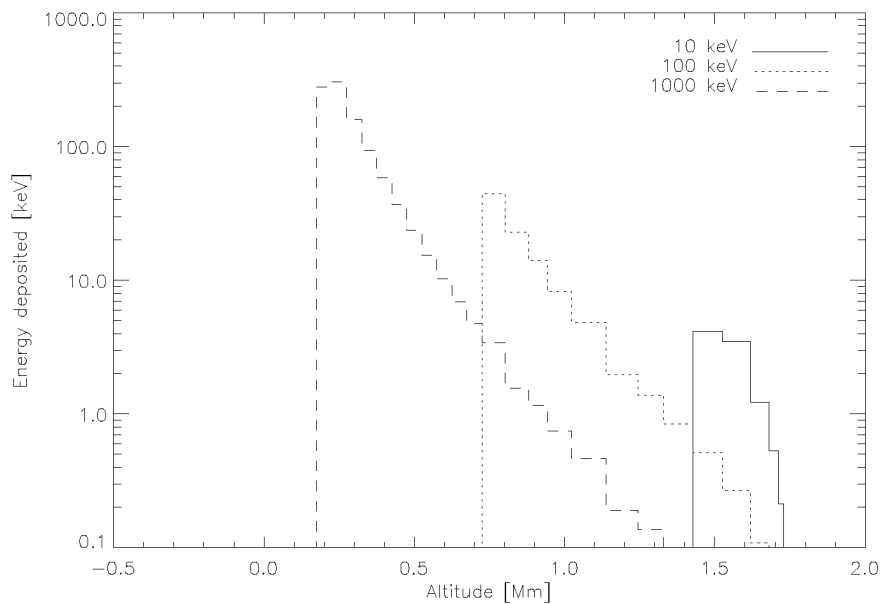


Figure B.3: As in Fig. B.2, but Coulomb losses have been computed using a non-relativistic approximation (Eq. (5.3)).

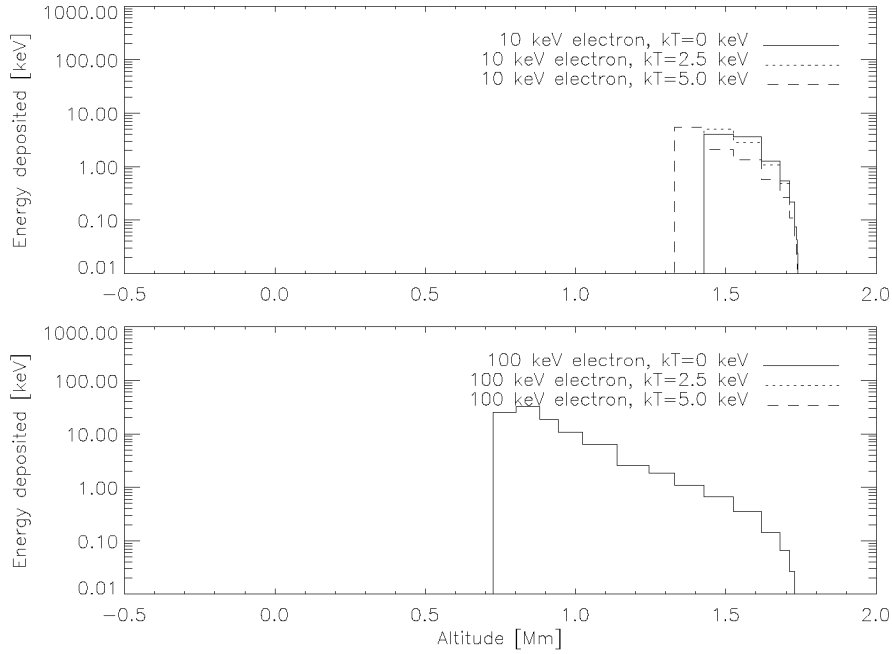


Figure B.4: As in Fig. B.2, in a “hot” target (Eq. 5.4). Basically, only electrons with energies of the same order as the plasma temperature are affected.

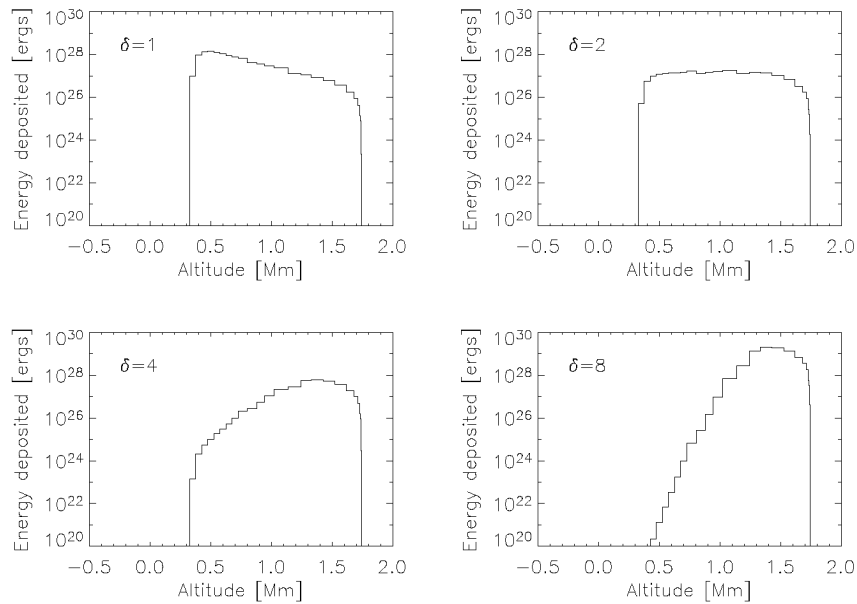


Figure B.5: Injected power-law electron spectra have been used, with spectral indices δ , flux at 50 keV of $1.3 \times 10^{33} \text{ e}^- \text{ keV}^{-1}$, and turnover at 20 keV.

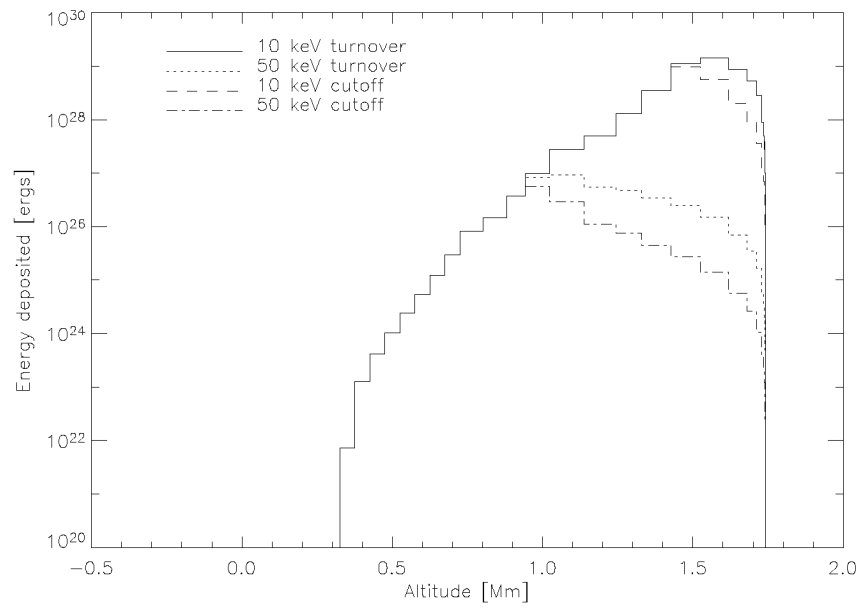


Figure B.6: Injected power-law electron spectra have been used, with spectral indices $\delta = 5$, flux at 50 keV of $1.3 \times 10^{33} \text{ e}^- \text{ keV}^{-1}$, and cutoff or turnover energies at 10 or 50 keV.

Appendix C

The Ramaty High-Energy Solar Spectroscopic Imager

Most of my work at ETH was centered around the Ramaty High-Energy Solar Spectroscopic Imager (RHESSI; Lin et al., 2002), which was launched on February 5, 2002, after two major delays. The first delay was due to a “shake” test went awry: 10 times the originally intended g-force was actually applied. This test occurred even before my coming to ETH (August 2000). RHESSI (or HESSI, as it was still known then) had to be disassembled, and its various parts re-examined by their manufacturers. The launch date was pushed from July 2000 to June 2001. But on June 2, 2001, one week before the scheduled RHESSI launch, NASA’s new experimental X-43 hypersonic scramjet aircraft suffered a catastrophic failure when it ceased controlled flight five seconds after ignition of the Pegasus missile’s engine. RHESSI was also to be mounted at the tip of such a missile (albeit in a different configuration). NASA headquarters preferred to err on the cautious side, and postponed the flight until an investigation board would clear the problem. RHESSI has finally been successfully launched on February 5th, 2002, and has provided an average of 1.8GB of data per day ever since. The X-43 is also doing fine, by the way.

Unlike at longer wavelengths, focusing optics are not feasible for hard X-rays and gamma-rays. RHESSI hence relies on Fourier-transform imaging. It uses 9 rotating sub-collimator grid pairs of different pitch, in front of 9 germanium detectors. These grids modulate the X-rays coming from the Sun. Each photon is tagged in time and energy. As the grid position and the satellite’s pointing are known at all times, image reconstruction

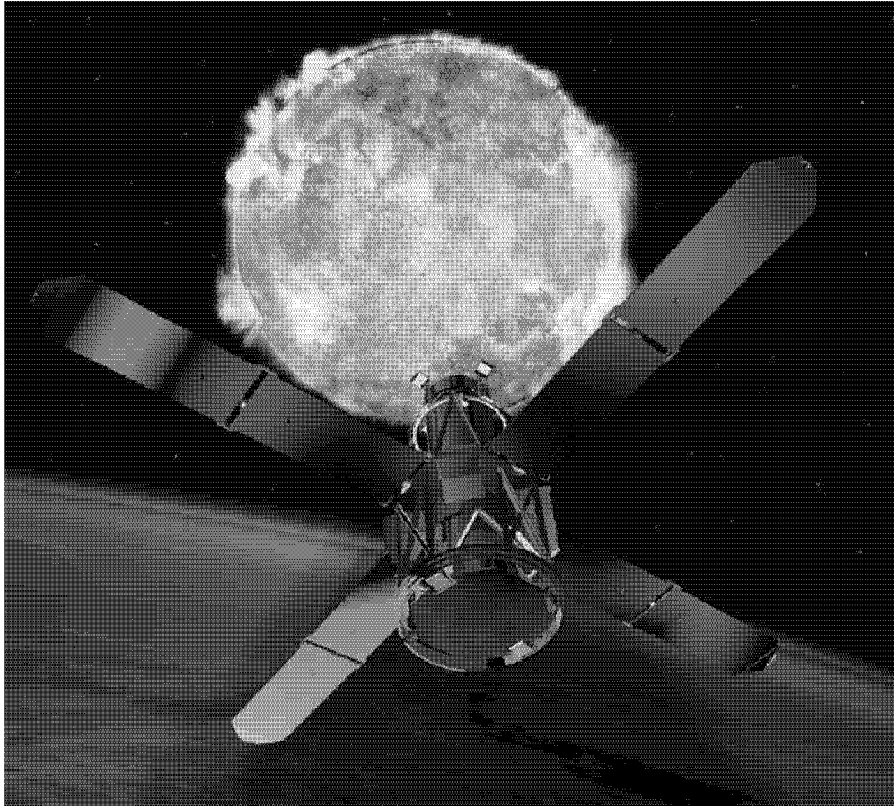


Figure C.1: The Ramaty High-Energy Solar Spectroscopic Imager observing the Sun (artist's impression).

may be done. It is computationally intensive: Typically a minute or less for a good-quality image, up to several hours for the best possible image.

Some instrumental characteristics:

1. Energy range: from 3 keV to 17 MeV
2. Energy resolution (FWHM): $\lesssim 1$ keV at 3 keV, increasing to ~ 5 keV at 5 MeV.
3. Angular resolution: 2.3 arcseconds to 100 keV, 7 arcseconds to 400 keV, 36 arcseconds to 15 MeV.
4. Temporal resolution: 2s for detailed image
5. Field of view: full Sun (~ 1 degree)

RHESSI has a trajectory 38 degrees inclined to the Equator, 590 km in altitude, and takes about 96 minutes to complete one orbit.

More details may be found in Lin et al. (2002) and accompanying papers in that volume.

Curriculum Vitae

Name	Pascal Saint-Hilaire
Date of birth	March 9, 1972
Place of birth	Hull, Canada
Nationality	Canadian, Swiss
1978 - 1980	Ecole Notre-Dame, Aylmer, Canada
1980 - 1984	Lycée Français de Belgique, Belgium
1984 - 1987	Lycée Claudel, Ottawa, Canada
1987 - 1990	Lycée Descartes, Rabat, Morocco
1990	Baccalaureat type 'C': "Maths & Physics"
1990 - 1994	Electrical Engineering at University of Ottawa, Ottawa, Canada
1994	B.Sc.A Electrical Engineering
1995 - 2000	Physics studies at University of Neuchâtel, Neuchâtel, Switzerland
2000	Dipl. Phys.
2000 - 2004	Research assistant at the Radio Astronomy and Plasma Physics Group, Institute of Astronomy, ETH Zürich
2004	Doctoral thesis: <i>Energy release in solar flares</i> Thesis supervisor: Prof. Dr. A. O. Benz

List of Publications

Publications in Refereed Journals

- Electron Trapping, Reconnection, or Shock Acceleration in Flare Radio ‘Afterglows’? Arnold O. Benz, Hubert Perret, Pascal Saint-Hilaire, Paolo Zlobec 2005, *Astronomy and Astrophysics*, submitted
- Thermal and non-thermal energies of solar flares
Pascal Saint-Hilaire and Arnold O. Benz,
2005, *Astronomy and Astrophysics*, submitted
- Survey on solar X-ray flares and associated coherent radio emissions
Arnold O. Benz, Paolo C. Grigis, Andre Csillaghy and Pascal Saint-Hilaire,
2004, *Solar Physics* , in press.
- Solar flare electron acceleration: comparing theories and observations
Arnold O. Benz and Pascal Saint-Hilaire,
2003, *Advances in Space Research* **32**, 2415 - 2423
- Hard X-ray, ejecta, and their associated decimetric radio emission in solar flares
Pascal Saint-Hilaire, and Arnold O. Benz,
2003, *Solar Physics* **216**, 204 - 224
- Energy budget and imaging spectroscopy of a compact flare
Pascal Saint-Hilaire, and Arnold O. Benz,
2002, *Solar Physics* **210**, 287 - 306
- The RHESSI Experimental Data Center
Pascal Saint-Hilaire, Christoph von Praun, Etzard Stolte, Gustavo

Alonso, Arnold O. Benz, and Thomas Gross,
2002, *Solar Physics* **210**, 143 - 164

- The solar origin of a slowly drifting decimetric-metric pulsation structure
Josef I. Khan, Nicole R. Vilmer, Pascal Saint-Hilaire, and Arnold O. Benz,
2002, *Astronomy and Astrophysics* **388**, 363 - 372
- Location of narrowband spikes in solar flares
Arnold O. Benz, Pascal Saint-Hilaire and Nicole R. Vilmer,
2002, *Astronomy and Astrophysics* **383**, 678-684

Acknowledgments

As with most endeavours, completing this thesis was not always “a walk in the park”. The way has been greatly facilitated by the great colleagues and work environment I have had.

First and foremost, I wish to express my gratitude to my supervisor, Prof. Arnold Benz: He trusted me enough to give me this PhD position. This, as well as his endless patience, constant cordial attitude and sound advice allowed me to reach meaningful goals, both private and professional. Thank you for putting up with me, Arnold.

Through Manuel Güdel, my position was in part financed by the Paul Scherrer Institute’s Laboratory for Astrophysics, headed by Alex Zehnder. Thank you for this additional support, Manuel. I am even more grateful for your eagerness in sharing your wisdom.

For their assistance, discussions (both work and non-work oriented) and/or companionship, special thanks to my colleagues, past, and present: Michael Arnold, Kaspar Arzner, Marc Audard, Marina Battaglia, Kevin Briggs, André Csillaghy, Barbara Codoni, Sonia Hirt, Reto Knaack, Christian Monstein, Peter Messmer, Gunnar Paesold, Christoph von Praun, Hubert Perret, Kester Smith, Pascal Stäuber, Peter Steiner, Etzard Stolte, Alessandra Telleschi, Thomas Wenzler, and in particular Paolo Grigis, who has admirably filled the shoes of both friend and collaborator. Their individual contribution and the degree of my gratitude need not be spelled out here.

I also wish to acknowledge the RHESSI software team for encouragements, help, and/or discussions, in particular Brian Dennis, André Csillaghy (again!), Hugh Hudson, Gordon Hurford, Säm Krucker, Jim McTiernan, Richard Schwartz, Ed Schmahl, and Kim Tolbert.

Thanks to the members of my family who steadfastly stood by me. Lastly, very special thanks to Karin Ammon: The heart also needs nur-

turing.

This thesis was made possible by the joint funding of the ETH Zürich and the Paul Scherrer Institute, Würenlingen und Villigen. Parts of it were financially supported by the Swiss National Science Foundation grant No. 20-67995.02 and ETH grant TH-W1/99-2.

Bibliography

- Alexander, R.C., Brown, J.C., 2003, *Solar Physics*, **210(2)**, 407
- Aschwanden, M.J., Alexander, D., 2001, *Solar Physics*, **204**, 93
- Aschwanden, M.J., Benz, A.O., 1986, *Astron. Astrophys.* **158**, 102
- Aschwanden, M.J., Benz, A.O., 1988, *Astrophys. J.* **332**, 447
- Aschwanden, M.J., Benz, A.O., Kane, S.R., 1990, *Astron. Astrophys.* **229**, 206
- Aschwanden, M.J., Schwartz, R.A., Dennis, B.R., 1998, *Astrophys. J.* **502**, 468
- Bai, T., Ramaty, R., 1978, *Astrophysical Journal*, **219**, 705
- Bailey, S.M., Woods, T.N., Barth, C.A., Solomon, S.C., Canfield, L.R., Korde, R., 2000, *Journal of Geophysical Research*, **105(A12)**, 27179
- Bastian, T.S., Gary, D.E., White, S.M., and Hurford, G.J., 1998, Towards a Frequency-Agile Radiotelescope. In: *Advanced Techniques in mm-Wave, Radio and Terahertz Telescopes*, Phillips T. (ed.), *Proc. SPIE*, **3357**, 609
- Benz, A.O., 1977, *Astrophysical Journal*, **211(1)**, 270
- Benz, A.O., 1986, *Solar Phys.* **104**, 99
- Benz, A.O., Csillaghy, A., Aschwanden, M.J., 1996, *Astron. Astrophys.* **309**, 291
- Benz, A.O., Krucker, S., 1999, in *Proc. 9th European Meeting on Solar Physics*, 'Magnetic Fields and Solar Processes', Florence, Italy, 12-18 September 1999, ESA SP-448, December 1999

- Benz, A.O., 2002, *Plasma Astrophysics, Kinetic Processes in Solar and Stellar Coronae*, 2nd Ed., Kluwer Academic Publishers
- Benz, A.O., Saint-Hilaire, P., Vilmer, N.R., 2002, *Astron. Astrophys.* **383**, 678
- Benz, A.O., Saint-Hilaire, P., 2003, *Advanced Space Research*, **32(12)**, 2415
- Brown, J.C., 1971, *Solar Physics*, **18**, 489
- Brown, J.C., 1973, *Solar Physics*, **28**, 151
- Brown, J.C., 1974, in *Coronal Disturbances*, G. Newkirk, Jr. (ed.), IAU Symp. **57**, 395.
- Brown, J.C., McArthur, G.K., Barrett, R.K., McIntosh, S.W., Emslie, A.G., 1998, *Solar Physics*, **179**, 379
- Bruggmann, G., Benz, A.O., Magun, A., Stehling, W., 1990, *Astron. Astrophys.* **240**, 506
- Cargill, P.J., 1994, *Astrophysical Journal*, 422, 381
- Livingston, W.C., *et al.*, 1991, in *Solar Interior and Atmosphere*, University of Arizona Press, Tucson, p. 1136
- de Jager, C., Bruner, M.E., Crannel, C.J., Dennis, B.R., Lemen, J.R., Martin, S.F., 1989, in *Energetic Phenomena on the Sun*, Kluwer Academic Publishers, Dordrecht, Holland, p. 396
- Dennis, B.R., Zarro, D.M., 1993, *Solar Physics*, **146**, 177
- Dulk, G.A., Marsh, K.A., 1982, *Astrophysical Journal*, **259**, 350
- Dulk, G.A., 1985, *Annual Review of Astronomy & Astrophysics*, **23**, 169
- Emslie, A.G., 2003, *Astrophysical Journal*, **595**, 119
- Fermi, E. 1949, *Physical Review*, **75**, 1169
- Emslie, A.G., *et al.*, 2004, *Journal of Geophysical Science*, to be published
- Fishman, G.J. *et al.*, 1989, Proceedings GRO Science Workshop **2**, 39

- Fontenla, J.M., Avrett, E.H., Loeser, R., 1989 *Astrophysical Journal* **406**, 319
- Gan W.Q., Li, Y.P., Chang, J., 2001, *Astrophysical Journal*, **552**, 858
- Guedel, M., Benz, A.O., 1988, *Astron. Astrophys. Suppl. Ser* **75**, 243
- Güdel, M., Benz, A.O., Aschwanden, M.J., 1991, *Astron. Astrophys.* **251**, 285
- Güdel, M., 2002, *Phil. Trans. R. Soc. Lond.*, **A360**, 1935
- Handy B. *et al.*, 1999, *Solar Physics*, **187(2)**, 229
- Haug, E., 1997, *Astron. Astrophys.*, **326**, 417
- Haug, E., 1998, *Solar Physics*, **178**, 341
- Hinteregger, H.E., Fukui, K., Gilson, G.R., 1981, *Geophysical Research Letter*, **8**, 147
- Holman, G.D., Sui, L., Schwartz, R.A., Emslie, A.G., 2003, *Astrophysical Journal*, 595(2), L97
- Holman, G.D., Dennis, B.R., Sui, L., 2004, AAS Meeting 204, #54.17
- Hori, K., 1999, in *Solar Physics with Radio Observations*, Proceedings of the Nobeyama Symposium, NRO Report No. 479, p. 267
- Hudson, H.S., Canfield, R.C., Kane, S.R., 1978, *Solar Physics*, **60**, 137
- Hurford, G. *et al.*, 2002, *Solar Phys.*, **210**, 61
- Innes, D.E., Inhester, B., Axford, W.I., and Wilhelm, K., 1997, *Nature* **386**, 811.
- Islaker, H., Benz, A.O., 1994, *Astron. Astrophys. Suppl. Ser* **104**, 145
- Isobe, T., Feigelson, E.D., Akritas, M.G., Babu, G.J., 1990, *Astrophys. J.* **459**, 342
- Jiricka, K., Karlicky, M., Kepka, O., Tlamicha, A., 1993, *Astrophysical Journal* **364**, 104

- Karpen, J.T., et al. 1977, *Astrophysical Journal*, **216**(2), 479
- Kahler, S., 1982, *Astrophysical Journal*, **252**, 239
- Karlicky, M., Farwik, F., Meszarosova, H., 2002, *Astron. Astrophys.* **388**, 1016
- Kerdran, A., Delouis, J.-M., 1996, in *Coronal Physics from Radio and Space Observations*, Trottet G. (ed.), Springer Verlag, Berlin, 192
- Khan, J.I., Vilmer, N.R., Saint-Hilaire, P., Benz, A.O., 2002, *Astron. Astrophys.* **388**, 363
- Kirk, J.G., Melrose, D.B., Priest, E.R., 1994, *Plasma Astrophysics*, 24th Advanced Saas-Fee course lecture notes, Springer-Verlag
- Kliem, B., Karlický, M., Benz, A.O., 2000, *Astron. Astrophys.* **360**, 715
- Koch, H.W., Motz, J.W., 1959, *Review of Modern Physics*, **31**(4), 920
- Kontar, E.P., Brown, J. C., McArthur, G.K., 2002, *Solar Physics*, **210**(2), 419
- Kosugi, T., Makishima, K., et al., 1991, *Solar Phys.* **136**, 17
- Krucker, S., Aschwanden, M.J., Bastian, T.S., Benz, A.O., 1995, *Astron. Astrophys.* **302**, 551
- Kuijpers, J., Slottje, C., 1976, *Solar. Phys.* **46**, 247
- Lang, K.R., 1999, *Astrophysical Formulae*, **I** Springer-Verlag, 3rd Enlarged and Revised Edition
- Lin R.P., Schwartz R.A., 1987, *Astrophys. J.* **312**, 462-474.
- Lin R.P., et al., 2003, *Solar Physics*, **210**, 3
- Longair, M.S., 1992, *High Energy Astrophysics*, 2nd Ed., Vol. 1, Cambridge University Press
- Lüthi, T. 2004, *Solar Flares at Millimeter and Submillimeter Wavelengths – Instrumental Techniques and Observations* (PhD thesis)

- Martirosyan, R.M., Goulyan, A.G., Sanamyan, V.A., Manaselyan, K.A., 2002, *Astrophysics*, **45(3)**, 365
- Masuda, S., 1994, PhD Thesis, University of Tokyo, Tokyo, Japan.
- McTiernan, J.M., 2002,
http://sprg.ssl.berkeley.edu/jimm/hessi/hsi_obs_summ_soc.html
- Mendiboure, C., 1998, in *Second Advances in Solar Physics Euroconference*: ASP Conf. Series **155**, 302
- Messmer, P., Benz, A.O., Monstein, C., 1999, *Solar Phys.* **187 (2)**, 335
- Miller, J.A., LaRosa, T.N., Moore, R.L., 1996, *Astrophysical Journal*, **461**, 445
- Miller, J.A., Cargill, P.J., Emslie, A.G., Holman, G.D., Dennis, B.R., LaRosa, T.N., Winglee, R.M., Benka, S.G., Tsuneta, S., 1997, *Journal of Geophysical Research*, **102/A7**, 14631
- Miller, J.A., 1998, in *CESRA Workshop on Coronal Explosive Events*, held 9-13 June, 1998. Metsaehovi Publications on Radio Science, HUT-MET-27, 1998, p. 11. ISBN 951-22-4097-1, ISSN 1455-9587
- Miller, J.A., 1998, *Space Science Reviews*, **86**, 79
- Miller, J.A., 2000, *High Energy Astrophysics - Anticipating HESSI*, Astron. Soc. of the Pacific Conference Series, **206**, 145
- Neupert, W.M., 1968, *Astrophysical Journal*, **153**, L59
- Paesold, G., Benz, A.O., Klein, K.-L., Vilmer, N., 2001, *Astron. Astrophys.* **371/1**, 333
- Paesold, G., 2002, *PhD thesis*
- Petrosian, V., 2003, private communication (Taos workshop, New Mexico, October 2003)
- Parker, E.N., 1957, *JGR*, **62**, 509
- Petschek, H.E., 1964, in *AAS-NASA Symposium on Physics of Solar Flares*, **NASA-SP50**, 425

- Pohjolainen, S. et al., 2001, *Astrophys. J.* **556**, 421.
- Porter, L.J., Klimchuk, J.A., 1995, *Astrophysical Journal*, 454, 499
- Priest, E.R., Forbes, T.G., 1986, *Journal of Geophysical Research*, **91**, 5579
- Priest, E.R., Lee, L.C., 1990, *Plasma Phys.*, **44**, 337
- Priest, E.R., Forbes, T.G., 2000, in *Magnetic reconnection: MHD theory and applications*, New York: Cambridge University Press.
- Ramaty, R., Mandzhavidze, N., Kozlovsky, B., and Murphy, R.J., 1995, *Astrophys. J.* **455**, L193
- Roberts, B., Mangeney, A., 1982, *Mon. Not. R. Astr. Soc.* **198**, 7
- Saint-Hilaire, P., Benz, A.O., 2002, *Solar Physics*, **210(2)**, 287
- Saint-Hilaire, P., von Praun, C., Stolte, E., Alonso, G., Benz, A.O., Gross, T., 2002, *Solar Physics*, **210(2)**, 143
- Saint-Hilaire, P., Benz, A.O., 2003, *Solar Physics*, **216**, 204
- Saint-Hilaire, P., Benz, A.O., 2005, *Astronomy & Astrophysics*, submitted
- Schmahl E.J., Hurford G.J., 2002, *Solar Phys.*, **210**, 273
- Schwartz, R.A., Csillaghy, A., Tolbert, A.K., Hurford, G.J., McTiernan, J., Zarro, D.M., 2002, *Solar Phys.*, **210**, 165
- Share, G.H., Murphy, R.J., 2004, *ASP Conference Series*, *in press*
- Shibata, K. et al., 1994, *Astrophys. J.* **431**, L51
- Smith, D.M., et al., 2002, *Solar Phys.*, **210**, 33
- Stolte, E., Alonso, G., 2002, Optimizing Scientific Databases for Client-Side Processing., in *Proceedings of the VIII Conference on Extending Database Technology (EDBT)*, Prague, Czech Republic, March 2002.
- Stolte, E., Alonso, G., 2002, Efficient Exploration of Large Scientific Databases, in *Proceedings of the 28th International Conference on Very Large DataBases (VLDB)*, Hong Kong, China, August 2002.

Strong K.T., Benz, A.O., Dennis B.R., Leibacher J.W., Mewe R., Poland A.I., Schrijver J., Simnett G., Smith J.B., Sylwester J., 1984, *Solar Phys.* **91**, 325

Styx, M., 2002, *The Sun, An Introduction*, Springer, 2nd Edition

Sweet, P.A., 1958, in *Electromagnetic Phenomena in Cosmical Physics*, edited by B. Lehnert (Cambridge University Press, New York), 123

Szalay, A.S., Kunszt P.Z., Thakar A., Gray J., Slutz D.R., 2000, Designing and Mining Multi-Terabyte Astronomy Archives: The Sloan Digital Sky Survey, in *ACM International Conference on Management of Data*, SIGMOD 2000.

Szalay, A.S., Gray J., Thakar A., Kunszt P.Z., Malik T., Raddick J., Stoughton C., van den Berg J., 2002, The SDSS SkyServer - Public Access to the Sloan Digital Sky Server Data, in *ACM International Conference on Management of Data*, SIGMOD 2002.

Tanberg-Hanssen, E., Emslie, A.G., 1988, in *The Physics of Solar Flares*, Cambridge Astrophysics Series

Tsuneta S., et al., 1991, *Astrophys. J.* **459**, 342

Woods, T.N., Eparvier, F.G., Fontenla, J., Harder, J., Kopp, G., McClintock, W.E., Rottman, G., Smiley, B., Snow, M., 2004, *Geophysical Research Letters*, **31**, L10802

www resource 1:

<http://www.plasmaphysics.org.uk/research/images/solflux.gif>

www resource 2:

<http://science.nasa.gov/headlines/images/sunbathing/spectrumgif.gif>
(Courtesy of Judith Lean, NRL)

www resource 3:

<http://hesperia.gsfc.nasa.gov/rhessidatacenter/>

Zhang, J., Wang, J., Liu, Y., 2000, *Astron. Astrophys.* **361**, 759.